8-19-2014

Transport-Induced Losses in Alkaline Anion Exchange Membranes and Solid Oxide Fuel Cell Anodes

Andrew M. Kiss
University of Connecticut - Storrs, andrew.kiss@engr.uconn.edu

Transport-Induced Losses in Alkaline Anion Exchange Membranes and Solid Oxide Fuel Cell Anodes

Andrew Michael Kiss, Ph.D.

University of Connecticut, 2014

Fuel cell systems are capable of providing power for a wide range of applications. In order to improve the performance and lifetime of fuel cell systems, transport induced losses are considered. For portable power applications, alkaline anion exchange membrane (AEM) fuel cells are one option. However the ion transport through the membrane is a significant performance loss. Understanding how these membranes operate and how to increase ion mobility is important for minimizing transport losses. One factor which affects AEM performance is the local hydration in the membrane and water-membrane diffusion coefficient. By studying water transport using water flux measurements, predictions can be made for effective ion-membrane diffusion coefficients and ionic conductivity as functions of the local hydration in the membrane. Comparing the ionic conductivity results to experimental measurements, equilibrium constants can be calculated for different ionic species in the membrane to the fixed side chain groups. Understanding how dissociation of mobile ions affects transport through the membrane can be useful for designing new membranes with higher ionic conductivities.

Transport losses also affect stationary power systems such as solid oxide fuel cells (SOFCs) which suffer from degradation mechanisms such as oxidation of the electronic conductor nickel in the anode. When nickel oxidizes, there is a significant decrease in the material electronic conductivity and as well as an increase in the particle volume. With the

volume expansion, the stresses between solid phases will increase and can initiate cracks, which can lead to cell failure. The cracks will increase transport lengths for different species and decrease fuel cell performance. To investigate this degradation mechanism, nickel oxidation is investigated using a new technique in a synchrotron based transmission X-ray microscope (TXM). Using the TXM, the nickel particles can be imaged *in situ* at the nanoscale while the reaction is occurring in SOFC operating conditions. The images can then be analyzed to measure reaction rates and activation energy.

Transport-Induced Losses in Alkaline Anion Exchange Membranes and

Solid Oxide Fuel Cell Anodes

Andrew Michael Kiss

B.S., University of Connecticut, 2010

A Dissertation

Submitted in Partial Fulfillment of the

Requirement for the Degree of Doctor of Philosophy

at the

University of Connecticut

2014

APPROVAL PAGE

Doctor of Philosophy Dissertation

Transport-Induced Losses in Alkaline Anion Exchange Membranes

and Solid Oxide Fuel Cell Anodes

Presented by

Andrew Michael Kiss, B.S.

Major Advisor _____
Wilson K. S. Chiu

Associate Advisor _____
Brice N. Cassenti

Associate Advisor _____
Ugur Pasaogullari

Associate Advisor _____
Michael T. Pettes

Associate Advisor _____
Michael W. Renfro

University of Connecticut
2014

Acknowledgements

There are many people I would like to thank in helping me accomplish what I have in the past few years. First and foremost, I would like to thank my major advisor, Prof. Wilson Chiu, for giving me the opportunity to work in his lab. Under his direction, I have been able to grow as a researcher and I am grateful for the opportunities he has presented me. I would also like to thank my committee members, Prof. Brice Cassenti, Prof. Ugur Pasaogullari, Prof. Michael Pettes, and Prof. Michael Renfro, for guiding me with my research as well as evaluating my thesis. During my time here at UConn, I have had the privilege of taking classes with some excellent faculty members and would like to thank the mechanical engineering department.

This research would not have been possible if it wasn't for financial support from several funding agencies. The water flux experiment and alkaline anion exchange membrane testing was supported by the Army Research Office. The *in situ* oxidation experiments were funded through the National Science Foundation as well as partial support from a U.S. Department of Energy Energy Frontier Research Center

I would also like to recognize Peter Menard and Garry Barnes at the Center for Clean Energy Engineering (C2E2) for their help with the water flux experiments. They were always available to answer questions about the experimental setup and assist with any problems. I am also grateful for the collaborations and help received from the synchrotron facilities. At the Advanced Photon Source beamline 32-ID, Dr. Steve Wang, Dr. Joan Vila-Comamala, and Alex Deriy were extremely helpful and trusted us to extend the capabilities of their microscope. Also, I received a great deal of help from Douglas van Campen, Dr. Johanna Nelson, Dr. Yijin Liu, and Dr. Joy Andrews at Stanford Synchrotron Radiation Lightsource beamline 6-2. They were always available for conference calls and excited to help with the research. The scientists at the

National Synchrotron Light Source beamline X8C also provided us with ample time on their microscope to run *in situ* experiments. For that, I would like to thank Chris Eng, Dr. Yu Chen Karen Chen-Weigart, and Dr. Jun Wang for their help and access to the TXM.

I also appreciate all of the help provided from past and present lab members who have helped me in my research efforts. I would like to thank Dr. Aldo Peracchio, Prof. George Nelson, and Dr. Arata Nakajo for all of the help and meaningful discussion they have provided. I have had the privilege work with former lab members such as Dr. Kyle Grew, Dr. John Izzo, and Dr. Jeffery Lombardo who have helped guide me through my graduate studies. I would also like to acknowledge my lab members including Timothy Myles, William Harris, Alex Cocco, Matthew Degostin, Timothy Webb, and Kyle Bagshaw.

Finally, I would like to acknowledge my friends and family who have been there for me and helped me through my graduate studies. I owe a great deal of thanks to Kathryn Gosselin for all of the support and encouragement she has provided me. I also want to acknowledge my parents Darlene and Peter Kiss, and my sister Michelle Kiss for all of their help. My family has always been supportive of me furthering my education and has been willing to help whenever possible. My father also provided expertise in manufacturing several components for the experiments and I am grateful for all of the help.

– Andrew M. Kiss

Table of Contents

Chapter 1: Introduction

With increasing energy demands, there is a growing need to produce clean, efficient power. In order to accommodate these energy needs, there has been a drive to decrease greenhouse gas emissions and increasing the efficiency of power generation. Traditionally, much of the power produced is achieved by combustion of fossil fuels. Of the energy used for transportation, 93% of it comes from petroleum based fuels. Electric power generation is largely supported by coal and natural gas power generation, 41% and 24% respectfully. While these technologies have improved, and can achieve high overall efficiency with combined heat and power, a great deal of research has been focused on cleaner and renewable technologies which can help decrease greenhouse emissions (U.S. Energy Information Administration, Monthly Energy Review, January 2014).

Depending on the application, different technologies have started to displace traditional power generation methods. Solutions for portable power such as internal combustion engines for cars are not necessarily an ideal approach for large scale stationary power. The term fuel cells encompasses a broad range of devices which, when selected properly, can be used for portable power or large scale applications. These electrochemical devices are appealing due to their high efficiency and the potential to be carbon neutral (Mench, 2008). A great deal of funding has been allocated to fuel cell technologies and there have been considerable advances in the performance and the lifetime of these devices.

The fuel cell was first discovered by Sir William Grove in 1839 who demonstrated its use with two platinum electrodes in sulfuric acid. Liquid electrolyte alkaline fuel cells were first developed by Sir Francis Bacon in 1930. A push in the development of fuel cells was sparked by the cold war and liquid electrolyte alkaline fuel cells saw significant use in NASA's Apollo

program. With the development of the polymer electrolyte membrane at General Electric in 1955 and the success of a proton exchange membrane PEM, DuPont Nafion 117 PEM, recent advances have focused on a polymer alkaline anion exchange membranes (AEMs). Other fuel cell systems such as solid oxide fuel cells (SOFCs) have evolved over the years to start being options for power applications (Larminie & Dicks, 2003, Mench, 2008).

The AEMs typically suffer from ionic conductivities much lower than PEMs which introduces transport losses and decrease performance. Even though careful design has gone into the membrane design, the hydroxide ions cannot transport across the membrane as easily as their acid counterparts (Varcoe & Slade, 2005). Transport issues are not isolated to the membrane, or electrolyte, and can be found in other components of the fuel cell. Solid oxide fuel cells (SOFCs) have seen acceptable performance from yttria-stabilized zirconia (YSZ) electrolyte but transport losses can found in the anode during degradation. If the nickel present in the anode oxidizes, transport paths can increase in length, electronic conductivity decrease, and separation of the anode from the electrolyte can lead to failure (Faes *et al.*, 2012). Understanding this degradation and how it affects transport can be valuable for extending SOFC lifetimes.

Polymer Electrolyte Membranes

Portable power applications have been investigating low temperature fuel cells such as proton exchange membrane fuel cells (PEMFCs) or alkaline anion exchange membrane fuel cells (AEMFCs) which typically operate below 80 °C. These low temperature fuel cells have a relatively fast start up, high power density, and the ability to utilize liquid alcohol fuels such as methanol which make them appealing for portable power applications. These systems do have some challenges related to water management as well as carbon monoxide and carbon dioxide decreasing performance (Varcoe & Slade, 2005, Yanagi & Fukuta, 2008). As the fuel cell is operating, water is generated and needs to be removed from the electrodes. If the water is not removed, then flooding can occur and gas reactants will not be able to reach the reaction site.

Both PEMFCs and AEMFCs are comprised of a polymer backbone which fixed ionic groups are attached to. A popular PEM made by DuPont, Nafion, is comprised of a polytetrafluoroethylene, PTFE (Teflon), backbone with sulfonic acid ion groups. The Teflon backbone is extremely stable in operating conditions and the sulfonic acid groups provide a highly acidic environment for proton transport. The sulfonic acid anion is a strong acid ($pK_a < 1$) and for a PEMFC, protons are the counter-ions used for transport (Helfferich, 1962). With a strong acid fixed ion group, the protons can dissociate from the fixed ion very easily. A high concentration of dissociated protons in the pores is beneficial for a high ionic conductivity and makes Nafion attractive for fuel cell use (Thampan *et al.*, 2000, Zawodzinski Jr. *et al.*, 1993b).

In order for the protons to dissociate from the membrane, water needs to be available for the ions to dissolve in. In fuel cell membranes, the amount of water, or hydration, can be measured by the ratio of water molecules to fixed ionic groups (Zawodzinski *et al.*, 1991). Water is absorbed into the membrane, forming pores and pathways across the membrane. The backbone is usually hydrophobic and the hydrophilic fixed ion groups will be attracted to the water. When

the membrane is in a low hydration state, dissociating ions can create a high concentration in the pore solution. Thermodynamically, this can be unfavorable so a small fraction of ions will dissociate. At higher hydrations, the pore concentration will drop and a higher fraction of ions can dissociate from the sulfonic acid groups (Choi *et al.*, 2005, Thampan *et al.*, 2000).

Water is not only responsible for the dissociation of the ions but is also vital for transport of ions through the membrane. Once the protons are dissociated from the membrane, water will bond and solvate the ion. This solvated proton, or hydronium (H_3O^+), can then transport through the membrane by several modes such as facilitated transport, migration, and bulk and Grotthuss diffusion mechanisms. Of these, the most dominant transport paths will occur through the pore solution being bulk and Grotthuss diffusion mechanisms (Choi *et al.*, 2005, Grew & Chiu, 2010).

Given water's importance for both the dissociation of ions as well as transport across the membrane, it should be well understood in the membrane. Water transport in PEMs has been extensively studied using many different techniques. Several types of experiments have been used to understand water transport in membranes including nuclear magnetic resonance (NMR) (Zawodzinski Jr. *et al.*, 1993a, Zawodzinski Jr. *et al.*, 1993b, Zawodzinski *et al.*, 1991), absorption (Hinatsu *et al.*, 1994, Majsztrik *et al.*, 2007, Satterfield & Benziger, 2008), and water permeation methods (Ge *et al.*, 2005, Motupally *et al.*, 2000). These techniques have been able to measure hydrations, effective diffusion coefficients, and interface resistances.

While PEMs and Nafion are well studied in the literature, there is relatively little reported in the literature on AEM water transport. The U.S. Army has shown an interest in using alkaline anion exchange membrane fuel cells (AEMFCs) for portable power applications. This technology shows the potential to replace batteries, providing power for soldiers in the field and allowing for fast refueling. The AMFC uses an alkaline polymer membrane electrolyte. Because

of the alkaline conditions, the AMFC is capable of operating on hydrogen or alcohol fuels and can use non-platinum catalyst alternatives including metals such as silver or nickel, among others (Larminie & Dicks, 2003, Spendelow & Wieckowski, 2007, Varcoe & Slade, 2005). AMFCs transport hydroxide ions from the cathode to the anode, which can help reduce fuel crossover. Materials and synthesis procedures have improved; however, substantial challenges regarding the thermal, chemical and mechanical stability, as well as the ionic conductivity, of these AEM materials still need to be addressed (Danks *et al.*, 2003, Slade & Varcoe, 2005, Varcoe & Slade, 2005, Varcoe, 2007).

Nafion PEM has received significant attention for several reasons including its ionic conductivity and chemical stability. When considering AEMs, there is not one popular membrane which is available for researchers to study. Instead, there are many different backbone-fixed ion combinations available. It is common for current AEMs use benzyl-trimethylammonium fixed side chain groups, however others are being investigated. This cation is a strong base ($pK_b < 1$) which allows for reasonable dissolution of the hydroxide ions (OH^-) from the membrane and easy transport through the membrane (Helfferich, 1962). The polymer backbone can range from several polymers including poly(ethylene-co-tetrafluoroethylene) (ETFE), poly(tetrafluoroethylene-co-hexafluoropropylene) (FEP), polypropylene, and polysulphone (Slade & Varcoe, 2005, Varcoe, 2007, Varcoe & Slade, 2006, Varcoe *et al.*, 2007, Vega *et al.*, 2010).

Each backbone-fixed ion combination will generate its own unique water and ion transport properties. These can even vary within the same combination when changing membrane properties such as ion exchange capacity (IEC), or the number of fixed ion groups per mass of membrane. Membranes can be designed to consider how changing these properties

might affect the water uptake might change in order to maximize ion transport through the membrane. Even by trying to tailor membranes for high ionic conductivity, AEMs reported in the literature still suffer from a low ionic conductivity when compared to their PEM counterparts as well as degradation. In one study, a fully hydrated AEM with an ETFE backbone was reported to have an ionic conductivity of roughly 30 mS/cm at 30 °C. When comparing this to Nafion 115 PEM, which has a similar IEC, the PEM has a much higher ionic conductivity around 90 mS/cm (Varcoe, 2007).

While a membrane might be manufactured with a desired IEC, there are several pathways for membrane degradation which could decrease the number of fixed ions. Membranes are fairly stable when in the chloride ion form, however the ion exchange to the hydroxide ion form can cause substantial degradation. The ion exchange procedure typically involves soaking the membrane in a high concentration of potassium hydroxide (1 M KOH) so that the chloride ions will be displaced. This highly basic solution has shown degradation effects for the membrane which can lead to failure (Vega *et al.*, 2010). The membrane should be able to withstand a highly basic environment since it is desirable to create a high concentration of hydroxide ions in the pore solution. The hydroxide ion has been shown to attack the membrane using several mechanisms including nucleophile displacement and Hofmann elimination (Arges & Ramani, 2013, Varcoe & Slade, 2005). These degradation mechanisms remove or deactivate the quaternary ammonium groups from the membrane and decrease the IEC. As the membrane degrades, the ionic conductivity will decrease and in some extreme cases, membrane failure can occur (Vega *et al.*, 2010).

Instead of operating in a hydroxide form, if the membrane is exposed to carbon dioxide (CO_2), then the hydroxide ions can be displaced by the formation of carbonate (CO_3^{-2}) and

bicarbonate (HCO_3^-) ions. This can affect the membrane in several ways. One effect is the decrease in pH, which might actually work to increase the stability of the membrane (Vega *et al.*, 2010). However, the same ion exchange process also reduces the ionic conductivity of the membrane. This happens because the carbonate species displace the hydroxide ions which can transport more easily through the membrane than the carbonate species (Grew *et al.*, 2011). Fortunately, the carbonate species can be removed from the system using a self-purging mechanism (Fukuta *et al.*, 2009, Matsui *et al.*, 2010, Yanagi & Fukuta, 2008). Also, operating the fuel cell in a CO_2 free environment allows for the hydroxide ions to replace the carbonate species (Yanagi & Fukuta, 2008). The presence of carbonate and bicarbonate can also influence the AEMFC's electrochemical kinetics.

It would be useful if an experimental setup could be designed to provide the information necessary to measure an effective water-membrane diffusion coefficient which is dependent on the local hydration and temperature in the membrane. From the list of techniques used for studying water transport in Nafion, a permeation based approach could be used to measure an effective water-membrane diffusion coefficient as a function of hydration based on water flux measurements. Once it is understood how water transports throughout the membrane, principles from kinetic theory can be applied to scale the water-membrane diffusion coefficient to an ion-membrane diffusion coefficient. With an assumed hydration in the membrane, the dissociated concentration of ions can be solved. Finally, using some modeling approaches and the diffusion coefficients, the ionic conductivity of the membrane can be calculated as a function of the hydration.

Solid Oxide Fuel Cells

While portable power applications have been focusing on low temperature fuel cells, stationary power applications tend to consider intermediate or high temperature fuel cells. Solid oxide fuel cells (SOFCs) are one high temperature fuel cell technology which has been receiving attention. These systems typically operate between 600 and 1000 °C and unlike low temperature fuel cells, do not have to worry about water management and flooding. Using higher operating temperatures, SOFCs have the ability to internally reform fuel, use low cost catalyst materials, and exhaust high quality steam byproduct which can be used for heating and air conditioning (Larminie & Dicks, 2003, Mench, 2008). This technology is starting to reach maturity and companies, such as Bloom Energy (Sunnyvale, CA), are starting to produce SOFC systems. Much of the research on SOFCs has been focusing on degradation and extending the life of these systems.

In state of the art anodes, a combination of yttria stabilized zirconia (YSZ) and nickel are used as ionic and electronic conductors respectively. The low cost of Ni combined with its electronic and catalytic properties make it desirable for minimizing cost while maintaining performance. These fuel cell anodes are typically composed of small particles forming an active electrode which is usually 5 to 10 μm thick (Sarantaridis & Atkinson, 2007). The combination of Ni/YSZ for an anode material has satisfactory performance however changes in the microstructure during operation can lead to degradation (Laurencin *et al.*, 2009, Sarantaridis & Atkinson, 2007, Sarantaridis *et al.*, 2008). While several degradation processes occur, chemical changes, such as oxidation of nickel (Ni) to nickel oxide (NiO), are especially significant because there is a decrease in the performance. The oxidation of Ni has a significant volumetric change which will affect the microstructure, connectivity of the electronically conducting Ni phase, electrochemically-active three phase boundaries, and increases stresses between solid

phases which can lead to fractures in the anode. In order to improve the lifetime of these devices, research is needed to understand the degradation mechanisms and how they can be minimized.

While nickel is found in SOFC anodes, it has also become an attractive metal for energy materials that are found in supercapacitors and batteries (Ayeb *et al.*, 2006, Inamdar *et al.*, 2011, Meher *et al.*, 2010, O'Grady *et al.*, 1996, Uchimoto *et al.*, 2001). The reduction and oxidation (redox) processes of Ni have been extensively studied in an effort to understand and improve electrodes. The surface morphology of electrodes in supercapacitors has had a significant effect on performance (Inamdar *et al.*, 2011, Meher *et al.*, 2010). For example, the nano-structure of the electrode can be tailored to help maximize the surface area resulting in more active area and greater capacitance. The redox of Ni has also been studied in nickel-metal hydride and lithium ion batteries (Ayeb *et al.*, 2006, O'Grady *et al.*, 1996, Uchimoto *et al.*, 2001). By understanding the oxidation state of the Ni in the electrode, degradation in the battery can be further deduced.

The oxidation of nickel to nickel oxide (NiO) is the redox processes of interest. The chemical reaction results in a volume increase based on density data of 69.8% (Green & Perry, 2008). This change in volume can increase stress between solid phases and lead to cracks at the nanometer scale. These complex interactions and phase transitions occurring at the tens of nanometer scale involve many compounds at high temperatures and are difficult to study with existing analysis techniques. There are many techniques which have been used to study nickel oxidation such as secondary ion mass spectroscopy (SIMS) (Atkinson & Taylor, 1978, Atkinson *et al.*, 1979), scanning electron microscopy (SEM) (Tikekar *et al.*, 2006), thermogravimetric analysis (TGA) (Carter, 1961, Faes *et al.*, 2011, Haugsrud, 2003, Karmhag *et al.*, 1999, Waldbillig *et al.*, 2005, Young *et al.*, 2007), environmental transmission electron microscopy (eTEM) (Jeangros *et al.*, 2010), and environmental scanning electron microscopy (eSEM)

(Klemensø *et al.*, 2006). These techniques can be divided into two categories: *in situ* and *ex situ* techniques. With the *ex situ* techniques such as SIMS or SEM, a chemical reaction cannot be studied as it is occurring. The advantages for these methods are SIMS can provide species concentrations in the sample while SEM micrographs can image the microstructure down to the nanoscale. In order to study a reaction, a sample can be investigated at different time steps. In contrast, *in situ* techniques can provide information as the reaction is occurring. A technique like TGA measures the mass change over time which can be used to calculate the reaction rate. However, this technique does not provide any information about the microstructure of the sample. A combined technique that can image the microstructure while the reaction is occurring would be desirable. This has been accomplished by using an eTEM or eSEM. Samples can be studied using the microscope while only at low pressures, up to 10 mbar. While this technique is useful, in order to study nickel oxidation in operating SOFC conditions, the instrument will need to be able to operate at higher temperatures and atmospheric pressures.

Using these techniques above, a wide range of reaction rates and activation energies have been reported. For example, the range of activation energy values range from 37 to 250 kJ/mol (Atkinson, 1985, Haugsrud, 2003, Modena *et al.*, 2006, Waldbillig *et al.*, 2005). There are several factors which could lead to this large discrepancy including the technique used, the differences in the sample and sample preparation, and the conditions in which the sample is studied. Having a detailed understanding of the reaction and accurate reaction rates would be beneficial for the scientific community and can be used to help understand degradation in SOFC anodes.

One approach which can be used to image the nickel oxidation reaction is by using a synchrotron based full-field transmission X-ray microscope (TXM) (Liu *et al.*, 2013, Shen *et al.*,

2007). This instrument can provide the high resolution which is required to observe the nanoscale changes in the sample. Several TXMs are located synchrotrons around the country including the Advanced Photon Source (APS) at Argonne National Laboratory, Stanford Synchrotron Radiation Lightsource (SSRL) at the Stanford Linear Accelerator Center, and National Synchrotron Light Source (NSLS) at Brookhaven National Laboratory. By using the TXM at one of these facilities, a high brilliance, tunable X-ray source can be utilized. By changing the energy level of the incoming monochromatic X-rays, absorption techniques can be used to identify the chemical species and oxidation state of the sample (Nelson *et al.*, 2011). With the instruments ability to image the sample and identify the oxidation state, all that is needed is an environmental chamber to control the temperature and gas environment around the sample. The TXM can operate with the sample exposed to ambient air and does not require a vacuum or low pressure to operate. Therefore, this work seeks to expand the capabilities of the TXM to include *in situ* chemical reactions and create a high temperature controlled gas environment to study the sample in. Using the images of the oxidation, modeling efforts can be used to analyze the images and solve for an oxidation reaction rate and activation energy. Once this technique has been demonstrated and validated for simple reactions such as oxidation of nickel particles, the experiments can be expanded to understanding degradation in Ni/YSZ anodes. This knowledge can then be applied to design anodes that are less susceptible to oxidation degradation. By reducing oxidation and transport losses in these anodes, the lifetime of these devices can be extended.

Chapter 2: Alkaline Anion Exchange Membranes

Introduction

Polymer electrolyte membranes are typically used in low temperature fuel cell applications for transporting ionic species. These membranes are composed of a polymer backbone with ionic side chain groups. The backbone material varies between different membranes and can include polypropylene (Vega *et al.*, 2010), fully or partially fluorinated carbon chains (Varcoe, 2007), polysulfone (Arges & Ramani, 2012) and a wide variety of polymers (Merle *et al.*, 2011). The side chain groups are attached to the polymer backbone and typically terminate in an ionic group which is used to help transport species. Several fixed ionic groups are used including one popular option for alkaline anion exchange membranes (AEMs), quaternary ammonium (Varcoe & Slade, 2005). These membranes have a specific goal of transporting the ions across the cell while separating the fuel and oxidizer. Depending on the operating conditions of the fuel cell, the transport of these ionic species can contribute to significant performance losses. The ionic conductivity of these membranes is strongly dependent on the amount of water present in the membrane, or hydration of the membrane (Grew & Chiu, 2010). In order to study ion transport to minimize losses in these membranes, it is important to first understand water transport.

In an operating alkaline anion exchange membrane fuel cell (AEMFC) water is produced at the anode while it is consumed to form hydroxide ions at the cathode. While the hydroxide ion is transporting across the membrane from cathode to anode, electro-osmotic drag will pull water molecules along with the ion. This can create a significant concentration gradient between the anode and cathode for diffusion of water. The ionic conductivity of the membrane is strongly dependent on the hydration of the membrane and if the membrane became too dry and dropped

below a percolation threshold, then there would not be any transport paths for the ions. To prevent dry out conditions at either electrode, humidified gases are used. Water management is extremely important and one way to improve fuel cell performance is to understand water transport so that the system is operating at ideal conditions.

The water-membrane diffusion coefficient has been extensively studied in the PEM literature however there is limited work done studying AEMs. Even though many groups have studied the water-membrane diffusion coefficient of Nafion, there are reported values in the literature which spread orders of magnitude (Ge *et al.*, 2005, Hallinan & Elabd, 2009, Motupally *et al.*, 2000). In general, as the hydration increases in the membrane so does the diffusion coefficient. Some works have reported a characteristic peak at low hydrations. This local maximum is due to the Darken factor which is a correction for non-uniform activity coefficients (Zawodzinski *et al.*, 1991). The Darken factor, which is dependent on the local activity and hydration, can be multiplied by the Fickian diffusion coefficient to calculate a water-membrane diffusion coefficient.

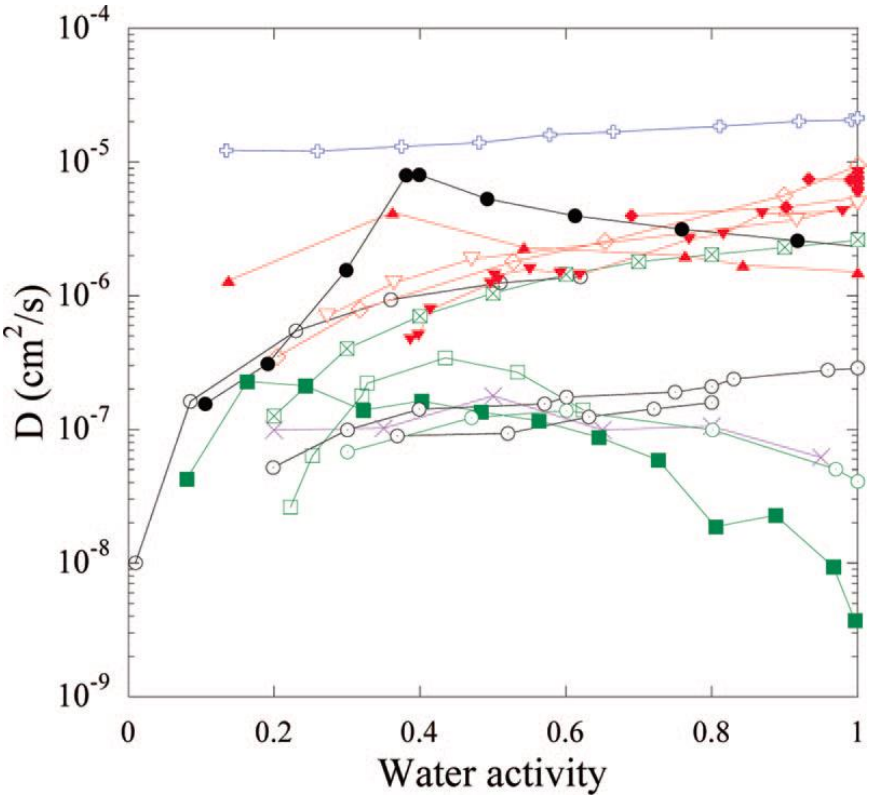

Figure 2.1: A range of water-membrane diffusion coefficients for Nafion using different experimental techniques (Hallinan & Elabd, 2009).

Water transport in polymer electrolyte membranes has been studied using several different experimental setups and approaches including nuclear magnetic resonance (NMR), absorption, and permeation based techniques. Using NMR, several important membrane characteristics can be measured such as the ion exchange capacity (IEC), membrane degradation, and the water-membrane diffusion coefficient (Arges *et al.*, 2012, Arges & Ramani, 2013, Zawodzinski Jr. *et al.*, 1993a, Zawodzinski *et al.*, 1991). When operating the NMR, the membrane is in equilibrium with the surrounding environment and will have the same hydration throughout the membrane. Hydration is not important for measuring the IEC or degradation, but

the water-membrane diffusion coefficient is strongly dependent on hydration. Therefore, each trial will need to be taken at a single hydration which can take 4 days to reach steady state (Zawodzinski *et al.*, 1991). NMR is a powerful technique but requires the instrumentation as well as knowledge to operate the device and interpret the results.

For dynamic measurements, researchers have chosen to use absorption and desorption methods by measuring the mass change of the membrane over time to determine water transport properties (Majsztrik *et al.*, 2007, Satterfield & Benziger, 2008). This typically involves suspending the membrane in a temperature controlled chamber above water to measure water absorption or a desiccant to measure water desorption. Based on how the mass changes, absorption and desorption resistances can be measured along with the water membrane diffusion coefficient. Using this setup, the membrane is not constrained and subject to the same external forces it might encounter in an operating fuel cell. As the membrane is absorbing water, it will expand as the pores open and the morphological changes can be difficult to consider from the results.

Water transport can also be studied using permeation based experiments (Ge *et al.*, 2005, Kiss *et al.*, 2013b, Motupally *et al.*, 2000, Myles *et al.*, 2011). Using a water concentration gradient, the amount of water transporting across the membrane can be measured. This typically involves running a high relative humidity gas or liquid water on one side of the membrane and dry gas other the other. The exhaust gases can be analyzed or the water trapped using desiccants to determine the water flux across the membrane. A permeation based technique can be used to consider interface effects such as absorption and desorption as well as measuring the water-membrane diffusion coefficient as a function of hydration. Although careful calibration and

modeling are required, this setup most closely resembles conditions the membrane would see in an operating fuel cell and was chosen in this set of experiments to study water transport.

It is always important to understand which phenomena need to be considered when performing experiments. In this system, possible water transport resistances exist at the gas-membrane interfaces as well as diffusion resistance through the membrane. Some researchers have reported possible absorption and desorption effects at the interfaces (Ge *et al.*, 2005, Majsztrik *et al.*, 2007). Including these phenomena affect the values calculated for the effective water-membrane diffusion coefficient in the membrane. There is a significant spread in the reported values of water-membrane diffusion coefficients for some membranes such as a proton exchange membrane Nafion (Hallinan & Elabd, 2009, Motupally *et al.*, 2000). Some differences in values are expected due to the approach taken and experimental error. However, it is important to address the fundamental issues and isolate which transport resistances are significant. To determine which transport resistances are most significant, the same membrane of different thicknesses can be used in a permeation based experiment.

The ultimate goal of this experiment is to determine transport properties of ions and water in fuel cell membranes. The permeation based experiment will measure water flux across the membrane. Using numerical models, an effective water-membrane diffusion coefficient as a function of hydration can be selected which best fits the experimental water flux results. The water-membrane diffusion coefficient can be scaled to an ion-membrane diffusion coefficient for hydroxide, carbonate, and bicarbonate using principles from kinetic theory. With these diffusion coefficients, the ionic conductivity of the membrane can be calculated as a function of hydration. The dissociation of the mobile species is also of interest and can be investigated using the ionic conductivity calculations.

Experimental Setup

As explained above, a permeation based experiment was chosen for this experimental setup. This technique creates a concentration gradient across the membrane by using two gas streams: one humidified to a high relative humidity and one completely dry. The water which transports across the membrane is collected in desiccants and the change in mass of the dry side desiccant is used to measure a water mass flux. This setup has several major components which help achieve the correct environment to study water transport and can be seen in Figure 2.2.

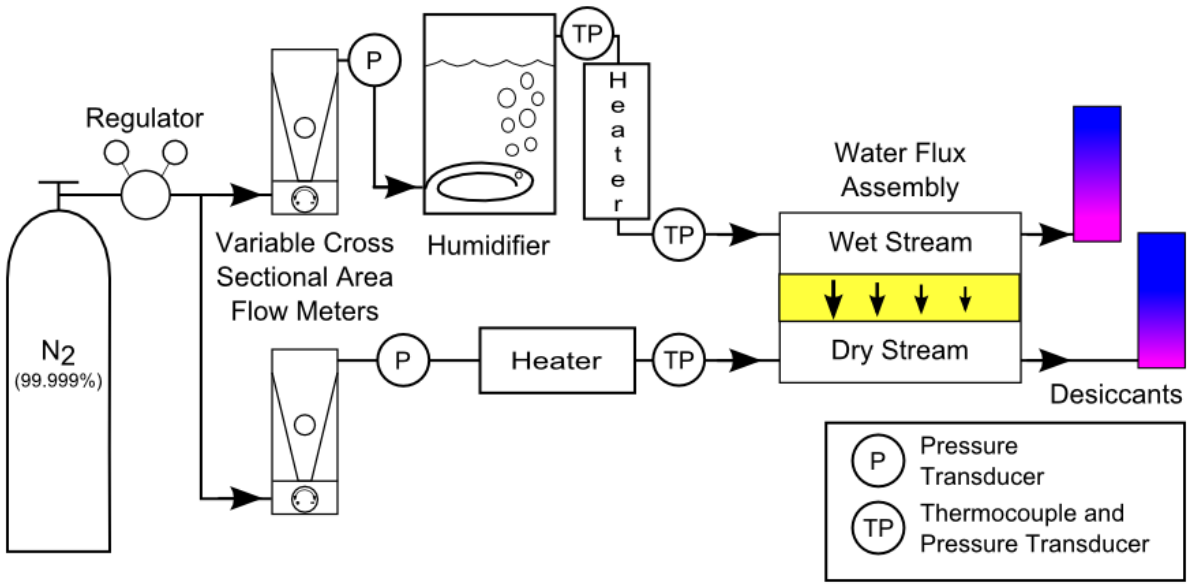

Figure 2.2: A schematic of the experimental setup (Kiss *et al.*, 2013b). The wet stream is humidified using a bubble humidifier before entering the water flux assembly. The arrows through the yellow membrane indicate mass transfer through the membrane. The water is collected using indicating desiccant.

Components

The experiment requires the flow of gases which will create the concentration gradient across the membrane. A tank of ultra-high purity nitrogen (99.999%) is used to carry water through the membrane assembly. The high purity nitrogen is required to minimize contamination from carbon dioxide in the membrane. The nitrogen is split into two gas streams which are controlled independently by Matheson Trigas FM-1050 variable cross sectional area flow meters, or rotameters. The dry side gas stream flow is regulated by the rotameter and then heated to the operating temperature of the cell. The wet side gas stream is also controlled by the rotameter but also needs to be humidified to the desired relative humidity. The nitrogen enters a bubble humidifier and leaves almost fully saturated with water. A significant amount of calibration and care goes into understanding and controlling the water output from the humidifier and will be explained in the following sections. The gas is heated to the operating temperature of the membrane to prevent condensation in the gas lines and minimize temperature gradients in the membrane assembly. The two gas streams are controlled independently in order to minimize the pressure difference between the two gas streams entering the water flux assembly. If a total pressure (water and nitrogen) gradient existed, it could skew the water flux results. Controlling the cell inlet pressure can cause the flow rates in the two gas streams to be different but they are usually close in value. The flow rate in each stream can be measured using the rotameters and a digital flow meter at the exit of the desiccants.

The wet side gas stream needs to be humidified to the desired relative humidity and this is accomplished using a bubble humidifier (Scribner Associates Inc., Southern Pines, NC). The humidifier is a sealed container with a water bath inside. The dry nitrogen gas enters the humidifier and bubbles through the water bath. This should fully saturate the nitrogen gas with

water. The gas then leaves the top of the humidifier with a high relative humidity and at the water bath temperature. There are two thermocouples in the humidifier: one to control the water bath temperature and a feedback thermocouple at the top of the chamber to monitor the exit gas temperature. The water bath temperature should be controlled to the temperature corresponding to the desired water partial pressure for the membrane assembly. The exit gas thermocouple is more sensitive to system changes such as gas flow rate and the ambient temperature. The humidifier is wrapped in electric heaters which are controlled by temperature controllers. The water bath temperature, depending on flow rate, is typically a few (2 – 4 °C) degrees greater than the thermocouple for the exhaust gas.

Since water diffusion through the membrane is the focus of this study, some care should be taken to achieve the best results. When filling the water tank, be sure to use deionized water from the water filter. The water should be rated for 18 MΩ or better to ensure that other species in the water have been removed. Exposure to ambient air should be minimized to prevent absorption of carbon dioxide. Some membranes can be sensitive to the presence of carbon dioxide and if it is found in the water, it can contaminate the gas stream and membrane.

Since the nitrogen is bubbling through the water bath, it is important that the water level remain at a constant height. As the experiment runs, water is removed from the humidifier and the water level will drop. If the water level is too low, then the nitrogen bubbles might not saturate before leaving the humidifier. In order to minimize the effect of water level, a float switch is utilized from inside the humidifier. When the water level drops below a certain level, the float switch trips a relay which turns on a water pump. This pump fills the humidifier with water until the water returns to a satisfactory level for the float switch and turns off the pump.

This method helps maintain a constant water level in the humidifier and repeatable results from the humidifier.

Electric heaters with temperature controllers are used to control the temperature and gas environment throughout the experiment. Omega CNi32 temperature controllers using a proportional-integral-derivative (PID) algorithm control the temperature of the experiment within ±0.5 °C of the set point value. The PID algorithm helps the temperatures remain stable and minimize fluctuations based on changes to the system. The temperature controllers get feedback from Omega K-type thermocouples. Temperature controllers and heaters are used to control the humidifier water bath temperature, heat the wet and dry gas lines and the water flux assembly. The humidifier uses an electric pad heater which wraps around the humidifier chamber. The wet and dry gas lines use an electric heating tape which is wrapped around the lines. The membrane assembly is heated using two cartridge heaters inserted into the back plates to maintain the operating temperature.

A power supply (Agilent E3630A) is used to power several pressure transducers (Druck PTX 1240). The pressure transducers require 9-30 VDC and output a 4-20 mA signal proportional to the pressure. The operating range of the transducers is 0-103 kPa (0-15 PSIG). The pressure is important in the system for calculating the humidifier water output and minimizing pressure gradients in the water flux assembly. For the water flux measurement, pressure effects should be minimized to isolate diffusion as the only transport mechanism and the total pressure should be the same on both sides of the membrane. Also, since the nitrogen is compressible, the pressure will be higher at the entrance to the flow channel before it travels through the long and tortuous flow channel. The pressure drop will increase the volumetric flow rate which can be accounted for in the numerical model.

The thermocouples and pressure transducers can be connected to a data acquisition instrument (DAQ) (Agilent 34970A) and recorded by the computer. The thermocouples output a potential which can be directly read by the DAQ. As mentioned above in the section describing the pressure transducers, the pressure transducers output a current which can be read by the DAQ by reading the voltage across a resistor. The DAQ is connected to the computer using a USB to GPIB converter. By using this, a GPIB card is not required in the computer. There are two versions of the Agilent software. The older version (1.0) allows for a more freedom for the user to create a custom interface. Once the system is calibrated, export the setup to save a backup. The runs typically acquire data every minute in order to track temperature and pressure changes. The data can be exported as a *.csv file for further analysis with Microsoft Excel.

To ensure that the humidifier is working correctly and to measure water flux, two desiccants are used to collect the water leaving the water flux assembly. The hot gases carry the water into a laboratory gas drying unit filled with indicating Drierite (Drierite, Xenia, OH). The gas drying units hold roughly 570 g (1.25 lb) of Drierite which can absorb up to 50 g of water. The calcium sulfate ($CaSO_4$) desiccant absorbs nearly all the water in the gas stream, leaving the nitrogen with a dew point of -73 °C. In this desiccant there is roughly 2% cobalt chloride ($CoCl_2$) which is used as the indicator. When the desiccant is blue, it is dry and able to absorb water. Once it absorbs water, a color change from blue to pink indicates that the desiccant is saturated and should be regenerated. There is a desiccant on each side of the membrane in order to measure the total amount of water which has left the humidifier, or considering only the desiccant tube on the dry side, the amount of water which has transported across the membrane. The mass of the desiccant tubes is measured using a precision scale (OHAUS Adventurer Pro AV3102C) which is accurate to 0.01 g.

The membrane assembly is where the water transport will actually take place in the experiment. An assembly was used from Fuel Cell Technologies that utilized a single serpentine flow channel and would have a cell active area of 50 cm^2 (Fuel Cell Technologies 50SCH, Albuquerque, NM). The wet and dry gas streams enter the assembly through heated stainless steel back plates. The gas is then directed into graphite flow channels. The wet and dry flow channels run parallel to each other and are arranged in a serpentine pattern to maximize path length along the membrane. The flow channels are only separated by the membrane. This allows for the water in the wet gas stream to transport across the membrane into the dry gas stream. The entire assembly is held together using 8 bolts which are torqued to 5.65 N-m (50 in-lb).

Several different membranes were studied using this experimental setup. The membranes were installed between the two flow plates into the membrane assembly. It should be noted that only the membrane was used in this testing. The water transport through the membrane was the focus of this work and in order to properly study this, any other variables should be removed including catalyst and gas diffusion layers. Although studying water transport through AEMs was the objective of this experiment, a validation was performed using a popular proton exchange membrane, DuPont Nafion 117, purchased from Ion Power (New Castle, DE). Once validated, water transport studies were performed using SnowPure Excellion I-200 (San Clemente, CA) and AEMs received through a collaboration with Illinois Institute of Technology (IIT). The SnowPure Excellion I-200 AEM has a polypropylene backbone and quaternary ammonium side chain groups (Vega *et al.*, 2010). The AEMs received from IIT, also used quaternary ammonium side chain groups but used a polysulfone backbone (Arges *et al.*, 2012). The AEMs were received in the chloride ion form for stability. The experimental setup outlined

can be extended to study a broad range of membranes to arrive at properties which are dependent on the hydration of the membrane.

Calibration

Pressure Transducers

There are pressure transducers located throughout the experimental setup and it is important that the 4-20 mA output is interpreted properly. As seen in experimental schematic, pressure transducers are located at the entrance and exit of the humidifier, after the rotameter for the dry side gas stream, and in both gas streams entering the water flux assembly. The pressure transducers are powered using a 20 V output in the front of the power supply. The output current is converted to a voltage using a resistor.

To calibrate the pressure transducers, the Center for Clean Energy Engineering (C2E2) maintains a portable calibration instrument (Druck DPI 603). Installing the pressure transducers into this device allows the user to pressurize the pressure transducer. The instrument displays the pressure and the DAQ software can read the voltage measurement. The voltage response can be recorded for multiple pressures. The relationship between the pressure and voltage for the pressure transducers is linear and a calibration curve can be calculated for each pressure transducer. The slope might change between pressure transducers based on the exact value of the resistor.

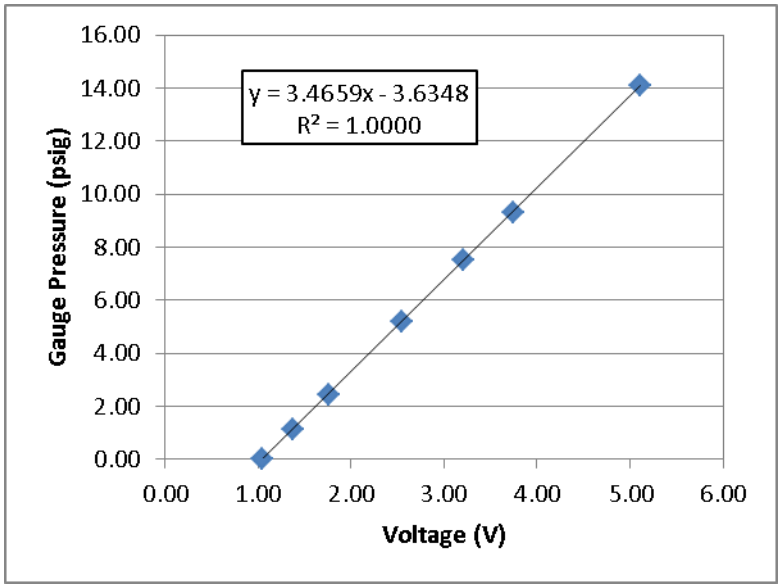

Figure 2.3: A representative calibration curve for a pressure transducer. As indicated by the R^2 value, the equation agrees with the data points and can be used accurately to measure the pressure.

Nitrogen Gas Flow Rate

Nitrogen gas is used as an inert carrier for the water vapor. As the nitrogen flow rate on the wet side increases, it will cause more water to travel into the water flux assembly. Measuring the nitrogen flow rate is important to ensure that the desired relative humidity and water entering the water flux assembly is achieved. The rotameters have a scale and calibration curves can be downloaded for different gases. It is important to consider testing conditions and the calibration curves are performed at 70 °F and 0 or 20 PSIG. Correction factors exist such that the calibration curves can be adjusted for temperature, pressure, and gas composition.

Another approach is to use the rotameter readings as a guide and to directly measure the flow rate using a digital flow meter. An Alicat mass flow meter (Alicat Scientific M0-5SLP) was acquired which could display the flow rate of the gas stream. The mass flow meter measures the flow rate based on a pressure difference through laminar plates. Nitrogen can be selected from a

list of preprogrammed gases and the mass flow rate can be calculated directly on the device using internal temperature and pressure measurements. It is also important to give the instrument 30 minutes to warm up in the device to reach thermal equilibrium so that the readings are consistent.

Temperature Control

The temperature measurements and control are important in the system to control the relative humidity and preventing condensation in the system. Omega K-type thermocouples are used in the experiment. Depending on the measurement, the thermocouple wires may travel to the data acquisition instrument and/or a temperature controller. A common way to calibrate thermocouples is to use two phase solutions such as ice or boiling water where the temperatures are well defined. The temperature controllers can be calibrated by submerging the thermocouple in ice water for an hour, to make sure the thermocouple bead has reached thermal equilibrium, and then setting the device to 0.0 °C. When performing this calibration, the data acquisition software did not read 0.0 °C and instead had an offset of 1-2 °C, depending on the thermocouple. This offset also existed at elevated temperatures where the experiment would be operating. Because of this difference, a decision was made to assume the temperature controller correct since it was calibrated at 0.0 °C and it would be controlling the heaters. The data acquisition software was corrected using a linear formula to match the temperature controller value. Both the temperature controller and the data acquisition board have internal temperature corrections to account for any potential at the junction of the device and the thermocouple wire.

The temperature controllers power electric heaters in the system and it is important for the components to maintain a constant temperature. An under-damped system with large

temperature oscillations is not desirable since that might cause condensation in the gas lines. The temperature controllers use PID algorithms which can be tuned for each component to provide the most consistent temperature possible. When the temperature controllers are powered off for an extended period, or reset to their factory configuration, the temperature controllers default to a PI algorithm which can cause significant oscillations in the temperature. Therefore, it is important to change this setting and then perform the auto-tune routine. This tests the heaters and measures the response in the system to minimize oscillations and help maintain a constant temperature.

Humidifier Theory and Calibration

Unfortunately, experiments have demonstrated that the humidifier water output is not proportional to nitrogen volumetric flow rate. As the flow rate increases, there is more significant back pressure through the membrane assembly. The flow channels in the water flux assembly have a small hydraulic diameter which increases the friction and the pressure in the system. As the back pressure in the system increases, the water partial pressure out of the humidifier remains constant and is only a function of temperature. If pressure effects from back pressure are negligible, then an ideal gas relationship can be used to arrive at the expected amount of water output. The mass flow rate of water exiting the humidifier, $\dot{m}_{H_2O}$, is related to the water partial pressure, P_{H_2O}, molar mass of water, W_{H_2O}, universal gas constant, R, absolute temperature of the ambient, T_{atm}, and volumetric flow rate of nitrogen at atmospheric conditions, $\dot{V}_{H_2O}$. This equation is plotted in Figure 2.5 as the "Ideal Gas" line.

$$\dot{m}_{H_2O} = \left(\frac{P_{H_2O} W_{H_2O}}{R T_{atm}}\right) \dot{V}_{atm} \qquad [2.1]$$

However these back pressure effects are not negligible so control volume analysis can be used to perform a mass balance in the humidifier to derive the water mass flow rate as a function of nitrogen flow rate and back pressure. The control volume used for analysis is shown as Figure 2.4.

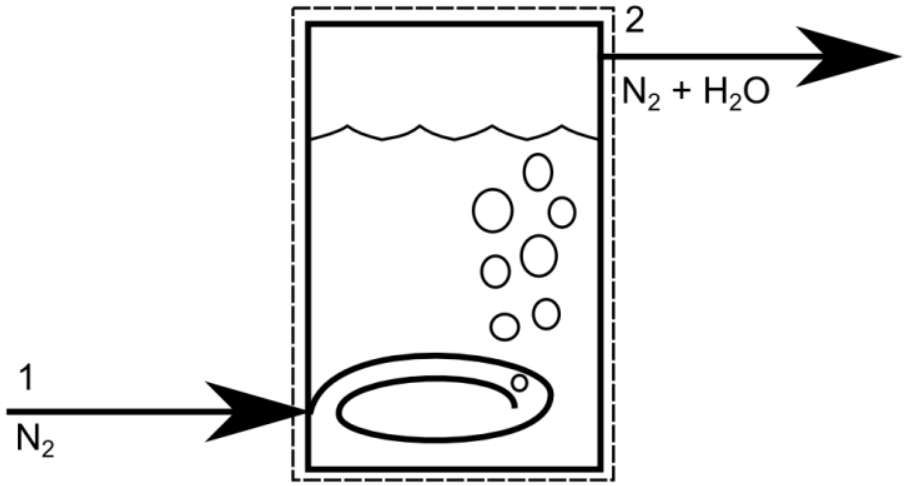

Figure 2.4: A schematic showing the control volume used to calculate the water mass flow rate out of the humidifier. Dry nitrogen is entering the humidifier at (1) and fully saturated water and nitrogen is leaving at (2).

Considering a mass balance of nitrogen, an expression can be solved to find the volumetric flow rate of nitrogen at (2). Using this expression, the mass flow rate of water output from the humidifier can be solved using Equation 2 below where P_2 is the pressure at (2). The results are plotted in Figure 2.5 as "Mass Balance".

$$\dot{m}_{H_2O} = \left(\frac{P_{H_2O}}{P_2 - P_{H_2O}}\right)\left(\frac{P_{atm}W_{H_2O}}{RT_{atm}}\right)\dot{V}_{atm} \qquad [2.2]$$

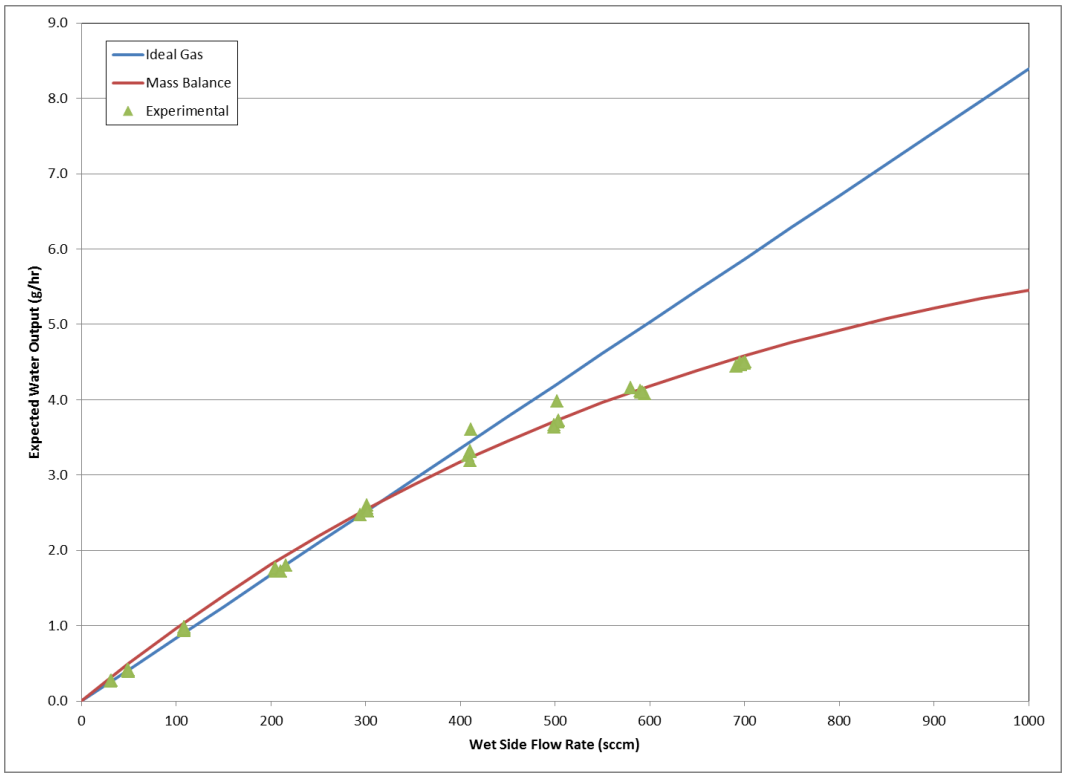

Figure 2.5: Comparison of two different models and experimental values. As the flow rate increases, the pressure in the humidifier increases which causes less water to leave the humidifier. This is captured using the "Mass Balance" model but not the "Ideal Gas" model. The symbols are experimental results.

Running the humidifier and collecting the water output from the humidifier, several variables such as the water mass flow rate, the humidifier pressure and volumetric flow rate can be directly measured. Equation 2.2 can then be rearranged to solve for the effective partial pressure of water output from the humidifier. This can water pressure can then be related back to an effective humidifier temperature. This temperature is lower than the values which are reported from the water bath temperature and the above water thermocouples. This is significant since it was previously assumed that if the water bath was 50 °C, then the nitrogen would come out with

the saturation partial pressure of water at 50 °C. This offset is fairly constant and can be related to the above water temperature as seen in Figure 2.6a.

In order to calibrate the humidifier, two procedures were performed: one to check the set point temperature effect and another for nitrogen flow rate effect on water output. Initially, the water output was measured for different water bath temperature while the nitrogen flow rate remained constant. Linear relationships were calculated for the relationship between the set point on the temperature controller and the water bath temperature, above water temperature, and effective humidifier temperature. These relationships can then be used to arrive at the desired water output for the experiment. If a water partial pressure for 50 °C is desired, then the user can use these relationships to set the temperature controller.

The set point temperature to effective humidifier temperature relationship was performed at a constant nitrogen flow rate so the effect of nitrogen flow rate needs to be considered. The set point of the humidifier was set to 53.7 °C, using the relationships calculated in the previous step so that effective humidifier temperature is 50 °C. The nitrogen flow rate was then varied from 100 to 900 sccm. Unfortunately, no clear trend is available from the experimental data seen in Figure 2.6b. There is an offset between the water bath temperature and the above water and effective temperatures but no distinct trend. The effective temperature was calculated based on the above water temperature and is seen to agree fairly well. Since no direct relationship was found between flow rate and effective temperature, the relationship between the effective temperature and the above water temperature will be used to calculate the expected water output from the humidifier.

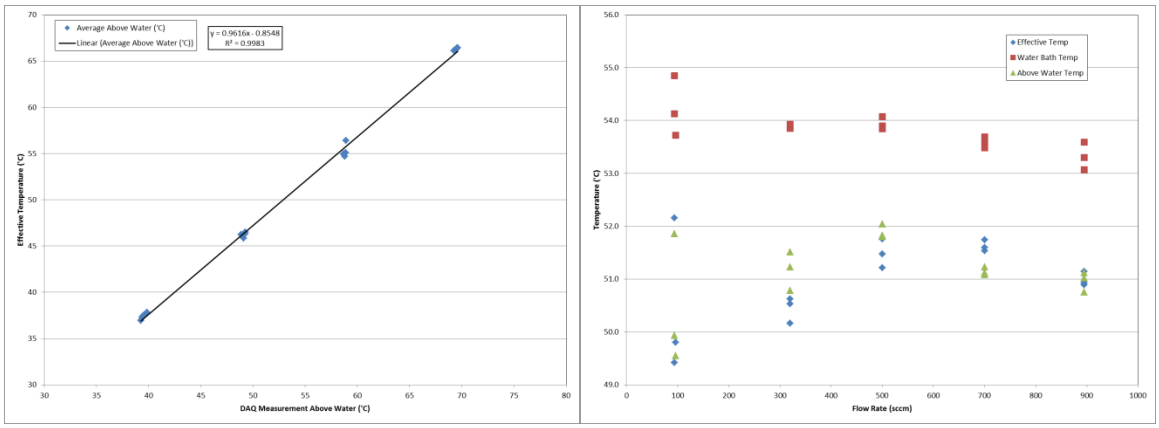

Figure 2.6: (a) (left) A linear relationship exists between the above water temperature and the effective humidifier temperature. This can be programmed into the data acquisition software to report this temperature to predict results. (b) (right) As the flow rate increases, the above water temperature changes while the water bath temperature remains fairly constant. The effective water temperature closely follows the above water temperature.

Leaks and Crossover

The volumetric flow rate is typically measured at the exhaust of the water flux assembly so one should consider that there are many connections which could leak throughout the setup. A leak in the system could change the flow rate and cause a loss of water. All the connections were leak tested using leak detector, Swagelok Snoop (Swagelok, Solon, OH). This fluid is put onto connections and will create bubbles if gas is leaving the connection. The system was pressurized and Snoop applied to all of the junctions. Any leaks were sealed. Sometimes a leak exists which is inside the water flux assembly. This can be checked by putting an impermeable membrane inside the assembly and running the experiment. If there are leaks from wet to dry side, then the

dry side desiccant will gain mass and crossover is occurring. This needs to be fixed until cross over is not present and the dry side desiccant does not gain mass. Crossover was not an issue with these experiments.

Uncertainty Analysis

There are several variables in this experiment which can greatly affect the water output of the humidifier and the water flux results. In order to identify the sensitivity of different measurements, uncertainty analysis was performed on the experimental and theoretical results.

Experimental Uncertainty

When considering the experimental measurement, the procedure is fairly simple. The change in mass of the desiccant is recorded over some change in time to arrive at a water mass flow rate.

$$\dot{m}_{H_2O} = \frac{\Delta m}{\Delta t} \quad [2.3]$$

$$U_{exp} = \sqrt{U_{stat}^2 + \left(\frac{U_{scale}}{t}\right)^2 + \left(U_t \frac{\Delta m}{t^2}\right)^2} \quad [2.4]$$

The experimental uncertainty, U_{exp}, is related to the statistical uncertainty, U_{stat}, the scale uncertainty, U_{scale}, and the stop watch uncertainty, U_t. The scale uncertainty is reported in the data sheet for the scale, and testing confirmed that the scale is accurate within 0.01 g. The stop watch uncertainty is fairly small and a conservative value of 5 seconds was used for this. This may seem large but the trials typically last an hour (3600 s) so the percentage error is small. The most difficult value to account for is the statistical uncertainty which is dependent on the data collected. Based on the sample size, standard deviation and desired confidence, an uncertainty can be calculated.

It is important to consider the sensitivity of each term. For some of the data taken during the calibration procedure, the time and scale uncertainty were extremely small. The statistical uncertainty was the most significant value and at least an order of magnitude greater than the

other terms. The sample sizes taken during calibration were typically small and this produces larger uncertainty bands because of the limited number of data points. When the membrane testing begins, a larger sample size will be taken to help decrease the uncertainty. With the low uncertainty of the scale and stop watch, the spread is not limited by the accuracy of the instruments. The user should be able to decrease the uncertainty simply by taking more data.

Theoretical Uncertainty

The derivation for the expected amount of water output from the humidifier, Eq. 2.2, is more complicated than the experimental equation. When the uncertainty analysis is performed on that equation, terms for the uncertainty for the water partial pressure, total pressure out of the humidifier, atmospheric temperature and volumetric flow rate can be isolated to investigate their effects on the water output.

$$U_{th} = \sqrt{\left(U_T \frac{\partial P_{H_2O}}{\partial T}\left(\frac{P_2}{(P_{H_2O}-P_2)^2}\frac{P_{atm}W_{H_2O}}{RT_{atm}}\dot{V}_{atm}\right)\right)^2 + \left(U_{P_2}\left(\frac{-P_{H_2O}}{(P_{H_2O}-P_2)^2}\frac{P_{atm}W_{H_2O}}{R\,T_{atm}}\dot{V}_{atm}\right)\right)^2 + \left(U_T\left(\frac{P_{H_2O}}{P_2-P_{H_2O}}\frac{P_{atm}W_{H_2O}}{R}\frac{\dot{V}_{atm}}{T_{atm}^2}\right)\right)^2 + \left(U_{V_{atm}}\left(\frac{P_{H_2O}}{P_2-P_{H_2O}}\frac{P_{atm}W_{H_2O}}{R\,T_{atm}}\right)\right)^2}$$

Water Partial Pressure + Total Pressure +Atmospheric Temperature + Volumetric Flow Rate

[2.5]

The uncertainty of the individual components can be found in data sheets. These include temperature uncertainty of 0.5 °C, pressure uncertainty of 0.25% of full scale (or 250 Pa), and a volumetric flow rate uncertainty of 0.8% of the reading + 0.2% of the full scale (>10 ccm). The water partial pressure uncertainty term takes into account how the water partial pressure changes with temperature. This is calculated based on tabulated values (Moran & Sharpiro, 2008).

The relative magnitudes in of these terms are interesting. For the flow rates considered, between 0 and 1000 ccm, the uncertainty from the total pressure and the atmospheric temperature are negligible to the calculation. The water partial pressure and volumetric flow rate uncertainties are much more interesting. At low nitrogen flow rates, the humidifier is outputting a small amount of water. Even though temperature is important, the flow rate reading is more sensitive and affects the calculation more heavily. The flow rate uncertainty starts at 10 ccm and then increases slowly as the flow rate increases. This is much more significant at 50 ccm than it is at 1000 ccm. At the higher flow rates, the percent error associated with the flow rate measurement decreases and the water partial pressure uncertainty becomes dominant. The relative contributions of each variable to the uncertainty can be seen in Figure 2.7. The water partial pressure is difficult to control because the uncertainty in the temperature measurement and the high gradient in the saturation pressure versus temperature curve. For the conditions shown in Figure 2.8, the gradient is about 870 Pa/°C. When considering the experimental humidifier output, the uncertainty analysis is able to bracket the data.

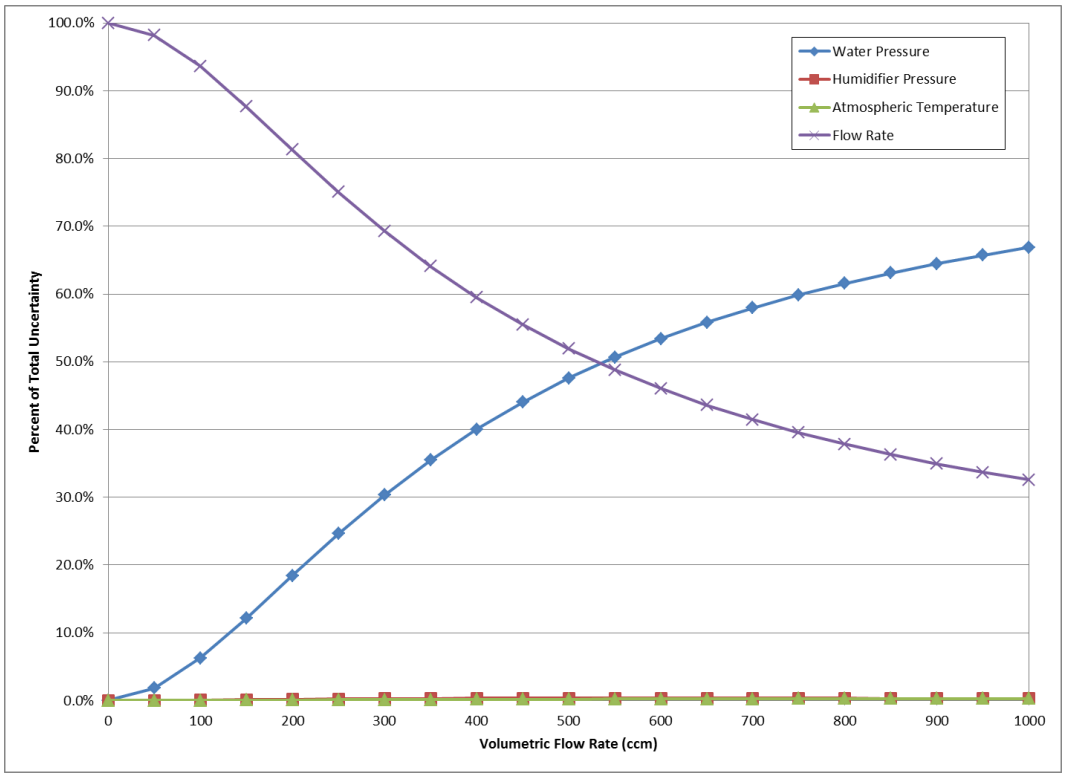

Figure 2.7: The contribution of each term in Eq. 2.5. At low flow rates the most error comes from the volumetric flow rate measurement. As the flow rate increases, the water partial pressure becomes more significant, surpassing flow rate uncertainty around 550 ccm.

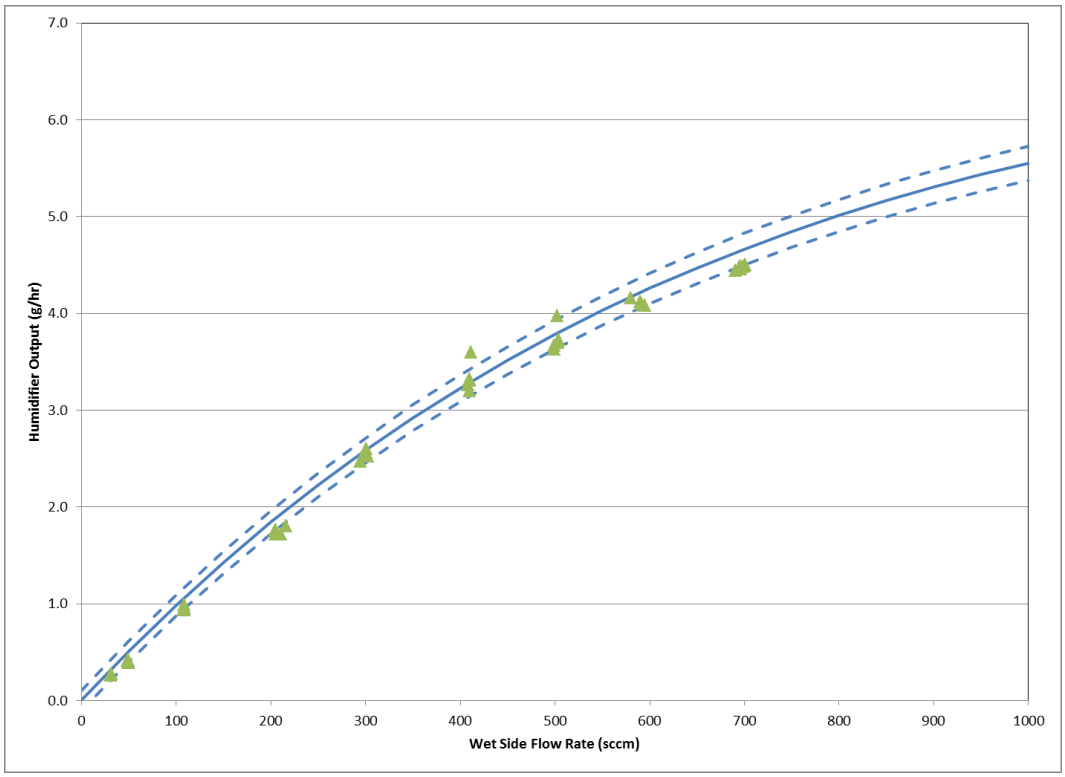

Figure 2.8: For 95% relative humidity at 60 °C, the experimental results are able to lie within the error bars. The solid blue line is the model prediction with the dashed lines representing the uncertainty bands. The symbols are experimental data points.

Experimental Procedure

Once the individual components are completely calibrated and there is confidence in the setup, the water flux testing can begin. In order to validate the overall experiment and the procedure, DuPont Nafion 117 PEM, was first used in the setup. This membrane has been well studied and water transport, water-membrane diffusion coefficients, and ionic conductivities can be easily found and used for validation of the experiment and modeling. Nafion 117 PEM is also mechanically and chemically stable at these operating conditions unlike some AEMs which can degrade, convert to a carbonate/bicarbonate ionic form, or fail.

For stability reasons, the AEMs are delivered in the chloride ion form. Since this ionic form is not useful in an operating fuel cell, the membrane must be converted to a hydroxide ion form. This can be done by performing an ion exchange and soaking the membrane in a potassium hydroxide (KOH) solution. The total number of chloride ions in the membrane, available for exchange, is known based on the ion exchange capacity (IEC) and the mass of the membrane. In order to exchange all of the ions, at least ten times more hydroxide ions were available in the solution than chloride ions were in the membrane. This was combined with the fact that the concentration of the KOH solution will directly affect the ionic conductivity and the degradation in the membrane. For the Excellion I-200 AEM, the membrane was seen stable in 10^{-4} M potassium hydroxide (Vega *et al.*, 2010). For this reason, this concentration was used for the ion exchange. Given the ion exchange capacity of the Excellion I-200 AEM was roughly 500 mmol eq/g, roughly 1 liter of 10^{-4} M KOH was sufficient to exchange all of the ions. The polysulfone AEMs were more stable in highly alkaline solutions and the collaborators used a stronger KOH solution of 1 M KOH. No degradation was seen using this high concentration. After 24 hours in the ion exchange solution, the membrane was then rinsed and soaked in 18 MΩ deionized water. This rinse and soak process was repeated every 24 hours until the pH of the

soaking solution maintained a pH of 7. During the soak in deionized water, nitrogen gas was bubbled through the water to prevent any contamination from carbon dioxide.

When the membranes are soaked in liquid water they are able to absorb the most water and swell to their largest volume. When in this fully hydrated state, the membranes are also the most flexible and can form the best seals in the membrane assembly. For these reasons, the membrane was first soaked in liquid water for at least 24 hours to fully saturate the membrane. A section of membrane the size of the entire flow plate, 10 cm x 10 cm, was cut and put between two graphite flow plates. It is important to consider that only a membrane is used. Other fuel cell components such as a catalyst or gas diffusion layer are absent here. This is done to isolate the effect of water transport in the membrane. If the other layers are included, they might impose another resistance for the water transport which would need to be considered. The flow channels were aligned such that they ran parallel to one another. This creates a high concentration gradient at the entrance to the cell which will decrease as water is transported across the membrane. This can be modeled using a marching scheme which will be discussed later. To complete the assembly, copper current collectors were put behind the flow channels and then stainless steel back plates. A pattern of eight 1/4-28 bolts were threaded through the stainless back plates to compress the assembly and the membrane. The bolts were lubricated using DuPont Krytox (DuPont, Wilmington, DE) and tightened in a crisscross applesauce pattern similar to tightening a car tire. The torque applied to each bolt was increased in increments of 1.13 N-m (10 in-lb) until 5.65 N-m (50 in-lb) was reached. This specification was found to be satisfactory for preventing any gas from escaping the flow channels.

The water flux assembly was then installed in the experimental setup. The membrane is currently in a fully hydrated state and needs to release some water to achieve equilibrium with its

environment. Since each trial in this experiment will take roughly one hour, the membrane needs to reach steady state to collect the most accurate data and eliminate transient effects. A predetermined set of experimental parameters is known and the experiment is set to run at those conditions. As a starting point, this typically involved running at roughly 300 ccm and 95% relative humidity on the humid side, and dry nitrogen on the dry side. The tests ran at membrane temperatures of 40, 50 and 60 °C. The experimental setup typically took 2 hours to reach steady state conditions (temperatures and pressures). After being installed in the water flux assembly, the membrane was given at least 16 hours to release any extra water and reach steady state with the system. If the membrane was not at steady state and was still releasing water than it would be apparent in the measurements and seen as a decreasing water flux value. This was not witnessed and therefore this amount of time was considered satisfactory.

Once the membrane had reached equilibrium, the experiment is ready to commence. The starting masses for the two desiccant tubes was measured and recorded. The desiccants were hooked up to the exit of the water flux assembly and the data acquisition software was started. The software will monitor the pressures and temperatures throughout the system and record the data every minute. This is important for considering the amount of water which should be output from the humidifier. At the beginning of the test, the flow rate is measured coming out of the desiccant tubes. The Alicat is installed at the exit of the desiccant so that only the nitrogen flow rate is measured and the gas has reached ambient temperatures and pressures. The flow rate remains fairly constant once the system has been given 16 hours to reach steady state so multiple measurements during a trial are not required. The flow rate is measured once during each trial to ensure the flow rate has not changed.

The length of each trial is dependent on the amount of water transporting the membrane. If most of the water is staying on the humid side of the membrane, then the water flux measurement will have a high uncertainty because of the scale resolution. Typically, the trials ran for 1 hour which was enough time to see at least a 0.20 g change in mass for the dry desiccant. After the trial was completed, the two desiccants were disconnected and their masses were recorded. The temperature and pressure data was also processed so that average temperatures could be considered. The data was exported from the Agilent software to Excel where a macro averaged the data. From there, the average temperature and pressure values could be used to compare a theoretical water output from the humidifier to the experimental value. This process was repeated for at least 5 data points at a given flow rate before moving to another flow rate. Data was taken between 50 and 700 sccm for the membranes. At least two temperatures were tested for each membrane so that properties could be measured as a function of temperature as well as hydration.

Numerics

Water Flux Numeric Model (MP09)

The water flux experiment detailed above can measure an average water flux across the membrane. The experiment is limited by only capturing the exhaust gas at the exit of the serpentine flow channels to arrive at the average water flux. In order to determine local hydration values along the flow channel, the experimental parameters can be fed into a numeric model. Developing and debugging this model was accomplished by the hard work of Timothy D. Myles and Dr. Aldo A. Peracchio (Myles *et al.*, 2011). A brief description of their work will be explained in the following paragraphs given its relevance to the water flux experiment and the predicted ion-membrane diffusion coefficients which use the results of this model.

Using the experimental approach, only an average water flux can be calculated. With the initial conditions entering the assembly, there is a broad range of local hydration values in the membrane as the gas travels the length of the channel. Several membrane properties such as diffusion coefficients and ionic conductivity are heavily dependent on the local hydration, so having a description of the local hydration is important for the quality of the data. The basic approach for the numeric model is to use a marching scheme with known initial conditions. The water flux assembly can be segmented into many control volumes and a mass balance can solve for the amount of water transported across the membrane, and the gas concentrations in that volume. These values can be applied as inlet conditions for the next control volume until the end of the flow channel is reached. Knowing the exit water concentrations in the gas streams allows for an average water flux to be calculated and compared to the experimental results.

Within this model, there are several assumptions that require explanation. One of the key assumptions is that the AEMs and PEMs have similar water transport behavior. Both types of

membranes are composed of fixed ionic groups attached to a polymer backbone. With a hydrophobic backbone and hydrophilic ionic groups, the membranes should demonstrate the same processes when exposed to water. These membranes also maintain similar water uptake behavior and exhibit percolation limits at low hydrations. For these reasons, it will be assumed in this work that both types of membranes transport water using similar mechanisms.

Once water is absorbed into the membrane, it is assumed that diffusion is the limiting transport mechanism. Some works have shown significant interfacial mass transport effects however during the validation stage, the model was able to agree with other techniques which would not observe interfacial mass transport effects. This would suggest that interfacial mass transport in negligible and one explanation to its existence in these experiments is device error which can be accounted for (Caulk *et al.*, 2012). The model also assumes that the flow channel can be simplified to a one-dimensional straight flow channel. While the actual flow channels are tortuous and have several bends, majority of the path is made of straight lengths. The gas flow through the channels is computed considering friction losses in the flow channels. These calculations can take into account the bends in the channel, creating a larger effective length, and the back pressure calculated using these calculations agrees with the experimental values. The system can also be simplified to assume that the diffusion is one-dimensional through the membrane. This would imply that water diffusion in the membrane is through the thickness of the membrane and is negligible in other directions. Since the flow channel is a serpentine path, it is possible that water could diffuse in other directions inside the membrane and not only through the thickness. When considering the small thickness of the membrane, a much more significant concentration gradient can exist in this direction than any other and this assumption should be valid.

Water absorption isotherms were used to determine the local hydration at the boundaries of the membrane in each control volume. These curves were found in the literature and not performed in this work. Isotherms for Nafion 117 PEM (Zawodzinski *et al.*, 1991) as well as ETFE and FEP AEMs (Varcoe, 2007) were found in the literature. The water uptake isotherms have a limited number of data points and modeling efforts can be used to determine continuous relationship between water vapor activity and local hydration in the membrane. It is common in the literature to fit the water uptake using a cubic polynomial fit or an adsorption model originally proposed by Brunauer, Emmett, and Teller (BET) (Brunauer *et al.*, 1938). Using the BET model provides an analytical equation with physical insight to water absorption by considering three parameters which are known, or fit, to solve for multiple adsorption layers of the gas. It can be difficult to calculate the slope of the water uptake isotherm using the BET model so some groups have used cubic polynomial equations to represent water uptake isotherms (Ge *et al.*, 2005, Motupally *et al.*, 2000). Using this polynomial expression, the slope of the isotherm can be more easily calculated. It should be noted that the fit for the water uptake isotherm and its derivative are extremely sensitive to the modeling technique used and the criteria for calculating the isotherm.

In order to solve for the flux through the membrane in each of these control volumes, a diffusion coefficient needs to be prescribed. This diffusion coefficient should be dependent on the temperature and the local hydration of the membrane. Values for the diffusion coefficient of water in Nafion 117 are abundant and span orders of magnitude in the literature (Hallinan & Elabd, 2009, Motupally *et al.*, 2000) but water-membrane diffusion coefficients for AEMs are not well studied. In order to determine a water-membrane diffusion coefficient, a second-order polynomial expression was assumed to represent the diffusion coefficient. This polynomial

expression is a function of activity and is fixed such that the diffusion coefficient approaches zero when there is no water present.

The diffusion coefficient is multiplied by the Darken factor to arrive at an effective water-membrane diffusion coefficient. The Darken factor is a correction for non-uniform activity coefficients and relates the hydration in the membrane to the relative humidity conditions outside the membrane. The Darken factor can be calculated from the water uptake isotherm for the membrane and is responsible for a characteristic maximum in the water-membrane diffusion coefficient. The membrane is composed of a hydrophobic polymer backbone and hydrophilic fixed ion groups. One model proposed by Hsu and Gierke (Hsu & Gierke, 1982) suggests that water is absorbed into the membrane quickly in order to solvate the hydrophilic fixed ion groups (Weber & Newman, 2003). Any absorbed water can transport through the membrane quickly with the additional driving force to hydrate the fixed ionic groups. This can be seen as the rapid increase in the water-membrane diffusion coefficient at low hydrations. As more water is absorbed, the membrane rearranges itself to form clusters where the fixed ion groups surround a core of water. Between the clusters, channels can exist to transport water and ions. With the hydrated fixed ionic groups, the water-membrane diffusion coefficient decreases since water will need to transport within small channels between the clusters without the addition driving force for solvating the fixed ionic groups. As the membrane is further hydrated, the number of channels in the membrane and channel size can increase, causing transport between clusters, and through the membrane, to increase. When the membrane is submerged in liquid water, it will hold the most water and channels will be largest to allow for the fastest transport of species. The location and magnitude of this peak are strongly dependent on the water uptake curve chosen. It can be difficult to experimentally measure water uptake at low relative humidities and

hydrations. This region is extremely important for the Darken factor since the peak is located at low hydrations ($\lambda = 2 - 3$). After choosing a water uptake model based on reported values in the literature, the Darken factor can be calculated. This leaves two unknown values in the diffusion coefficient expression, α and β.

$$D_{H_2O,M}^{eff} = D_{H_2O,M}\left[\frac{\partial \ln a}{\partial \ln \lambda}\right]_{Darken} \quad [3]$$

$$D_{H_2O,M}^{eff} = (\alpha a^2 + \beta a)\left[\frac{\partial \ln a}{\partial \ln \lambda}\right]_{Darken} \quad [4]$$

Using this expression, a diffusion coefficient can be fit to minimize the error between the numerical average water flux and the experimental water flux. The α and β combination which has the minimum error, can be used to represent the water-membrane diffusion coefficient as a function of local hydration.

Ionic Conductivity Model

With the water-membrane diffusion coefficient determined by the MP09, a method is needed to relate the water-membrane diffusion coefficient to the ionic conductivity in the membrane. This can be accomplished using the dusty fluid model (DFM) and Ohm's law. Starting with the generalized Stefan-Maxwell diffusion equations, the DFM can be derived where, the membrane is treated as a separate species that interacts with the diffusing media but is fixed in space (Grew & Chiu, 2010, Mason & Malinauskas, 1983, Thampan *et al.*, 2000). The membrane, or "dust," particles are uniformly distributed and can represent the side chain groups of the membrane. Using the DFM, the flux of each species can be solved for. Assuming the side chains are uniformly distributed, a concentration gradient of mobile ions cannot exist according to the condition of electroneutrality. In this analysis, the interaction between the mobile ion species is assumed negligible. The total ionic conductivity of the membrane is then calculated as the summation of the individual conductivities in the system. The individual conductivities can then be calculated considering only two mobile species: water and the conducting ion (hydroxide, carbonate, or bicarbonate). Considering a closed electrochemical impedance spectroscopy cell, then it can be assumed that the two species have equal and opposite molar fluxes and are in pseudo-equilibrium (Grew & Chiu, 2010, Thampan *et al.*, 2000). Manipulating the DFM and Ohm's law with these assumptions allows for the ionic conductivity to be solved in the membrane as seen in Eq. 1. Considering comparable assumptions, a similar equation can be derived starting with the Nernst-Planck equation.

$$\sigma = \sum \sigma_i = \sum \frac{F^2 z_i^2}{RT} \frac{(\varepsilon - \varepsilon_0)^q D_{i,H_2O}^0}{1 + \delta_i} C_i \alpha_i \qquad [2.5]$$

Using Eq. 2.5, the ionic conductivity of the membrane can now be calculated based on several important variables. The first term is a constant which is comprised of Faraday's

constant, F, valence of the ion, z_i, the universal gas constant, R, and the temperature of the system, T. The diffusion coefficient in the pore is estimated by multiplying the infinite dilution diffusion coefficient in water, D_i^0, by a Bruggemann term which is a function of pore volume fraction, $(\varepsilon - \varepsilon_0)^q$. This term takes into account a peroration threshold, ε_0, where below this value, there are no contiguous pathways through the membrane and the conductivity is zero. This expression is raised to the Bruggemann exponent, q, which can be treated as a fitting parameter. It is common in the literature to use a value of $q=1.5$ for both PEMs and AEMs (Grew & Chiu, 2010, Thampan *et al.*, 2000).

The denominator of that term contains a parameter, δ_i, which is the ratio of the diffusion coefficient of the ion, i, in water, D_{i,H_2O}^{eff}, to the effective ion-membrane diffusion coefficient, $D_{i,M}^{eff}$.

$$\delta_i \equiv \frac{D_{i,H_2O}^{eff}}{D_{i,M}^{eff}} \qquad [2.6]$$

It is difficult to measure this ratio since both diffusion coefficients are dependent on the local hydration of the membrane. Attempts have been made to simplify this expression by treating it as a constant fitting parameter (Thampan *et al.*, 2000) or using kinetic theory to approximate its value (Choi *et al.*, 2005). Using the MP09 model, an effective water-membrane diffusion coefficient is predicted and can be used to find ion-membrane diffusion coefficients. This approach will then directly solve for the parameter δ_i instead of treating it as a fitting parameter.

The final variables represent the concentration of ions in the pore of the membrane. The total concentration of ion i in the membrane is multiplied by a dissociation constant, α_i, to yield the number of ions available for transport in the pore, C_i. Equilibrium constants are used in Eq. 2.7 to solve for concentrations of free ions, C_i, free fixed ions from the membrane, C_M, and the

number of ions attached to membrane, $C_{i\cdot M}$. The dissociation constant for a species *i* is defined as the fraction of free (dissociated) ions available in the pore compared to the total number of that species in the membrane.

$$K_i = \frac{[C_i][C_M]}{[C_{i\cdot M}]} \quad [2.7]$$

Ion-Membrane Diffusion Coefficients

Using the experimental and numerical tools outlined above, an effective water-membrane diffusion coefficient is found. This diffusion coefficient needs to be corrected to be in an ion-membrane form to be useful in the ionic conductivity equation. In order to accomplish this, principles from kinetic theory are utilized which can convert from the water-membrane diffusion coefficient to an ion-membrane diffusion coefficient.

Kinetic theory, which was originally developed for low density monatomic gases where transport properties can be predicted based on collisions for non-interacting rigid spheres, is able to predict diffusion coefficients for most gas mixtures within a reasonable uncertainty (Bird *et al.*, 2007). This is enabled by the relatively small interaction between molecules and serves as an approximation in this work. More rigorous derivations of the theory include interactions between molecules and more accurately predict transport properties for non-ideal gases and liquids (Bird *et al.*, 2007). For these conditions, the specific details of the nature of forces between both individual and groups of neighboring molecules are more significant and should be considered for the most accurate prediction. For a system in the membrane, the forces between molecules can be significant given that it is in liquid phase and contains ions. In order to minimize charge effects and inter-molecular forces, a primary solvation shell is considered around the ion. Considering this solvation shell, a hydrated ion can be assumed to transport through the membrane with similar inter-molecular forces to a single water molecule. These forces are captured in the water-membrane diffusion coefficient which was measured experimentally. Therefore, the water-membrane diffusion coefficient which was measured can be scaled using predictions from kinetic theory to arrive at a diffusion coefficient of the ion in the membrane.

Kinetic theory states that a diffusion coefficient between two species is going to be related to the speed of the particles and the mean free path (Bird *et al.*, 2007). The average speed of the particles can be found based on a reduced mass of the two diffusing species, μ_{ij}. If the particles are assumed to be rigid spheres, the average distance traveled between each collision for the particles is found using the collision radii of the particles, r_{ij}, as well as the total number density of the system, N_{ij}. Knowing these properties, the diffusion coefficient between two species, *i* and *j*, can be found using Eq. 2.8.

$$D_{ij} = \frac{2}{3}\sqrt{\frac{k_B T}{\pi \mu_{ij}}}\frac{1}{\pi r_{ij}^2}\frac{1}{N_{ij}} \quad [2.8]$$

The diffusion coefficient of water in the membrane is found experimentally. Starting with an identity relationship (Eq. 2.9), the terms can be rearranged to solve for an ion-membrane diffusion coefficient by scaling the water-membrane diffusion coefficient (Eq. 2.10).

$$\frac{D_{i,M}}{D_{i,M}} = \frac{D_{H_2O,M}}{D_{H_2O,M}} \quad [2.9]$$

$$D_{i,M} = D_{H_2O,M}\left[\frac{D_{i,M}}{D_{H_2O,M}}\right] \quad [2.10]$$

Equation 2.8 can now be substituted into Eq. 2.10 to arrive at an expression for an ion-membrane diffusion coefficient as seen in Eq. 2.11.

$$D_{i,M} = D_{H_2O,M}\left[\sqrt{\frac{\mu_{H_2O,M}}{\mu_{i,M}}}\frac{r_{H_2O,M}}{r_{i,M}}\frac{N_{H_2O,M}}{N_{i,M}}\right] \quad [2.11]$$

The diffusion coefficient which is calculated here is strictly a collision based diffusion coefficient and would not include other mechanisms for ion transport such as structural diffusion. This equation only depends on the water-membrane diffusion coefficient, reduced masses,

collision radii and number densities of the diffusing species. These properties can all be calculated based on values found in Table 1.1 and reported in the literature.

Table 1.1: Mobile species properties.

Species	Hydration Number	Molar Mass [g/mol]	Hydrated Radius [Å]	References
H_2O	-	18.02	1.46	(Bockris & Reddy, 1970)
OH^-	4.0	89.07	3.00	(Marx, 2006, Nightingale Jr., 1959)
HCO_3^-	6.9	185.32	3.64	(Leung *et al.*, 2007)
CO_3^{-2}	8.7	216.74	3.94	(Kameda *et al.*, 2006, Leung *et al.*, 2007, Nightingale Jr., 1959)

Results and Discussion

The methodology for calculating the diffusion coefficient from the water flux experiment was validated by using the Nafion 117 PEM. This membrane was chosen for validation because of the volume of data and literature published on water uptake, water-membrane diffusion coefficients, and ionic conductivities. The water flux results from the experiment agreed with data from the published literature given the operating conditions. This validated both the experiment as well as the numerical water flux model.

The experiment was run using two different membranes: DuPont Nafion 117 PEM was used for validation and SnowPure Excellion I-200 AEM was the membrane of interest. Water absorption isotherms were taken from the literature from Zawodzinski *et al.* for Nafion 117 PEM and from Varcoe for an ETFE AEM (Varcoe, 2007, Zawodzinski *et al.*, 1991). Both of these membranes were exposed to temperatures of 50 and 60 °C and incoming relative humidities of 95% on the humid side and 0% on the dry side. The two membranes have reported thicknesses of 178 μm for Nafion 117 PEM and 350 μm for Excellion I-200 AEM. When looking at the experimental data, several trends can be observed. The 60 °C water flux values are consistently higher than the 50 °C data. Since the relative humidity is a function of the operating temperature and the incoming relative humidities are fixed, the mass flow rate of water entering the assembly is higher at the elevated temperature. With more water being output from the humidifier, there is more water available to diffuse across the membrane and a higher average water flux is possible. Also, given the same operating conditions, Nafion 117 PEM has a much higher water flux than the Excellion I-200 AEM membrane. This agrees with predictions based on the thicknesses of the two membranes, Nafion 117 PEM having a thickness which is roughly half of Excellion I-200 AEM.

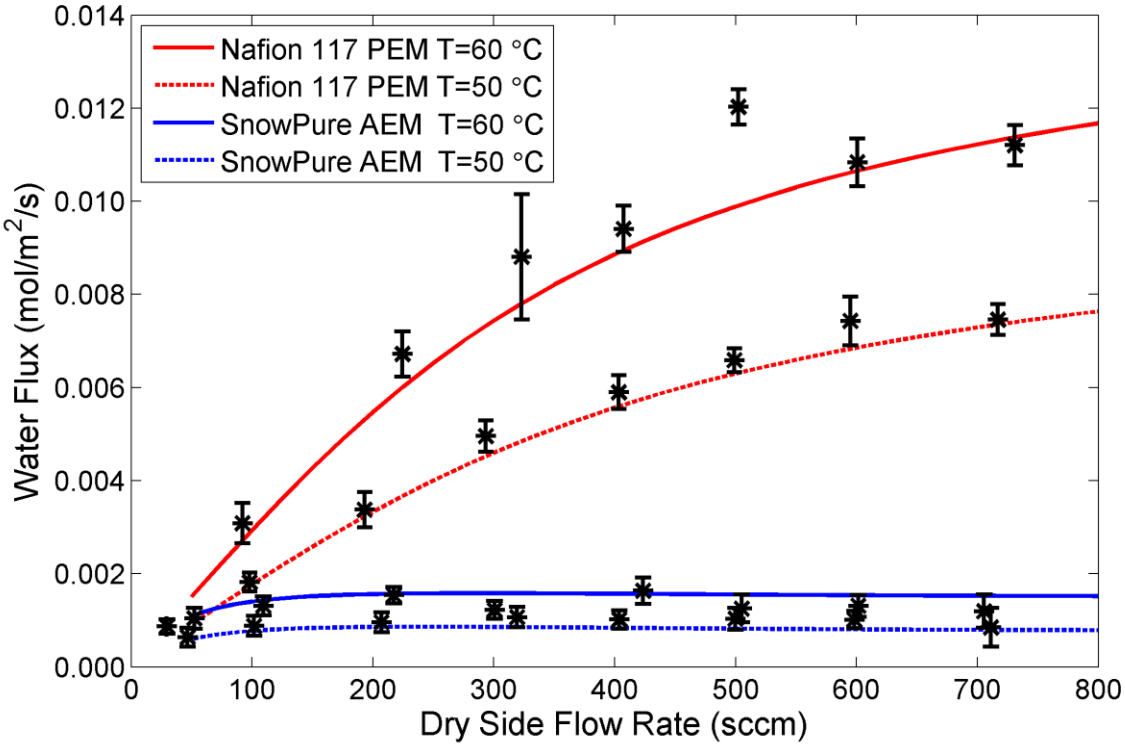

Figure 2.9: The symbols represent experimental data points with their associated uncertainties. The red and blue lines show the predicted water flux using the MP09 model for Nafion 117 PEM and SnowPure Excellion I-200 AEM respectively (Kiss *et al.*, 2013b).

The MP09 model can successfully predict the average water flux through the membrane which means that the diffusion coefficient used accurately represents transport in the membrane. The water flux results for Nafion 117 PEM can be used to validate the predicted water-membrane diffusion coefficient. The water-membrane diffusion coefficient for Nafion 117 PEM has been reported in the literature and can be used for validation of the MP09 predicted diffusion coefficient. Although the spread of values is large in the literature, the diffusion coefficient reported by Zawodzinski *et al.* using an NMR technique agrees extremely well with the MP09

value as seen in Figure 2.10 (Myles *et al.*, 2011, Zawodzinski *et al.*, 1991). This technique does not subject the membrane to interface effects. This suggests that the interface effects are negligible in this water flux experiment and diffusion is the dominant resistance.

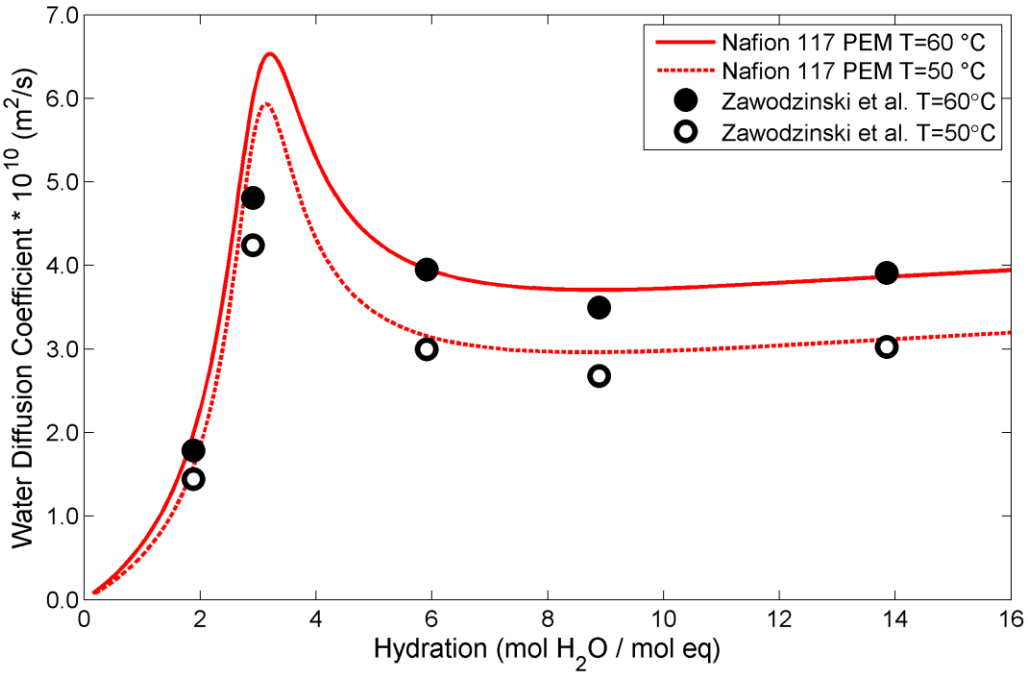

Figure 2.10: Validation of the MP09 for extracting diffusion coefficients using Nafion 117 PEM (Myles *et al.*, 2011).

With the water flux experiment and model validated using Nafion 117 PEM, a water-membrane diffusion coefficient could be found for Excellion I-200 AEM. This diffusion coefficient includes effects from the structure of the membrane, such as the tortuosity, as well as sorption effects (Majsztrik *et al.*, 2007, Motupally *et al.*, 2000, Myles *et al.*, 2011, Satterfield & Benziger, 2008). Currently the model does not distinctly account for any sorption effects and is able to agree with reported diffusion coefficients for Nafion 117 PEM. In an AEM system, the

water flux through the membrane is significantly lower and therefore any sorption effects should be less significant than in a PEM system. The water-membrane diffusion coefficient for the Excellion I-200 AEM is about an order of magnitude less than that of Nafion 117 PEM. This is in agreement with the water flux measurements that show significantly less water diffusing through the AEM than the PEM.

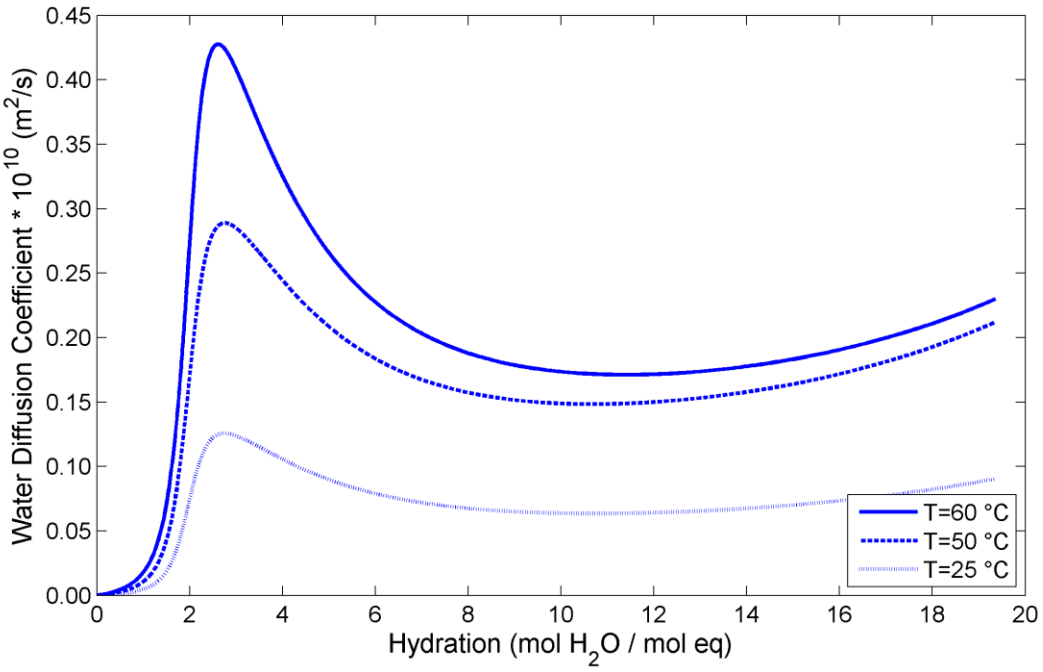

Figure 2.11: The reported effective water-membrane diffusion coefficient for Excellion I-200 (Myles *et al.*, 2011).

To convert the water-membrane diffusion coefficient to an ionic form such as the hydroxide form, Eq. 2.11 can be used. Given that the species is transporting in the presence of water, hydrated values are used such that the primary solvation shell is considered. This accounts for several water molecules solvating the ion, increasing the mass and radius. The number of

water molecules present in the solvation shell depends on the ion and ranges from 4 around hydroxide (Marx, 2006), to 6.9 around bicarbonate (Leung *et al.*, 2007), and 8.7 to 9.1 around carbonate (Kameda *et al.*, 2006, Leung *et al.*, 2007). Hydrated radius values were used based on Nightingale (Nightingale Jr., 1959) whom correlated the Stokes radius to the hydrated ionic radius. The mass of the ions is simply a combination of the ion mass and the mass of the water molecules in the solvation shell. The hydroxide ion has the smallest hydrated radius and mass while the carbonate ion has the largest radius and mass. The number density of the carbonate species present in the membrane will be different than that of the bicarbonate and hydroxide ions. This is because of the -2 valence of the carbonate ion versus the -1 valence of the other species.

When using the conductivity equation shown above in Eq. 2.5, there is an assumption that the activity coefficients in the system are unity. In the water-membrane diffusion coefficient, the Darken factor is used to correct for non-unity activity coefficients. Therefore, this component should not be considered when using the conductivity equation and only the Stefan-Maxwell diffusion coefficient should be considered. The quaternary ammonium fixed ionic groups are uniformly distributed in space and the ionic conductivity is solved for a fixed hydration state of the membrane. The activity coefficient of the ions will remain constant and should not have a significant effect on the solution.

The Stefan-Maxwell diffusion coefficients for the SnowPure AEM are plotted in Figure 2.12 and all increase with increasing hydration in the membrane. The curves, especially for H_2O, show a percolation limit at low hydrations where transport rates become inappreciable. The water-membrane diffusion coefficient has the lowest of the diffusion coefficients, when compared with the ion diffusion coefficient at higher hydrations, where the membrane would

most likely be operated. With the pore volume fraction increasing with hydration, the ion-membrane diffusion coefficients increase as the species become diluted in the pore volume. The hydroxide ion has the highest diffusion coefficient in the membrane due to its relatively small size and mass. Hydroxide can also transport through a Grotthuss mechanism in water while carbonate and bicarbonate ions cannot. The carbonate diffusion coefficient is the next largest despite having a larger mass and collision radius than the bicarbonate ion. This happens because the number density of the carbonate species is lower in order to maintain electroneutrality.

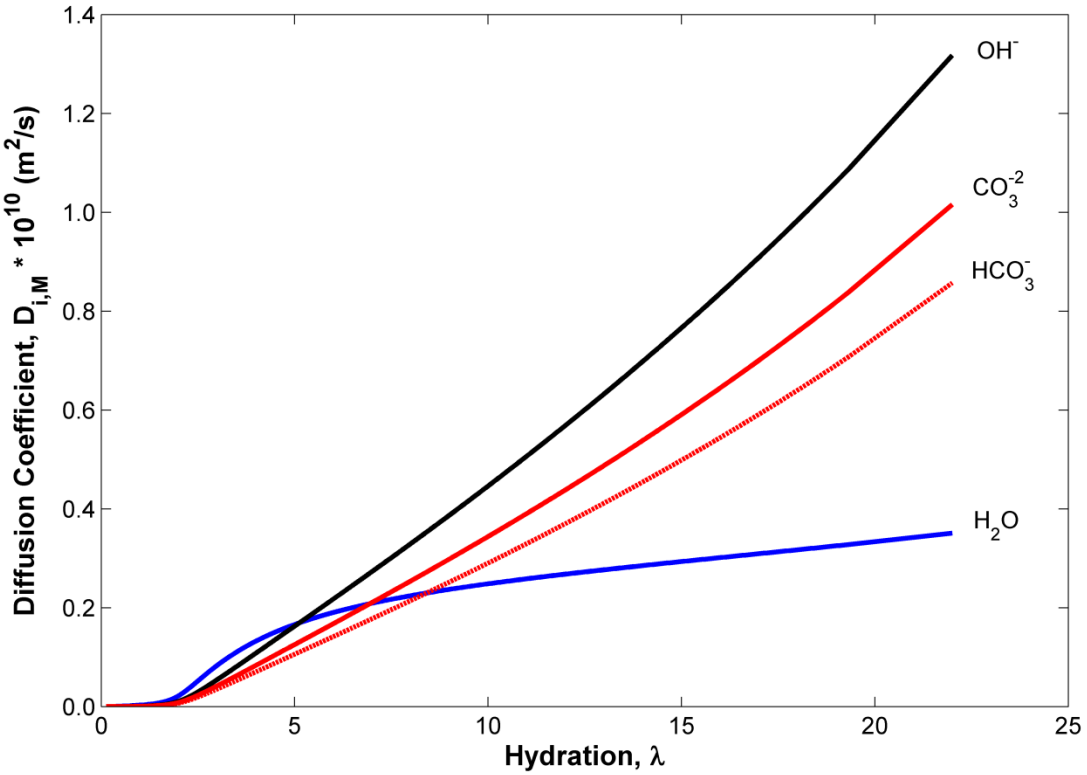

Figure 2.12: The diffusion coefficients as functions of hydration in Excellion I-200 AEM (Kiss *et al.*, 2013b).

With the diffusion coefficients that were calculated for different ionic species, the ionic conductivity of the membrane can be calculated as a function of hydration. Using Eq. 2.5, the diffusion coefficients for the different species are substituted into the equation to yield the ionic conductivity. Results are shown in Fig. 2.13a for three membranes: Nafion 117 PEM, ETFE AEM, and SnowPure AEM. Experimental results provided for Nafion 117 PEM (Sone *et al.*, 1996, Zawodzinski *et al.*, 1991), ETFE AEM (Varcoe, 2007), and Excellion I-200 AEM (Vega *et al.*, 2010) to validate the numerical predictions from the model. In order to best match the experimental value, the equilibrium constant used in Eq. 2 for the side groups and hydroxide is fitted within values reported values in the literature (Helfferich, 1962, Mbuna *et al.*, 2004). The trimethylammonium (TMA) hydroxide group is a strong base and the corresponding equilibrium constant (i.e., base constant) which was found is $K_{TMA \cdot OH}$ = 0.37. Even with this equilibrium constant value, only a fraction of the hydroxide ions that are available for transport in the membrane are free and dissociated from the membrane. At fully hydrated conditions, roughly 32% of the hydroxide ions (counter-ions) are dissociated from the side chain groups. To determine the dissociation, the fraction of free ions can be found using the concentrations of species calculated using Eq. 2.7. The dissociation is calculated by dividing the free concentration of hydroxide by the total concentration of hydroxide in the membrane. This approach was used by Thampan *et al.* (Thampan *et al.*, 2000) for calculating the dissociation of protons in Nafion PEM. As the dissociation increases, more ions will be available for transport and the ionic conductivity will increase.

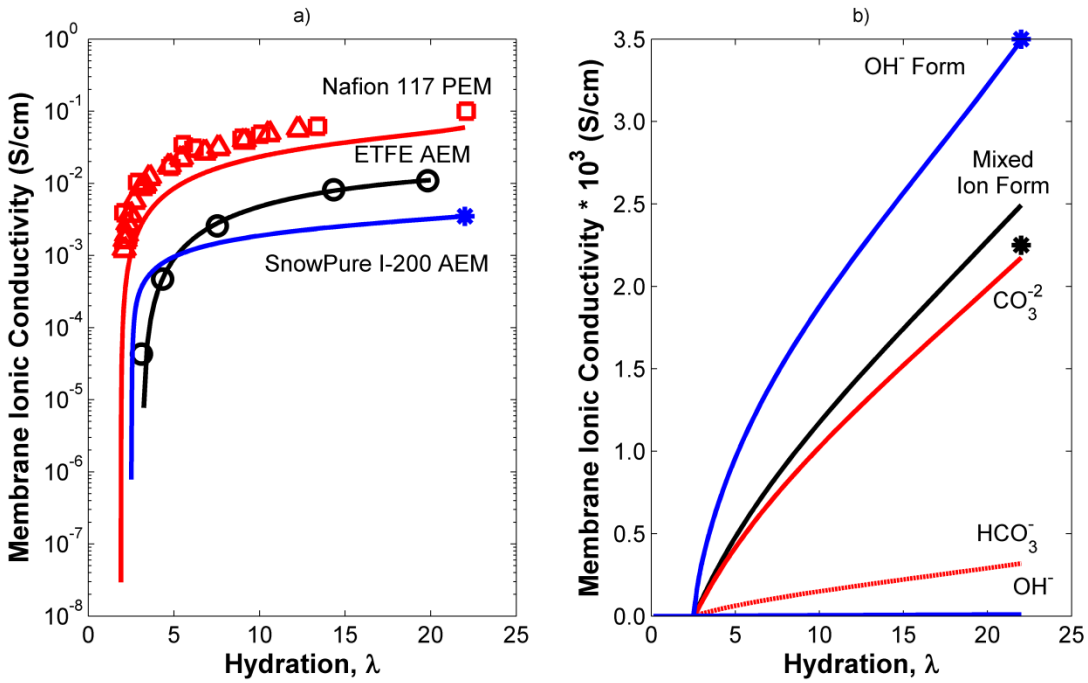

Figure 2.13: a) Using the approach described, the model is successfully able to predict the ionic conductivity of different fuel cell membranes as a function of hydration. b) This tool can then be used to predict the ionic conductivity of the membrane in different ionic forms. All of the symbols are experimental points while the lines are numerical predictions (Kiss *et al.*, 2013b).

With the approach outlined above, the water-membrane diffusion coefficient was experimentally measured for Nafion 117 PEM and SnowPure Excellion I-200 AEM. Knowing the water-membrane diffusion coefficient allows for the direct calculation of the δ parameter in Eq. 2.6. Unfortunately, an ETFE membrane was unavailable for testing and is discussed here as a comparison for the SnowPure Excellion I-200 AEM to another AEM. Previous studies for PEMs and AEMs have used δ as a fitting parameter because a water-membrane diffusion coefficient

was unknown (Grew & Chiu, 2010, Thampan *et al.*, 2000). In these works, δ was treated as a constant and was able to achieve reasonable agreement to experimental conductivity results. A least squares fit algorithm can be applied to experimental hydroxide conductivity results for ETFE AEM to arrive at values for δ and a percolation limit. A value of 1.65 can be found for δ and a percolation limit at $\lambda = 3.16$ was found for the AEM. These values are reasonable when compared to reported values by Grew and Chiu with $\delta = 1.90$ and a percolation limit at $\lambda = 2.50$ for the ETFE AEM (Grew & Chiu, 2010). It is difficult to compare the ionic conductivities of the ETFE AEM and SnowPure AEM since they have several differences including backbone polymer and ion exchange capacity. It can be noted that the ETFE AEM has a hydroxide ionic conductivity that is noticeably greater than the SnowPure AEM. However it is still roughly an order of magnitude less than the proton conductivity of the Nafion 117 PEM.

A further decrease in ionic conductivity was seen when the ion exchange put the membrane in a carbonate and bicarbonate form. For the carbonate and bicarbonate results, Vega *et al.* treated the membrane in a solution of 0.5 M Na_2CO_3 and 0.5 M $NaHCO_3$. Knowing this treatment, the ion concentrations in the external solution can be solved and used to predict ion concentrations in the membrane (Helfferich, 1962). This was done assuming an ideal membrane which has no preference to specific counter-ions. Taking into account the ion concentration in the external solution and the valence of each ion, the membrane was found to be primarily in a carbonate ion form. Even though the membrane was assumed to have no preference to counter-ion, the -2 valence of the carbonate ion makes it more preferable for the membrane (Helfferich, 1962). The mole fraction of the ions in the membrane was 60.75%, 38.62%, and 0.64% for carbonate, bicarbonate, and hydroxide respectively.

Knowing the ion concentrations in the membrane, the total ionic conductivity is assumed to be the addition of the ionic conductivity from each ion. With only a single experimental data point at fully hydrated conditions, it is difficult to separate the individual effects from the two mobile ions present in the membrane. In order to predict the dissociation of individual ions in the membrane, ions of the same valence are assumed to have equal equilibrium constants. Using this approach, the bicarbonate and hydroxide will use the same equilibrium constant and the carbonate equilibrium constant can be obtained using values from ions of the same valence in the literature (Mbuna *et al.*, 2004). Using this approach, a value of $K_{TMA \cdot CO_3}$ = 0.08 M can be used for carbonate. This equilibrium constant is much lower than that of hydroxide in the membrane which means a smaller dissociation constant for carbonate ions. The individual contributions to the ionic conductivity are shown in Figure 2.13b. Carbonate contributes most given it has the highest concentration in the membrane and carries more change with a -2 valence.

With the membrane being put in the carbonate/bicarbonate form, a decrease in performance is seen by both the model and the experimental results. This decrease in ionic conductivity agrees with the trend for the values calculated for the ion-membrane diffusion coefficients. If the ion has a lower diffusion coefficient, then it would be expected that the ionic conductivity would be lower for that ion as well. This model is able to successfully predict the performance for the membrane in the hydroxide form and match the experimental results. However, with the mixed ion form, the model over predicts the conductivity of the membrane. The model predicts total ionic conductivity of the membrane in the carbonate form to be 2.49 mS/cm where the experimental results show 2.25 mS/cm. This exceeds the experimental value by roughly 10%. This increase can be from several factors including over predicting ion-membrane diffusion coefficients or neglecting effects between the counter-ions.

Using this model, the dissociation effects in the membrane can also be investigated. With Nafion PEM, there is almost complete dissociation between the fixed sulfonic acid groups and the protons (Thampan *et al.*, 2000). This helps contribute to the high ionic conductivity of Nafion PEM. Even with highly basic head groups, the ion dissociation in AEMs is much lower than in their acidic counterparts (Grew *et al.*, 2010). For the SnowPure AEM with hydroxide counter-ions at fully hydrated conditions, only 32% of the ions are free for transport in the pores. When the membrane is exchanged into the mixed carbonate/bicarbonate form, three ions are present and the total dissociation can be looked at for each ion as well as the total free charge in the pores. The hydroxide and bicarbonate are roughly 40% dissociated while the carbonate is only 20% dissociated at fully hydrated conditions. Another way to analyze these numbers is to consider the total charge of the free ions and compare that to the total charge available from the membrane. By considering the fraction of free charge, a direct comparison can be made between different scenarios with single or multiple counter-ions. For this calculation, each free ion concentration is multiplied by its valence. The summation of the absolute values is then divided by the charge available in the membrane, the membrane concentration multiplied by its valence, to find the fraction of charge available for transport. For the hydroxide counter-ion case, the fraction of charge available for transport in the membrane is the same as the dissociation of hydroxide in the pores. However, considering the total amount of charge free in the pores for the mixed ion form described above, only 25% of the charge is free in the pores. The mixed ion form has been shown experimentally and numerically to have a smaller ionic conductivity than the hydroxide form. This is explained by a decrease in charge available for transport, as well as lower ionic diffusion coefficients in the membrane.

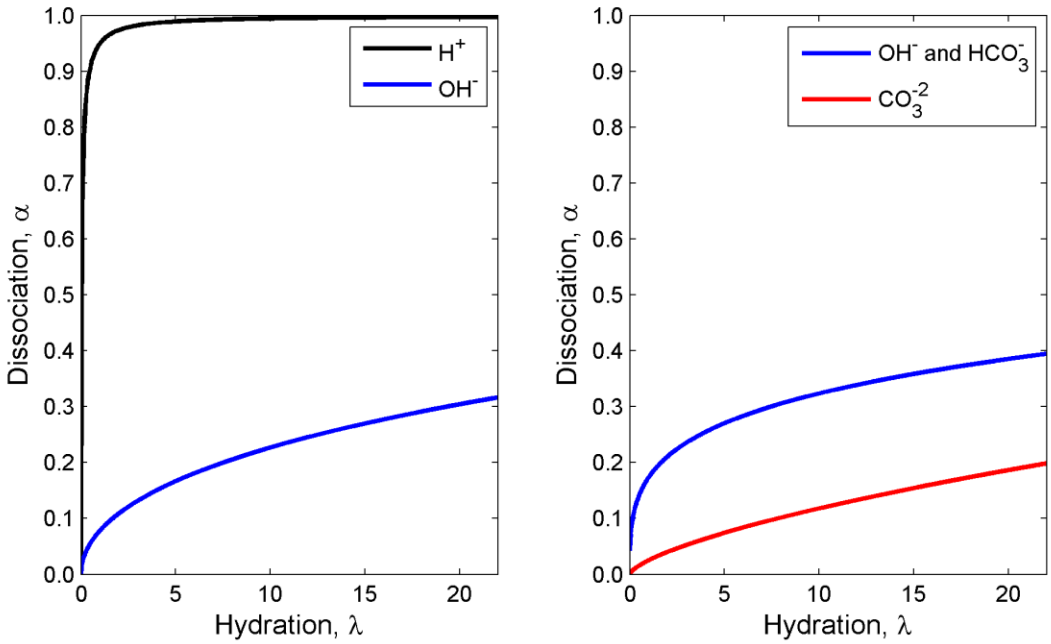

Figure 2.14: Both figures display the fraction of dissociated ions in the membrane. (left) Shows the difference in dissociation for single counter-ion systems: H^+ with Nafion 117 PEM and OH^- with Excellion I-200 AEM. (right) When Excellion I-200 AEM is exchanged to a mixed ion form, the dissociation of each ion can be solved. Hydroxide and bicarbonate have higher dissociation fractions than carbonate.

Absorption/Desorption Testing

The results of this experiment do not include any absorption or desorption effects at the membrane-gas interface. When validating the water-Nafion diffusion coefficients, this approach was able to agree with a technique which would not demonstrate this effect. For this reason, any interface resistances were considered negligible.

Presenting this work, the topic of interface resistances came up multiple times. In order to address this issue, a collaboration was formed with Illinois Institute of Technology (IIT) with Prof. Vijay Ramani and, at the time, his Ph.D. student Chris Arges. Through this collaboration, they would supply membranes of different thicknesses which could be studied to see if the diffusion coefficient varied between membranes of different thicknesses. If there are any interface resistances, they would be accounted for in the diffusion coefficient. As the membrane becomes thinner, the interface resistances should become more significant, while diffusion would be more significant with a thicker membrane. This study would provide direct evidence of, or disprove, any interface effects. The collaborators were most interested in the water- and ion-membrane diffusion coefficients for their membranes as well as ion dissociation data.

Unfortunately, there were several difficulties which left this collaboration unsuccessful. Many AEMs suffer from degradation when put in the hydroxide form due to several degradation pathways. These membranes seemed to exhibit accelerated degradation when put in the hydroxide form and exposed to the water flux setup. The membranes formed considerable cracks and holes during the heating process to 40 °C which took about an hour. When the test was run overnight, roughly 16 hours, the membrane was destroyed and heavily degraded. The accelerated degradation could be attributed to the high concentration of hydroxide ions in the pores. Originally, these membranes were exposed to the same conditions as the Excellion I-200 AEMs

with 95% relative humidity on the humid side and 0% relative humidity on the dry side. This significantly dries out one side of the membrane which increases the pore concentration of hydroxide ions. With a higher concentration of hydroxide ions, there is an increased risk of degradation due to hydroxide attacking the membrane. These effects were not experienced using the Excellion I-200 AEM however Excellion I-200 has a polypropylene backbone while the membranes provided from IIT has a polysulfone backbone.

When the membranes continued to fail in the hydroxide form, it was decided to test the membranes in the more stable chloride ion form. This form has similar water uptake properties but does not provide the chemical degradation of the hydroxide ion form. While this solved the chemical degradation of the AEM, another challenge with these membranes seemed to be the mechanical stability of the membrane. When the membrane was in the liquid water equilibrated state, it was fairly flexible and could seal against the graphite flow channels well. However, when the gas started flowing across the membrane, it would start to dry out and the hydration would decrease. The decreasing hydration would cause a volume decrease and the membrane would contract. In order to create the gas tight seal, the compression bolts would need to be tightened fully to 5.65 N-m and this inflicts a significant amount of force onto the membrane. Using estimates for lubricated bolts, the force per bolt is roughly 4 kN (900 lbf) (Norton, 2006). This force fixed the membrane in place where it was in contact with the lands. This is not an issue in steady state, but while the membrane in losing water and contracting, stresses can build and cause cracks to initiate. These cracks would grow as the membrane would continue to approach steady state until a hole would form and crossover would occur. This failure would provide reason to disregard these measurements.

There were several attempts made to prevent this significant decrease in volume and failure. Some membranes were slowly dried such that they were dried flat (to the human eye). When installed in the water flux assembly, these membranes did not produce the expected back pressure for the flow channels. When testing with Nafion 117 PEM or Excellion I-200 AEM, the back pressure due to the flow channel was consistent with impermeable membranes such as aluminum foil and PTFE membranes. With these dried membranes, the back pressure was significantly lower and suggested that the gas was not following the flow channel. This would introduce inconsistencies when trying to match the experimental and modeling results, which assumes the gas follows the flow channel.

Since a dried membrane was not sealing properly on the flow channels, an attempt was made to dry the membrane while in the water flux assembly. This was done by first equilibrating the membrane in liquid water and installing it in the assembly. The compression bolts were only torqued to 1.1 N-m (10 in-lb). This value was used because it provided a more repeatable measurement than “hand tight” and it was the lowest value which could be controlled by the torque wrench. The experiment was then run for a few hours to let the membrane achieve steady state before increasing the torque on the bolts by another 1.1 N-m (10 in-lb). This was repeated until the bolts reached 5.65 N-m (50 in-lb). Again, the back pressure did not reach the expected value.

In order to prevent significant contraction, instead of running the experiment with 95% relative humidity on the humid side and 0% relative humidity on the dry side, roughly 58% relative humidity, saturation temperature of 30 °C, was run on the drier side. The value of 58% was chosen based on the fact that the water flux assembly would run at 40 °C and the water bath could be maintained at a comfortable temperature above ambient. With the experiments close

proximity to a west facing window and facilities inability to control the heating and cooling systems at C2E2, a water bath temperature of 30 °C was high enough that ambient temperatures would not rise above this so the heaters could control the temperature. Using a lower water pressure difference, and higher humidity conditions, could prevent the amount of volume expansion/contraction and provide better sealing in the assembly. Humidifying the drier side did not provide any better results.

While the potential was very high for this collaboration, a series of complications distracted from the goal of this work. If water flux measurements were possible with this setup, then water- and ion-membrane diffusion coefficients could have been measured. This would have provided evidence which could show the significance of interface effects. Unfortunately, there were several obstacles including chemical and mechanical degradation which prevented reliable water flux measurements. If the experimental setup could successfully test the membranes and valid data could be collected, that some important conclusions could be made which would benefit the scientific community. Several techniques and operating conditions were attempted however the results were invalid and the overall test was unsuccessful.

Conclusions and Scientific Impact

Understanding water transport in low temperature fuel cell membranes is important for water management in the fuel cell. The membrane performance is directly related to the local hydration which should be maintained as high as possible for the highest ionic conductivity. To understand water transport, an accurate representation of the water-membrane diffusion coefficient is required. With the limited knowledge of AEM water diffusion coefficients in the literature, an experiment was built to investigate water transport in AEMs.

A permeation based water flux experiment was built to provide a wide range of hydrations in the membrane for testing. The experiment was run in parallel with a numerical model, MP09, to predict water flux and water-membrane diffusion coefficients. After validating the experiment using a Nafion 117 PEM, water flux testing was performed using Excellion I-200 AEM. This membrane did not transport water as easily as Nafion 117 PEM and showed a much lower water flux. This was confirmed using the numerical modeling which calculated a water-membrane diffusion coefficient as a function of local hydration and temperature. An attempt to investigate interface effects like absorption and desorption was performed but was unsuccessful. While this data would benefit the literature as confirmation that these effects are not significant, this does not change the validity of the water-membrane diffusion coefficient results since the experiment and model were able to match a technique which does not exhibit these phenomena.

The water-membrane diffusion coefficients could then be used as a basis to calculate ion-membrane diffusion coefficients. Principles from kinetic theory were used to scale the effective water-membrane diffusion coefficient to an ion-membrane diffusion coefficient. The scaling was done using values which could be found in the literature such as mass and hydrated radius. The reported ion-membrane diffusion coefficients for hydroxide, carbonate, and bicarbonate are

functions of local hydration and temperature. Each ion diffusion coefficient can be used to calculate the ion's contribution to the total ionic conductivity of the membrane.

By manipulating the dusty fluid model and Ohm's law equations, an equation for the total ionic conductivity of the membrane can solved. The ion-membrane diffusion coefficient equations can be input to this equation to solve the membrane's ionic conductivity with each ion. Using experimental values, dissociation constants were solved for and reported for hydroxide, carbonate, and bicarbonate in Excellion I-200 AEM. The total ionic conductivity of the membrane can be solved as a function of hydration and temperature.

The approach outlined can be valuable as a way to study water transport and predict membrane ionic conductivity in new fuel cell membranes. The predictions can be dependent on the local hydration and temperature in the membrane to arrive at the most accurate results. The diffusion coefficients can be used as a tool to improve on membrane chemistry and design membranes a higher dissociation of counter-ions and higher ionic conductivity.

Chapter 3: Solid Oxide Fuel Cell Anodes

Introduction

State of the art solid oxide fuel cells (SOFCs) utilize nickel and yttria-stabilized zirconia (YSZ) anodes and operate at elevated temperatures ranging from 600 to 1000 °C (Faes *et al.*, 2012, Sarantaridis & Atkinson, 2007). These systems are a popular choice for stationary power applications provided their ability to run on natural gas and provide high quality steam (Larminie & Dicks, 2003, Mench, 2008). Researchers have been focused on extending the lifetime of these devices and understanding the degradation mechanisms. One degradation mechanism is the oxidation of nickel in the anode. During the oxidation process, there can be a significant volume expansion, 70% based on density data, and a decrease in electronic conductivity. This volume increase can form cracks and eventually lead to anode-electrolyte separation and cell failure (Faes *et al.*, 2012, Sarantaridis & Atkinson, 2007).

To study nickel oxidation, groups have used both *in situ* and *ex situ* techniques (Atkinson, 1985, Jeangros *et al.*, 2010, Karmhag *et al.*, 1999). Unfortunately, these techniques have not been able to directly observe and measure oxidation at SOFC operating conditions. In order to accomplish this, an environmental chamber will be designed for use in a synchrotron based full field transmission X-ray microscope (TXM). The environmental chamber will be able to control the gas environment around the sample and heat the sample to SOFC operating temperatures. Using a synchrotron based TXM allows for a high brilliance, monochromatic X-ray beam that can image the sample down to the 17 nm resolution (Vila-Comamala *et al.*, 2012). Also, the monochromatic beam allows for absorption techniques such as X-ray absorption near edge structure (XANES) to be used to identify the oxidation state of the sample (Nelson *et al.*, 2011). Imaging the sample at the tens of nanometer scale while the oxidation reaction is occurring will allow for the morphological changes to be recorded and the reaction rates to be measured.

The TXM has several important components which are vital to its operation. The incoming synchrotron radiation passes through a monochromator to isolate a single wavelength of light. The light will pass through some alignment optics before reaching a capillary condenser lens. The condenser directs the X-rays through a pinhole and onto the sample where some of the signal will be absorbed. The sample is held using stages which can translate in the three spatial directions as well rotate. The transmitted X-rays are then focused by a Fresnel zone plate onto a charge-coupled device (CCD) camera. The zone plate is important for the spatial resolution of the image and new manufacturing techniques have been able to create zone plates that can achieve 17 nm resolution (Vila-Comamala *et al.*, 2012). The TXMs located at the different synchrotron facilities are unique and use slightly different hardware but all have these components (Liu *et al.*, 2013, Shen *et al.*, 2007). There are important differences in the optics which lead to differences in range of X-ray energies available, spatial resolution, and working distances. The working distance is especially important for the design of an environmental chamber which needs to fit between the pin hole and the zone plate. This will be discussed further with the design of different environmental chambers.

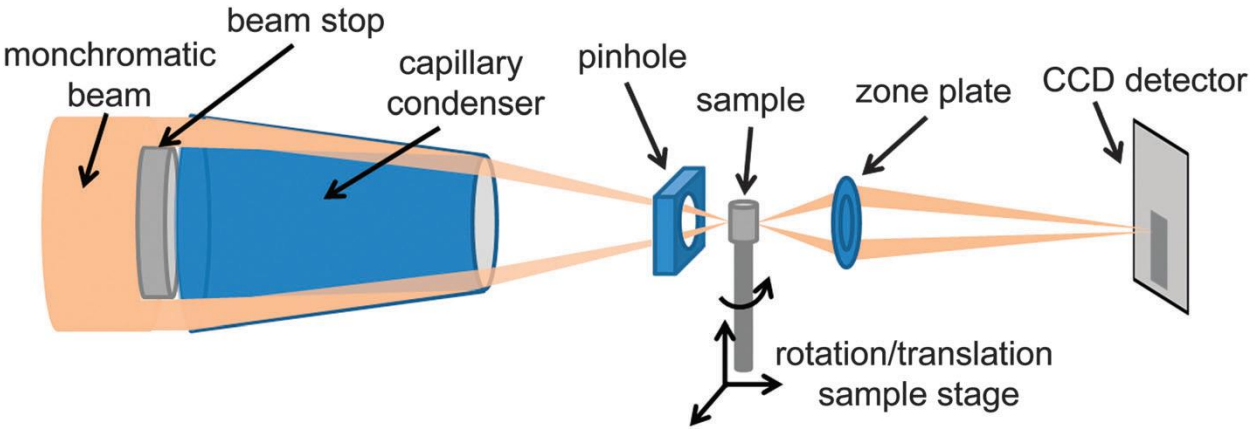

Figure 3.1: A schematic of a typical TXM. For *in situ* testing, an environmental chamber is installed over the sample between the pinhole and the zone plate (Cocco *et al.*, 2013).

Using the TXM, there are different types of images taken and these images can be processed differently. For clarification, a few definitions and their meaning will be described. A *background image* is a transmission image which shows any artifacts as well as the reference beam intensity distribution. The sample is not present in this image. The number of counts in each pixel is recorded and treated as the reference incoming signal for that location, I_0. A *projection image* is also a transmission image with the sample moved into the field of view. Since the sample is attenuating some of the signal, fewer counts will be in pixels corresponding to the sample so these locations will appear darker. These pixel values can be represented as the actual intensity with the sample, *I*. An *absorption image* will refer to the background corrected projection image. In creating an absorption image, each pixel will display optical density information. The optical density, *OD*, can be defined using the Beer-Lambert Law where the incoming signal is related to the final signal by the absorptivity, μ, and the path length, *ds*. The absorptivity is a function of the energy level of the X-rays and the material it is traveling

through. If the sample does not move into the path for a particular pixel, the signal should not change between the transmission and background images, and the optical density will be zero. If there is a significant change because of attenuation of signal from the sample, then the optical density will be some value greater than zero. Displaying these images show higher levels of absorption as brighter regions. Each image should be corrected by applying the background image before processing. This will remove any artifacts and account for the distribution of the beam.

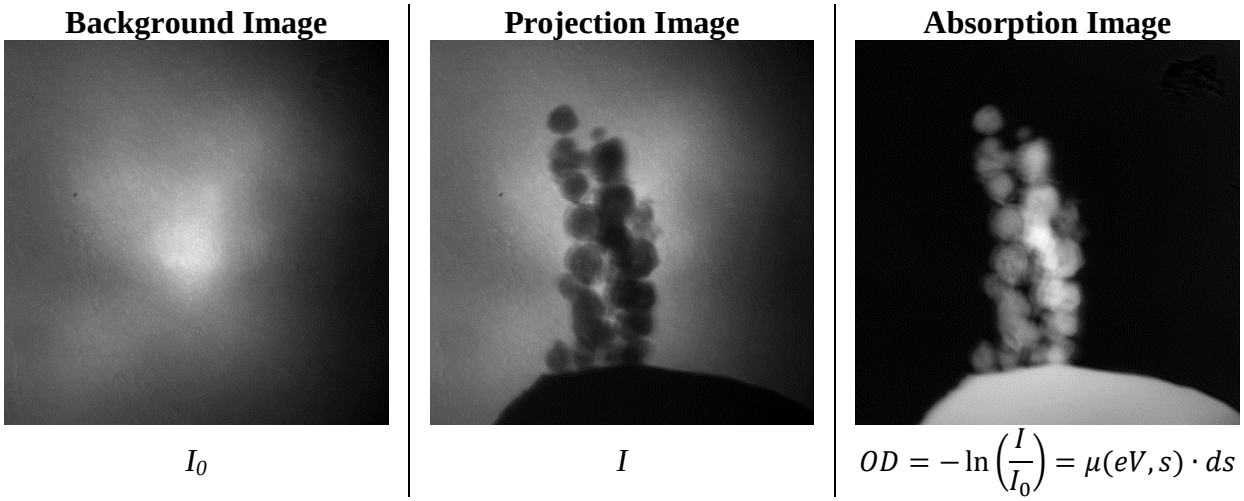

Figure 3.2: The different types of images which will be discussed in this thesis. The absorption image will be the focus of the processing but is calculated based on the background and projection images.

One of the benefits of using a synchrotron based TXM is the monochromatic X-rays which are available. The absorption properties of a material are dependent on the energy of the incoming X-rays and absorption techniques can identify different materials by scanning across absorption edges. X-ray absorption near-edge structure (XANES) looks at the absorption

changes across a particular absorption edge to identify the chemical species. Reference absorption spectra can be collected for nickel and nickel oxide (NiO) measuring absorption across the nickel K-absorption edge at 8333 eV. The absorption spectra can be normalized by the below and above edge values. As seen in Figure 3.3, the normalized spectra show a characteristic absorption peak in the NiO spectrum which is absent from the Ni spectrum. This peak, known as the white line peak, is used to quantitatively measure the progress of the reaction.

Performing a full scan across the absorption edge can be time consuming and difficult to justify in the middle of an oxidation experiment. To save time, detailed reference spectra at collected for Ni and NiO before any testing has begun. During testing, only 4 energy levels are considered to identify the oxidation state of sample based on the detailed reference spectra collected. The 4-point XANES can consist of 1 point below the edge, 1 point at the white line peak, and then two points above the edge where the absorption should be similar. These points can provide enough information about the sample to confirm the oxidation state of the sample. Tests have been conducted using the energies 8316, 8348, 8358, 8376 eV. When normalized by the endpoints, the magnitude of the white line peak at 8348 eV can be used to track the degree of oxidation and confirm the reaction has completed.

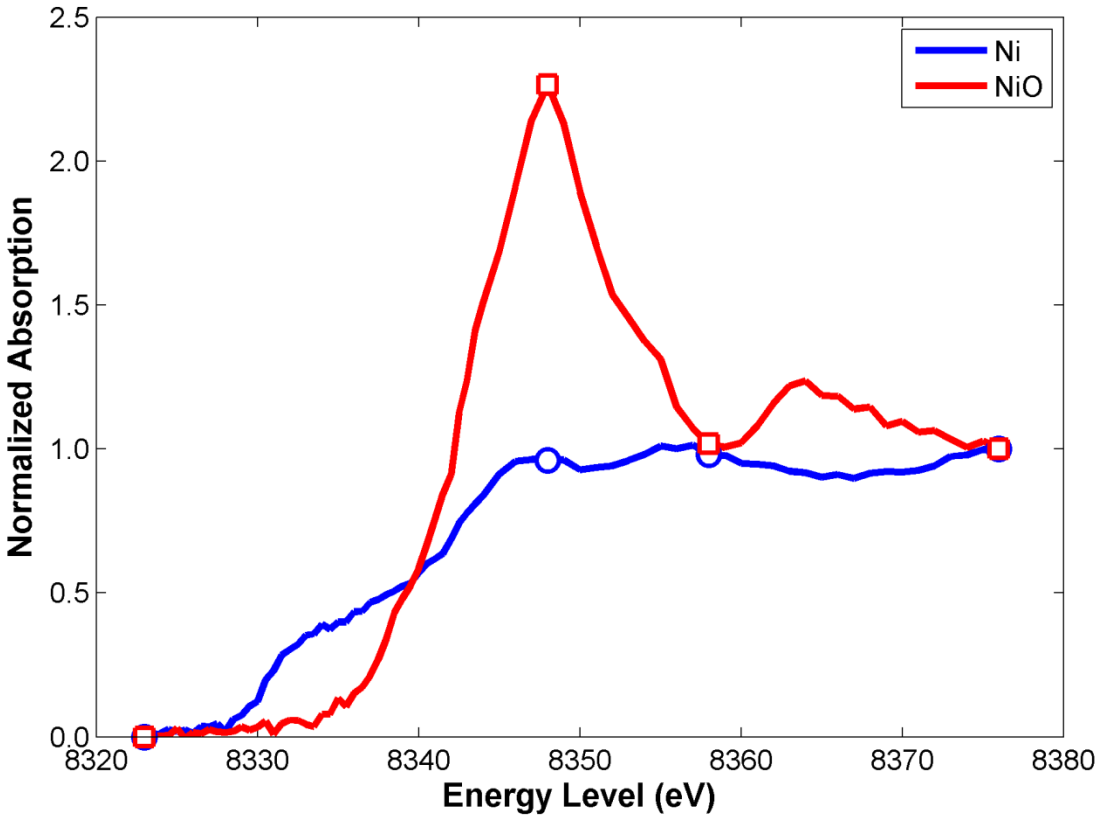

Figure 3.3: A normalized spectrum for nickel and nickel oxide. The symbols represent the points used for the 4-point XANES spectrum (Kiss *et al.*, 2013a).

Environmental Control

These experiments were conducted using multiple heater designs and TXMs. Although the microscopes are all similar, they each have their own set of hardware and customizations which make designing one system difficult. Over the past few years, the project has developed and heater designs have evolved to meet desired requirements. There are five different heater designs which have been utilized in the microscopes. Of these, only two heaters have yielded useful results but some notes on some of these heaters will follow to document some of their advantages and shortcomings.

APS Heaters

Much of the early development was performed through collaboration with the Advanced Photon Source (APS) beamline 32-ID. Here, the optics allow for a large working distance between the pin hole and the zone plate. This makes it easier to design and operate a heater which could achieve SOFC operating temperatures. The work presented here was performed using an older microscope at this beamline. The new TXM is still overcoming some challenges so the *in situ* setup has not seen operation in the new microscope but there is a set of optics which can hold the environmental chamber.

One of the first heaters developed used thermal radiation from a heat lamp. Using a 250 W bulb, the infra-red radiation was focused down to a small volume where the sample would be located. This would heat the sample to the desired temperature. Using this technique could heat the sample to the desired temperature in seconds. The bulb was installed in a holder which focused the heat to the sample and helped prevent heat from escaping to the optics. This heater design was able to provide oxidation results for nickel. Since the experiments were successful,

the holder was modified so that it could be used in the TXM at NSLS which has a much smaller working distance.

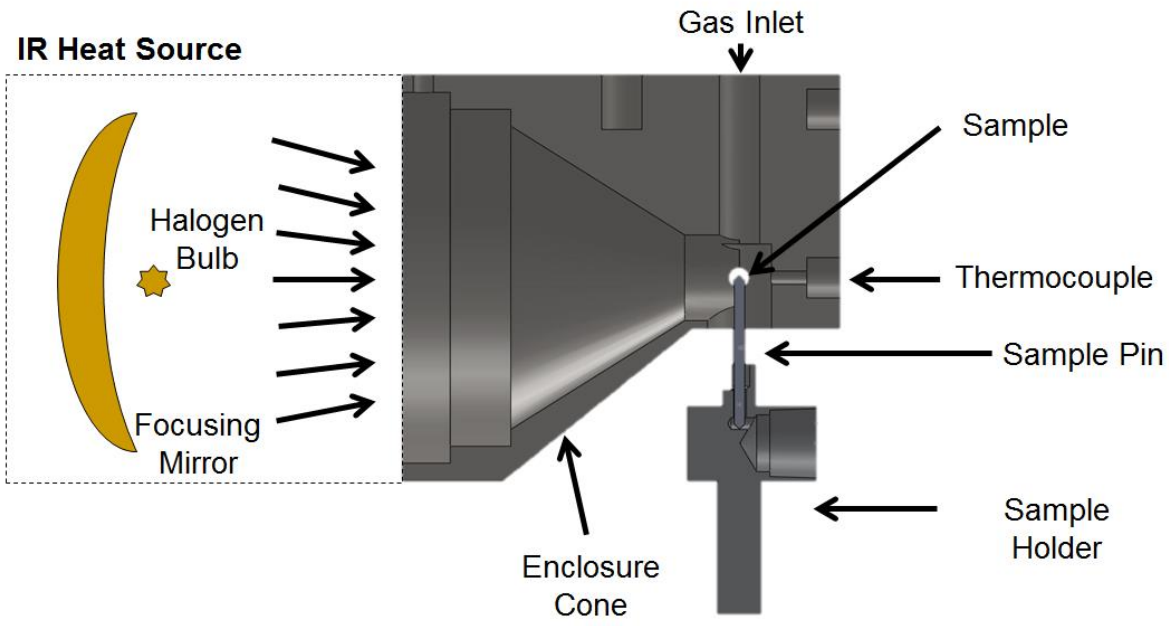

Figure 3.4: The infra-red heat is focused to the sample position. The sample, held on the tip of a pin, is maintained in the field of view of the microscope for imaging (Kiss *et al.*, 2013a).

Unfortunately, there were several difficulties using this approach and heater. The bulb would frequently burn out because it was overheating. Nitrogen cooling gas was fed behind the bulb to help keep it cool but there was still a short lifetime associated with the bulb. Also, when replacing the bulb, it was difficult to locate the new bulb in the exact position that the old bulb was in. This new position may move the heated volume and change the temperature calibration for the sample in the field of view. Using this heater did not provide a means for gas control and

only oxidation experiments could be run in ambient air. With the lack of gas control, this heater made it challenging to maintain the sample in the field of view. When the heater was powered on, the sample and pin would start to thermally expansion and the sample would move out of the field of view. This displaces the sample from the calibrated heated volume and it does not provide any useful images for studying the reaction. The sample could be moved back into the field of view using the TXM stages and this would continue until thermal equilibrium was reached. During warm up, it would be difficult to image the sample since it is moving and creates blurry images. This prevented a significant number of images to be taken at the beginning of the reaction.

To improve on the heater design, a ceramic resistance heater was considered. A Fiber Heater (MHI Inc.) was purchased and modified to fit the beamline needs. This involved adding some holes for the X-rays to pass through. The heater consists of a molybdenum-disilicide ($MoSi_2$) ceramic heating element which is encased in alumina. The heating element is located in the heating chamber and shaped in a spiral so that the temperature distribution will be fairly uniform. For feedback, a B-type thermocouple (70/30 Pt/Ru – 94/6 Pt/Ru) is located in the heating chamber. The heater is powered by a low voltage/high current DC power source and is capable of reaching temperatures in excess of 1500 °C.

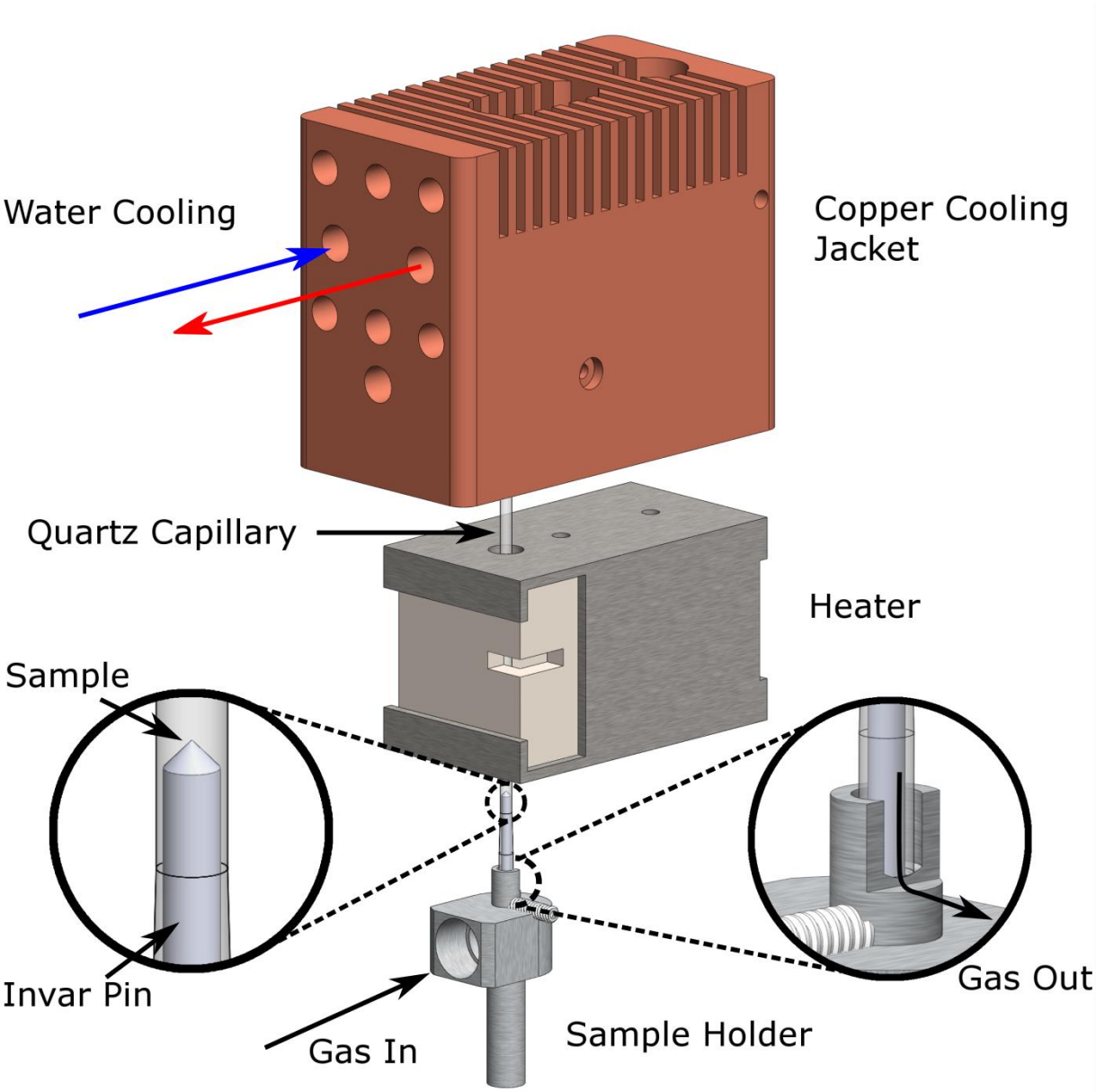

Figure 3.5: A schematic showing the components to the ceramic resistance heater design. The sample is placed on the tip of a pin and the heater is lowered over the sample. Gas is fed into the sample holder, around the sample, and then exhaust at a step at the bottom of the capillary.

While the alumina in the heater helped prevent the heat from escaping, the X-ray optics can still be damaged by the heat. To protect the optics, a copper cooling jacket was manufactured to be installed over the heater. Copper was chosen as the material of choice because of its high thermal conductivity and high melting temperature. Holes were drilled in the cooling jacket and then covered with aluminum foil to minimize heat escaping and attenuation from the cooling jacket. While there were fins machined into the top of the heater to help cool the jacket, majority of the heat was removed by running water through the jacket. Water cooling channels were machined into the cooling jacket and worked extremely well at removing heat. Water was pumped through the cooling jacket and then into a water chiller which was set to maintain 20 °C. Even when the inside of the heater was operating at 1000 °C, the outside of the cooling jacket was cool to the touch. This protected the X-ray optics from any thermal expansion and heat damage.

The ceramic resistance heater was able to perform exceptionally well. Modifications were made to the setup to include gas control by using a quartz capillary tube. The infra-red heater design struggled with maintaining the sample in the heated volume and the field of view. With the ceramic resistance heater, the spiraling heating element provides a uniform temperature distribution. Although the heater takes roughly 45 min to 1 hour to get to operating temperature, the gas environment can be controlled and the sample can be heated in an inert environment. Once the heater has reached steady state, the pin and sample will not be thermally expanding and it will be much easier to maintain the sample in the field of view. With gas control, there is also the possibility to study many reactions such as oxidation or reduction.

This heater was able to successfully provide nickel oxidation, and some reduction, data at elevated temperatures. Unfortunately, time with the TXM is difficult to come by and a new TXM

was being built. This made it difficult to continue developing and working with this heating setup. Also, the ceramic resistance heater is much bigger than what can be accommodated at NSLS. The heater by itself has a width of roughly 32 mm along the length of the beam. With the cooling jacket this grows to 40 mm. In order to fit comfortably in the TXM at NSLS, the total width would need to shrink to roughly 13 mm.

NSLS Heaters

After difficulties with modifying the infra-red heater from APS for use at NSLS beamline X8C, a new heater was developed by the scientists. This heater uses an 80% nickel 20% chromium alloy (Ni-Cr) wire as a heating element. The Ni-Cr wire was wrapped around the outside a small Macor (Corning, Corning, NY) tube and inserted into a larger Macor tube so that the wire is electrically isolated. The tubes are then inserted into a copper jacket which has water flowing through it. This heater is much thinner than the ceramic resistance heater, at 13 mm, and fits in the limited working distance of the microscope. Aluminum foil is put around the optics to help minimize heat transfer and the pin hole temperature is monitored using a thermocouple.

This heater design ran into a wealth of issues and was unable to oxidize any samples. Similar to the infra-red heater, this design only allows for use in ambient air. The water cooling method consisted of pumping water up to a reservoir and then gravity feeding the water through the heater and into a container on the floor. The water temperature was not monitored and was not chilled. Before operating the heater, it is important to make sure the water reservoir is not leaking since it is located above the power supply controlling the heater. It was really shocking to see this setup was not modified from the scientists when even after water had leaked onto the power supply. Although nickel and chromium can help minimize oxidation in alloys, when operating at high temperatures, the wire itself would oxidize and over time could fail. If the wire

is replaced, it is important to recalibrate the heater since the new wire can create a considerably different temperature distribution. Finally, holes were machined in the Macor to allow for the X-ray beam. When the wire was heated, there was thermal expansion and this would cause the Macor tubes to rotate and block the X-ray beam. This heater design proved unsuccessful for *in situ* and oxidation studies.

SSRL Heaters

The microscope at Stanford Synchrotron Radiation Lightsource (SSRL) beamline 6-2C has a working distance which is comparable to that of the APS TXM. This would imply that the ceramic resistance heater could work in this beamline. The only issue is the heater is extremely delicate and would most likely break during shipping. To continue extending *in situ* capabilities, the scientists at SSRL had developed a metal resistance heater which could operate up to 450 °C. The heating element was made of Kanthal wire (Sandvik, Hallstahammer, Sweden) so that it was more stable in an oxidizing environment. Kanthal is typically an iron-chromium-aluminum alloy which, when heated, will create a passivation layer on the surface to protect itself from further oxidation. The wire is wrapped around the heating volume. This heater was designed to have a particularly large heating volume such that the sample could rotate inside the heated volume for tomographies. Since the heater was achieving lower temperatures, the cooling jacket was made out of aluminum but still had chilled water cooling it. This heater was not considered for the nickel oxidation experiments because of its low temperature operation. Instead, an experiment was designed to consider morphological changes to a nuclear waste form sample (see Chapter 4).

Components

A great deal of thought and consideration went into the different components used in these experiments. For example, the sample holder was designed to hold the sample pin and feed the gas around the sample. These design criteria were considered for the infra-red heater experiments even though the gas environment was not controlled for that series of experiments. An aluminum holder was machined such that it could be held by the microscope stages using a 6.35 mm (0.250 in) shaft. Once attached to the stages, gas could be fed into the holder using an 1/8 inch NPT fitting. The tubing which connected to the 1/8 inch NPT fitting needed to be placed carefully so that it would not hit any of the nearby optics. This was fairly easy for taking two-dimensional projection images since the stages do not rotate. If a tomography was performed, then the stages would need to rotate +/- 90°. Flexible tubing was required such that it could move and deform while the stages were rotating and not bump into any optics. Once the gas was fed into the holder, it was redirected up around the sample pin.

The sample pin was placed onto a step in the holder, for repeatability, and fixed using a small set screw. The hole for the pin was machined to allow for gas to come up around the sample. Several pin materials were considered, including a K-type thermocouple, tungsten and tungsten carbide, Invar, and alumina. The sample was placed on the tip of a K-type thermocouple in order to get accurate temperature readings, however this was unsuccessful. The thermal expansion of the thermocouple was too significant and it was not possible to find the sample after the heater was turned on. To combat thermal expansion, an alloy of nominal 36% nickel and 64% iron known as Invar was considered. Invar is known for its low thermal expansion and is typically used in applications where thermal expansion needs to be minimized. Several Invar pins were manufactured and proved to be useful in keeping the sample in the field of view. Using Invar also introduced a new challenge which was the oxidation of the pin material. Since Invar is

an alloy of nickel and iron, the pin would oxidize during the same conditions as the sample. An oxidation front would grow from the pin surface during oxidation and collapse during reduction. This interfered with the nickel powder sample on the surface so powder farther away from the pin surface was considered. After performing an oxidation and reduction cycle, the pin tip could be cleaned and any loose material removed. This seemed to leave a fairly stable, passivation layer which did not interfere much with the sample.

Even though Invar was useful for helping maintain the sample in the field of view with the infra-red heater, the ceramic resistance heater was capable of controlling the gas environment. This allowed for the sample to be heated in an inert environment and the components to reach thermal equilibrium before testing would start. With this capability, new pin materials were tested. Tungsten and tungsten carbide were considered for their high melting temperature and its use in high temperature applications such as machine tooling. After exposure to temperatures in excess of 700 °C in ambient air, the tungsten carbide had corroded and would not make a stable pin material. Although some might suggest that using this material will work, it can be seen in the figure below that the pin is not stable in a high temperature, oxidizing environment. It is more likely that the heater that they are using is not operating at the temperature they are expecting.

Tungsten Carbide (WC)

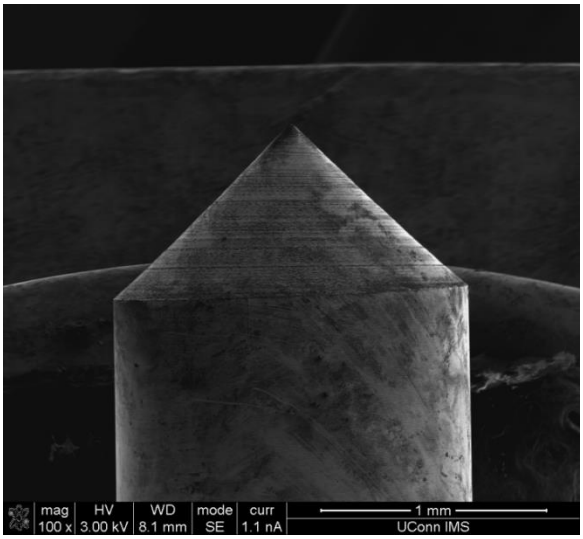

Clean Tip

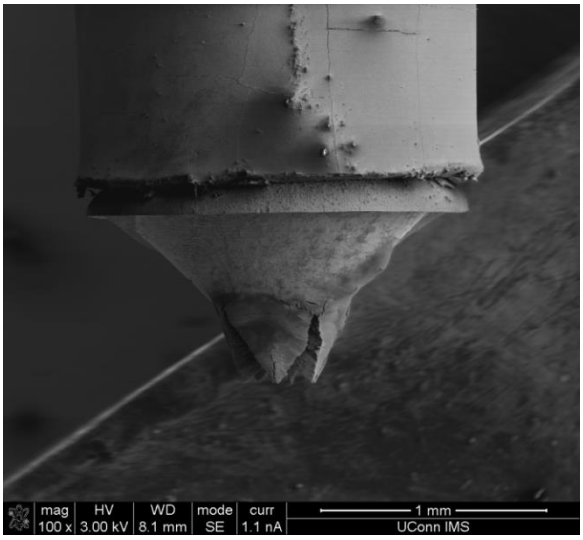

Subject to high temperature, oxidizing environment. Considerable degradation.

Alumina (Al_2O_3)

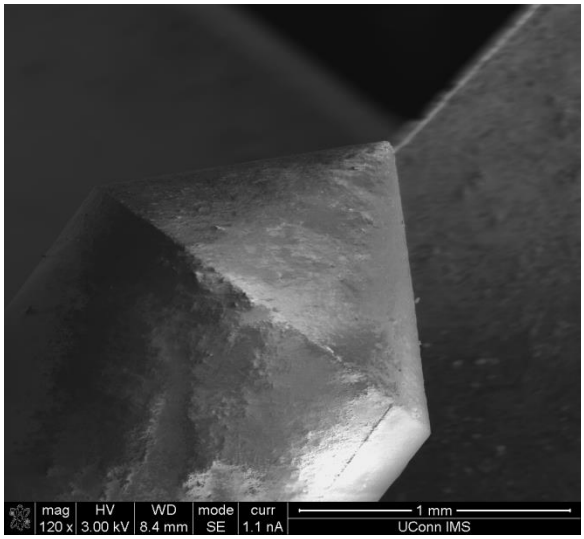

Clean Tip

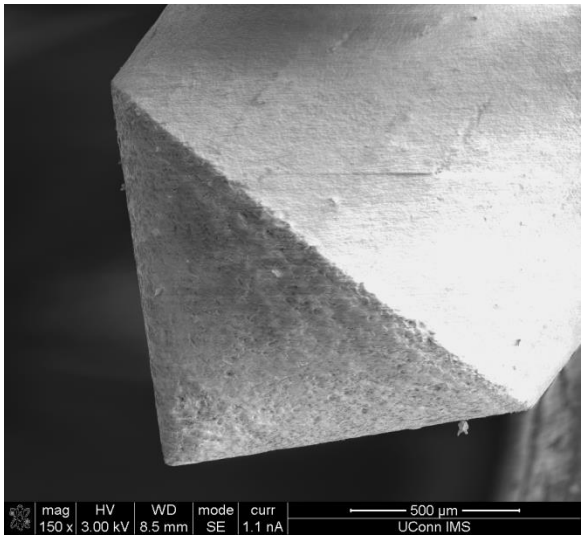

Subject to high temperature, oxidizing environment. No degradation.

Figure 3.6: The left panels are showing the effect of a high temperature oxidizing environment on tungsten carbide pins. While there is significant degradation seen in the bottom left panel, the bottom right panel shows no degradation to the alumina pin after exposure to the same conditions.

With the controlled gas environment, an alumina pin achieved the desired results. Since thermal expansion was not an issue in the inert environment, the sample could be heated slowly and kept in the field of view. Using alumina, the pin material is stable and no reaction was observed when tested in high temperature, oxidizing and reducing environments. The nickel powder sample would not be affected by an oxidation front and could be studied much easier.

The stock material can be purchased in the correct diameter (1.6 mm or 0.063 in) but machining just the tip can be a challenge. The alumina stock is extremely hard and brittle. To machine the tips, the expertise of K&K Precision Manufacturing Inc. (East Berlin, CT) was called upon to create a setup and grind the tips onto the pins. The pins were first cut to their desired length. The pin was placed in a collet with padding on the bottom. The padding was important and to prevent damage to the end of the pin while providing a repeatable location for machining. In the collet, the pin would stick out only a little bit. If it extended too far out of the collet, then it would break during grinding, and if it was not out enough, then the grinding wheel would not be able to machine the tip. The collect was setup at a 45° angle and aligned with a diamond grinding wheel. The grinding wheel would slowly be lower to remove more material. During grinding, the collet and pin would be rotated to grind the entire tip at once. This would be repeated until a point with a radius less than 25 μm (0.001 in) was produced and confirmed using a shadowgraph.

In order to isolate the gas environment around the sample from the ambient, a quartz capillary tube was placed over the sample and sample pin. Quartz capillary tubes (Charles Supper, Natick, MA) were purchased for their ability to withstand the high temperature environment and their wall thickness of roughly 10 μm. The capillary tubes were closed on one end and had an open funnel at the other. The holder was designed to fit that funnel and acted as

an inlet for the gas. There was also a small step which was used as an exhaust for the gas. The capillary tube's thin walls would help minimize the amount of attenuation and signal loss due to the capillary. Even with the thin walls, roughly 60% of the signal was attenuated by the quartz. This increased the exposure time to 10 seconds. Fortunately, the sample did not move significantly because it was already at thermal equilibrium with the environment and quality images could be captured.

Different gases were fed into the quartz capillary to control and study the reactions. The inert environment was controlled using high purity nitrogen (Airgas) or by using boil off nitrogen from a liquid nitrogen tank (Airgas). The oxidizing environment used ultra-zero air (Airgas) and the reducing environment used 4% hydrogen balance helium gas (Airgas). Nitrogen can be used instead of helium but helium is closer in mass to hydrogen and should mix better with hydrogen. The hydrogen concentration was limited to 4% for safety reasons. The flammability limit of hydrogen in air is 4%. These gases were controlled from outside the hutch by using valves. This allowed for the gases to be switched quickly from inert to oxidizer. The flow rate was controlled by using a variable cross section flow meter and set to roughly 25 ccm. It is important not to mix the hydrogen with air for safety reasons. To avoid any mixing, the inert gas was always used to purge the lines before switching between hydrogen and air.

The starting sample for oxidation and reduction was chosen to be nickel powder. Two different nickel powders were used for these experiments. Initially, nickel powder (Alfa-Aesar, Ward Hill, MA) having a particle size of roughly 3-5 um was used. This powder did not have any particular shape but was of the desired size and material. The numerical modeling which accompanied the experiments, assumes that the particle is spherical in shape. This was not necessarily true for this powder and careful consideration of which particles were tracked was

needed. To eliminate this process, spherical nickel powder (Alfa-Aesar, Ward Hill, MA) was purchased. The packaging states that the particle size should be from 5-15 um. The methods used to select particles and place them on the pin tip are more likely to select smaller particles and this is reflected in the analysis. The average particle diameter considered using the spherical particles was 4.0 μm. Using this starting powder, the particles can be properly described as spheres later in the modeling.

Experimental Procedure

In order to perform the experiments, a general procedure was developed. This procedure might differ from one beamline to the next or between heaters, but the process is similar. It is always important to perform a complete and detailed calibration before performing any trials and taking data. Images of the sample should be taken as quickly as possible to minimize blurring from the sample moving or missing changes from the reaction. Before each trial, a XANES spectrum should be performed to confirm that the sample is starting as nickel. The *in situ* imaging will be taken at the white line peak where an increase in the optical density can be observed as the reaction progresses. Once the reaction has completed, a final XANES spectrum should be performed to confirm that the reaction has completed.

Calibration

Beam Calibration

While the beam scientists are extremely helpful and may try to help by performing some calibration, it is important to calibrate separately and make sure the procedures are done correctly. Calibrating the beam is a fairly straight forward and quick process and will not consume a significant amount of beam time. Since this experiment is highly dependent on the calibration of the beam, it is important to have a full XANES spectrum for both nickel and nickel oxide. Finding the absorption edge can be done with a few points, however it is always good to have too much data and be able to reference it later. The XANES spectra can be collected by simply putting a reference sample of nickel or nickel oxide in the beam and scanning through different energy levels. The absorption or optical density can be measured by selecting the same region of interest in each image and tracking the mean or median value. Once complete spectra are collected, the points for a shortened 4-point spectrum can be determined.

Heater Temperature

The temperature inside the heater is also vital to the accuracy of the measurements. The best way to calibrate the heater is to closely simulate the conditions that the sample would be experiencing. If water cooling is available, then it should be turned on. If the sample will be used with the infra-red heater, a thermocouple can be placed in the sample location. If the ceramic resistance heater is being used, then the thermocouple should be placed inside the quartz capillary and gas flowing. Omega K-type thermocouples are used for the sample temperature. The thermocouple has a 0.25 mm diameter to provide a small spot size, and is shielded by using a nickel-chromium based Super OMEGACLAD XL sheath. By using the shielded thermocouple, the bead is protected from oxidation and should have a longer lifetime than an exposed bead. Once the thermocouple is situated in the holder, the beam should be turned on and the tip of the thermocouple should be moved into the field of view. Throughout the calibration, the thermocouple should try to be maintained here since this will be the sample position during the trial. The heater can now be moved over the thermocouple and turned on low. This step is to best try to find the hot spot of the heater. Move the heater around until the thermocouple reads a maximum. Record the position of the heater so it can return to this location. The heater can then be calibrated by looking at the power setting to the heater or feedback heater feedback thermocouple and comparing that to the sample thermocouple. For example, with the ceramic resistance heater, a calibration was made based on the voltage input (current was also measured), and the B-type thermocouple located inside the heater. This provided two guidelines for the temperature. If a sample temperature of 800 °C was required, it was known to drive the heater to 1.74 V, and the B-type reading would indicate how close the heater was to that steady state value. Once the calibration is complete, it is a good idea to perform and three-dimensional map

of the temperature field around the field of view in case the sample moves. This will also confirm that the sample is in the local hot spot.

Gas Delivery

The calibration for the gas delivery through the variable cross sectional area flow meter can be obtained online. While the values might deviate slightly between different gas mixtures or at different pressures, the error is fairly small. The value for the flow rate is not terribly important and is only used as an estimate for purging times and time for oxidizer to reach the sample. Since the purging time should be long enough to displace 4 system volumes, there is room for some variation in the flow rate.

Microscope Stages

One final check that should be performed is whether or not the stages can be moved while the software is acquiring images. If a script can be setup to acquire images automatically, this is much easier for the users but the sample might drift and need to be moved. At APS with the older microscope, the software could be set to perform an "Averaging" scan with "Average on the fly" disabled. This would automatically take images for the user and put them into an image stack. If the sample started to move, a separate computer could be used to control the stages and move the sample. This is not the case at NSLS where the stages are locked when the software is acquiring images. Moving the stages might cause one or two images to be blurry but these can be removed during the post processing. The alternatives are hoping that the sample stays in the field of view, or manually collecting each image, the latter can be especially difficult to collect enough good images to analyze.

in situ Measurements

When the system is ready, the sample can be mounted on the tip of a pin. If necessary, the pins and quartz capillary can be cleaned using a solvent such as methanol and then rinsing with deionized water. Gloves should be worn to prevent fingerprints after cleaning. A human hair, or a bristle from a paint brush, can be dipped into the nickel powder to collect some powder on the hair. The hair can then be mounted on a wooden splint and mounted onto stages. The sample pin is placed on stages opposite the hair. Using an optical microscope, the nickel powder can be placed on the tip of the pin. It is important to put the powder on in such a way that it can be imaged and analyzed. Do not clump the powder on and instead leave visible spheres. Once the powder is on the pin, the pin can be moved to the microscope and installed in the pin holder.

After mounting the pin in the pin holder, some tests should be run before the imaging the reaction. If gas control is available, the inert gas should start flowing to purge the system. It is recommended that the inert gas run so that 4 system volumes of gas have gone through the system. This should take about 20 minutes. If water cooling is available, the water should start flowing through the heater. The beam can then be turned on and the stages moved until the sample is in the field of view. Make sure that the powder can be processed later. If this passes, then the heater can be dropped to its ideal heating location. If the gas environment is controlled, the heater can be turned on and the ramped to its operating temperature. Be sure to track the sample and wait for the system to reach thermal equilibrium. After heating is complete, a 4-point XANES spectrum can be taken to confirm that the sample is still in its original state. If possible, or desired, a tomography can also be performed to get a three-dimensional representation of the sample before oxidation has occurred.

Before switching to an oxidizing environment, be sure to set the monochromator to the desired energy level, typically the white line peak at 8348 eV, and capture one more image of the

sample as well as a background image. If the stages can be moved using the “Average” setting, then start acquiring “Average” images. Be sure that “Average on the fly” is disabled. For this setting, try to take enough images for 20 minutes. At this point, another background image should be taken before continuing with more images. With gas control, the inert gas can be switched off and the oxidizing gas can be turned on. If the heater is not already on, then at this point it should be turned on. And finally, if the “Average” setting cannot be used, start acquiring single images. Take them as quickly as possible and be sure the use a short exposure to prevent blurring. This technique is difficult and should be performed with two people so one person can worry about the heater and the time stamps of the images, and the other can maintain the sample in the field of view and collect the images.

By looking at the projection images, the reaction progress can be monitored. As the particles oxidize, they should attenuate more signal and swell. Using the TXM Controller software, circles can be drawn over the images as they are updated. This is useful for tracking the small changes in volume size as the reaction reaches completion. Once it appears that the reaction has completed, do not shutdown. Perform a 4-point XANES to confirm quantitatively that the reaction has completed. If the sample is still reacting, continue collecting images. Otherwise, the shutdown procedure can begin.

To shutdown the experiment, turn off the reacting gas and start the flow of inert gas. The heater can then be ramped down and powered off. Once the setup has cooled and reached thermal equilibrium, a tomography can be performed to get a final structure of the powder. This procedure can be repeated for multiple temperatures to measure a dependence of temperature on the reaction rate.

Image Processing

Once all of the data has been collected, the post-processing can begin. The data analysis can be performed using Microsoft Excel, GIMP, some MATLAB scripts, as well as TXM Wizard (Liu *et al.*, 2012). TXM Wizard has been in development by the scientists at SSRL and is a free alternative which is capable of performing many of the functions available from the Xradia software. The SSRL team has also provided us with the source code to some of their functions and they have been utilized in some of the work.

Before focusing on a specific trial, the XANES spectrum should be analyzed and complete conversion confirmed. The XANES spectra taken before and after the reaction should be corrected to become absorption images. This requires one background image for each energy level in order to properly correct the projection image. The absorption images can be created using the TXM Wizard software. There is a button located on the main window for "External Reference" which can be used to select the background and projection images to make an absorption image. The absorption images can then be used for image processing.

To analyze the XANES spectrum, chose a particle(s) which stays in the field of view during the oxidation reaction. Be sure that each image has been corrected to display optical density information. Using a script in MATLAB, select the particle(s) to be considered. It is important to only select the desired particles to be studied. Selecting a larger area that doesn't capture any particles is acceptable. The background area should have an optical density of zero, since there is little to no absorption in air. To help minimize noise, a threshold value is used so that any pixel with an optical density less than 0.13 is considered zero. The total optical density is summed in the selected region of interest and normalized by the endpoints. Hopefully, the resulting XANES spectra will match the reference values for nickel and nickel oxide. There will

be some scatter associated with selecting different regions but the values should be fairly close to the references.

Once the particle is known to oxidize, the processing of the *in situ* images can begin. While during the beamline trip, hopefully data was collected using the "Averaging" approach. This creates *.txrm files which are a stack of images. Using the TXM Wizard software, the individual projection images can be extracted from the stack using "Data Evaluation → TXRMtoBin". If the "Average" could not be performed, then a series of *.xrm images were taken and the processing can begin here, but with fewer images. For each image, there should be an associated timestamp. It does not need to begin at the beginning of the reaction and can start when the imaging begins. With the "Average" technique, this is simple since the software is set to take images continually with a given exposure time. More care needs to be taken with the manual image technique which is why it helps to have two people so one can record timestamps.

Background images were collected before, during, and after the reaction occurred and should be applied to the projection images before further processing. Applying the backgrounds needs to be done with care. If this is done incorrectly, then there can be noticeable differences when switching from one background to another. To help alleviate this issue, a background image is interpolated for each projection based on the timestamp. This helps prevent the significant changes in the background and a smooth transition from the first background to the last. A MATLAB script was written which can input two background images and a timestamp vector to interpolate the required background images.

With a background image for each projection image, the absorption images can be produced by using Beer-Lambert Law. This step can be easily conducted using the TXM Wizard and the "Data Evaluation → Data Ref" feature. This set of absorption images will be exported to

a new folder so that no data is deleted. If that folder is opened in the TXM Wizard main window, the files can be play through to qualitatively check the image quality and look for any images that are blurry. These images can be removed since they will not produce valid data. With the images loaded in the TXM Wizard, the particle may drift or move during the reaction. The images can be aligned by choosing a point, such as the very top of one of the spheres of interest, in each image. By clicking "Recon Central Slice", TXM Wizard will align all of the images based on that point and export the aligned images to a new folder. Now that the images are aligned, it will make selecting the same particles easier.

For this analysis, a change in the optical density is being monitored over the reaction. A MATLAB script has been written which can load the aligned absorption images and total the optical density in a given region of interest. Similar to the XANES script, it will only consider values above a certain threshold so a larger region containing not containing the sample can always be selected. This is useful since the particles should grow over time. The script will run through each absorption image and ask the user to select the same particles. If the samples are stable and the alignment is good, then there is an option where the user can select the region of interest once and the program will use that same region of interest for each image. This is useful for large stacks of aligned image data. The optical density will be saved and plotted. This provides a more quantitative way to look for anomalies in the data and see if any images need more careful processing or should be removed. The optical density plot should provide clear evidence of an initial optical density before oxidation and a final optical density. These values can be used to normalize the optical density data such that the normalized data starts at zero and ends at one.

Unreacted Core Model

In order to capture the physics in the oxidation process, a modified unreacted core model was used (Levenspiel, 1972). The shrinking core model is capable of analytically solving the time required for complete oxidation of the particle. With the original model, a sphere is assumed to undergo a chemical change with a constant flux of reactant gas. Mass transport is neglected meaning the concentration of reactant gas is assumed to be the same at the reaction interface and air. This is not necessarily true given that diffusion processes would need to take place in order for the Ni to be oxidized. The diffusion coefficient for Ni through NiO is orders of magnitude greater than that of oxygen through NiO (Kofstad, 1966). In order to check that mass transport was not limiting, a calculation was done using Fick's law and the concentration had less than a 10% drop over a 1.5 μm radial distance. The unreacted core model is capable of modeling the Ni core of the spherical particle as it shrinks and becomes consumed, converting to NiO. The fundamental equation in this model is seen in Eq. 3.1 where the molar flux of Ni is assumed to be constant and related to a stoichiometric reaction coefficient, *b*, a reaction rate constant, k_c, and oxygen concentration, C_{O_2}. The molar flux is calculated based on the Ni core surface area and the rate that Ni is consumed. Both of these expressions can be related to the core radius, r_c.

$$-\frac{1}{4\pi r_c^2}\frac{dN_{Ni}}{dt} = bk_c C_{O_2} \qquad [3.1]$$

$$r_c = r_0 - \frac{bk_c C_{O_2}}{\rho_{Ni}}t \qquad [3.2]$$

This equation can be manipulated to solve for the core radius at any time, *t*. This allows for the time necessary for complete oxidation to be solved for the starting radius, r_0.

The shrinking core model can provide information on the Ni core however the NiO layer needs to be considered by a numerical model which would simulate optical density of the particle. As the Ni oxidizes, the volume increases by about 70%. In the transmission images, two phenomena would be seen with oxidation: an absorption change from the changing species, but also a volume change and increase in path length. With the unreacted core model, a quantity of Ni in the core was known at any time. The total quantity of Ni atoms was fixed and could be distributed between the unreacted Ni core and the NiO shell. Knowing the amount of Ni present in the core at any time can correlate back to the amount of NiO needed to maintain that molar balance and solve for a particle radius, r_p, based on a ratio of molar volumes, *z*. A similar approach was used by Carter (Carter, 1961) where an unreacted core is consumed and the particle grows in size.

$$r_p^3 = z r_0^3 - r_c^3(z-1) \qquad [3.3]$$

With the core radius and particle radius known for any time, the total optical density can be calculated based on attenuation coefficients for the two phases, μ. Since a sphere is assumed for the shape of the particle, an integral over the sphere can be evaluated to find the total path length through the Ni core and the NiO shell. The sum of the optical density over the entire particle can be done using Eq. 3.4.

$$\sum_{particle} OD = \left(8 - \frac{16}{\pi}\right)\mu_{Ni} r_c^3 + \left(8 - \frac{16}{\pi}\right)\mu_{NiO}\left(r_p^3 - r_c^3\right) \qquad [3.4]$$

This equation can be used to sum the optical densities over several particles. This can be useful for particles that can be approximated as several spheres as well as helping to minimize error related to noise in the data.

Temperature Correction

An exposed K-type thermocouple was used for the temperature readings inside the environmental chamber. These thermocouples are made using two alloys, alumel and chromel, which are both mainly comprised of nickel. The K-type thermocouple was chosen due to its large range of operating conditions as well as the linear temperature response (Figliola & Beasley, 2006). The pin material for the testing is Invar which is an alloy composed of 36% nickel and balance iron. The heat transfer properties such as absorptivity and conductivity of the K-type thermocouple and the Invar pin are similar (Howell *et al.*, 2011, Incropera *et al.*, 2007). Provided these assumptions, the temperature reading based on analysis using a numerical model for the thermocouple and the sample temperature on the Invar pin should be similar however offsets can be calculated using the model.

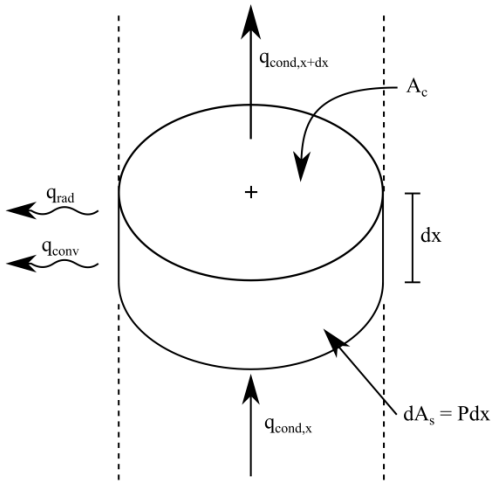

Figure 3.7: An energy balance is performed on a representative volume as seen above to arrive at an equation for the temperature of the pin given conduction and radiation effects (Kiss *et al.*, 2013a).

For a rigorous comparison of the thermocouple and pin temperatures, a numerical model was developed. Following a derivation similar to the temperature distribution in extended surfaces, the energy balance was performed taking into account conduction and radiation in a control volume. Exact solutions exist for extended surfaces for conduction and convection heat transfer however these solutions do not best represent the operating conditions. Given the high operating temperature, radiation is significant and must be considered. Also, since the heater is heating only a section of the pin, a heat flux into the pin can be considered for a region unlike the exact solutions. With these assumptions, a control volume can be drawn as seen in Figure 3.7 with conduction, convection, and radiation heat transfer. With this analysis, the governing equation for this system can be derived as Eq. 3.5 from an energy balance.

$$\frac{d^2T}{dx^2} - \frac{hP}{kA_c}(T - T_\infty) - \frac{\varepsilon\sigma P}{kA_c}(T^4 - T_e^4) = 0 \qquad [3.5]$$

Included in this analysis is the assumption that emissivity, ε, thermal conductivity, k, convective heat transfer coefficient, h, perimeter, P, and cross sectional area, A_c, remain constant. The values for the convective heat transfer coefficient and the emissivity were set to 10 W m^{-2} K^{-1} and 0.45 respectively (Incropera *et al.*, 2007). When solving these equations, convective and radiation heat transfer was assumed at the boundary conditions as seen in Eq. 3.6.

$$-kA_c\frac{dT}{dx} = hA_c(T - T_\infty) + \varepsilon\sigma A_c(T^4 - T_e^4) \qquad [3.6]$$

This boundary condition was used since defining temperatures at the end points wouldn't properly capture the system. The temperature of the thermocouple in the heater was known from the thermocouple output however the temperature away from the heater was unknown. Defining a temperature, such as ambient temperature, at this boundary could affect the temperature

distribution along the pin and increase conductivity effects by increasing the temperature gradient if the end temperature is greater than ambient. Setting the radiation heat transfer boundary condition allows this end to come to equilibrium based on the heat input from the heater and radiation losses to the environment.

In order to model the heater, two environmental temperatures were used: one for removing heat from the pin and one for adding heat. The equipment around the pin was assumed to be at 300 K and effectively removing heat from the pin through radiation. For convection, the surrounding temperature was assumed to be the average of the ambient temperature and maximum pin temperature. In order to simulate the heat addition through the heater, another environmental temperature was assigned. This heater environmental temperature was only exposed to a section of the pin which was dependent on the heater used. For the infra-red heater, the datasheet defined the heating zone as 6.35 mm (0.25 in) whereas the ceramic resistance heater had a uniform temperature distribution and the pin was roughly 17 mm inside the heater. The heater environmental temperature was calibrated based on the thermocouple calibration which controlled the heater power. With a thermocouple of length 152.4 mm (6 in), the heater temperature was set such that the bead temperature matched the calibration temperature. These environmental temperatures could then be used to see how the temperature distribution would change using an Invar pin. The heater temperatures could then be used to find a sample temperature using the Invar pin properties. Table 3.1 shows the values that were used for this analysis.

Table 3.1: Parameters used for studying sample temperature.

	Thermocouple	Invar
Length (m)	0.1524	0.0227
Diameter (m)	0.0010	0.0016
Thermal Conductivity ($W\ m^{-1}\ K^{-1}$)	25.0	13.8

With these changes, small temperature differences could be observed. Using the infra-red heater, the most extreme case when the heater was at the lowest power, calculated a sample temperature of 720 K when the thermocouple read 684 K. This can be expressed as a 5.3% error. The difference between the thermocouple and pin temperature decreases as temperature increases, with a minimum of 2.4%, or 21 K. These offsets were then used in the analysis of the oxidation of the nickel particles to provide the most accurate results. Table 3.2 shows a more detailed analysis for each temperature which was run.

Table 3.2: Comparison of experimental data and numerical results for the infra-red heater.

Power Supply Point (%)	Thermocouple Temperature T_{TC} (K)	Sample Temperature T_{sample} (K)	$T_{sample} - T_{TC}$ (K)	% Error (%)
60	684	720	39	5.3
70	797	830	37	4.1
80	905	935	31	3.3
90	1016	1045	29	2.9
100	1122	1149	21	2.4

From this analysis, a temperature correction is used to account for thermocouple and pin temperature differences. Having addressed this, the largest variation of temperature in the infra-red heater would be attributed to position variation. The temperature variation with position experiences gradients as high as 80 °C with a change of 500 μm. As the sample was heated, the

sample holder needed to move to keep the pin tip in the field of view. Maintaining the pin tip in the field of view was a challenge even with a low thermal expansion material like Invar and the sample could have some time outside of the focal point of the infra-red heater. The time outside of the field of view, and focal point, would be small however for completeness this possibility is mentioned. Also, changing samples meant moving the heater assembly so that the new sample could be installed in the holder. The assembly was on translational stages and the positions on the stages were recorded. However, with the large temperature gradients that were observed, the heater was returned to a same position as best as possible, with precautions taken to minimize any effects from misalignment.

Results

The experimental approach outlined above was successful for oxidizing nickel powder samples using only two of the heaters: the infra-red and ceramic resistance heater. The reaction rates and activation energy values were validated using reported values in the literature. There were some differences between the resulting reaction rates which were calculated using the two heaters. Using the ceramic resistance heater, the reaction rate was slower and the activation energy larger than that using the infra-red heater. Differences in these values can be attributed to changes in experiment including different nickel powders and environmental control.

Experiments were first conducted using the infra-red heater. In Figure 3.8, two transmission images can be seen from the same sample at the Ni K- edge's white line peak for powder in the Ni and NiO forms. As the sample oxidizes, the material expands and the rough edges of the Ni powder appear to smooth out as shown in Figure 3.8b. Particles swell, resulting in the appearance of much larger particle diameters and necks. The interface between the particles also appears to grow, resulting in increased particle contact. An optical density plot of the transmission images is shown in Figure 3.8c. The optical density is normalized by the end points where the sample is known to be in either the Ni or NiO form based off of the XANES spectra. Time t=0 indicates the start of the oxidation process. The oxidation starts off rapid because of the large surface area available. As the core of Ni shrinks, there is less surface area available for Ni oxidation and the distance required for oxidation is increased due to the thicker NiO shell.

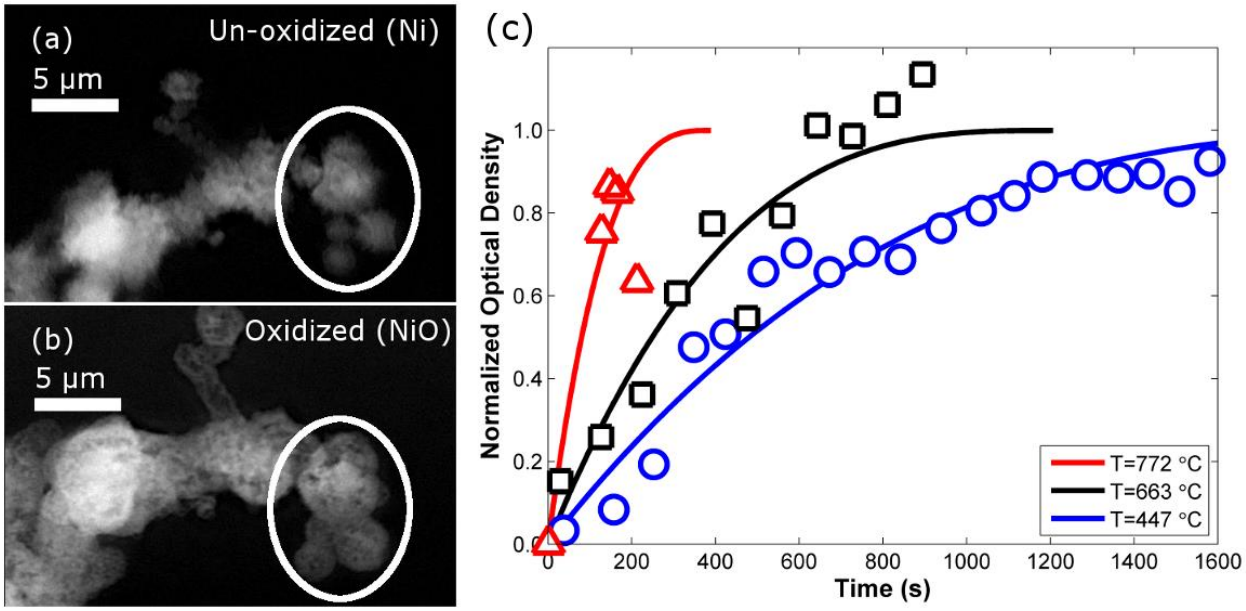

Figure 3.8: Using the infra-red heater, the nickel particles can be seen before (a) and after (b) oxidation. Spherical shaped particles are selected and the volume increase can be seen after oxidation of the particles. (c) The optical density is tracked during the oxidation process for different temperatures (Kiss *et al.*, 2013a).

The experiments were repeated using gas control and the ceramic resistance heater. Using the experimental procedure outlined above, nickel powder spheres were oxidized at several solid oxide fuel cell operating temperatures ranging from roughly 670 to 830 °C. The heater was calibrated using a K-type thermocouple in place of the sample position and was corrected using the pin heat transfer model. Corrected temperatures were used for all of the reaction rate and activation energy calculations.

Performing each trial was a time consuming processes and could exceed 6 hours per trial. It was desired to collect data at more temperatures but there was limited time allocated to access the TXM. Using this controlled gas environment approach, more data points could be collected

per trial due to the image taking process becoming much simpler than with previous heater designs using an IR heater (Kiss *et al.*, 2013a). The sample still moves slightly during the oxidation however it is much easier to keep in the field of view. A steadier sample allows for more images to be taken and more data points collected to look at optical density over time. This is especially important at the beginning of the reaction where the gradient is large. When the numeric model is trying to fit the experimental data, there are more data points to consider which can help the model fit the data more accurately.

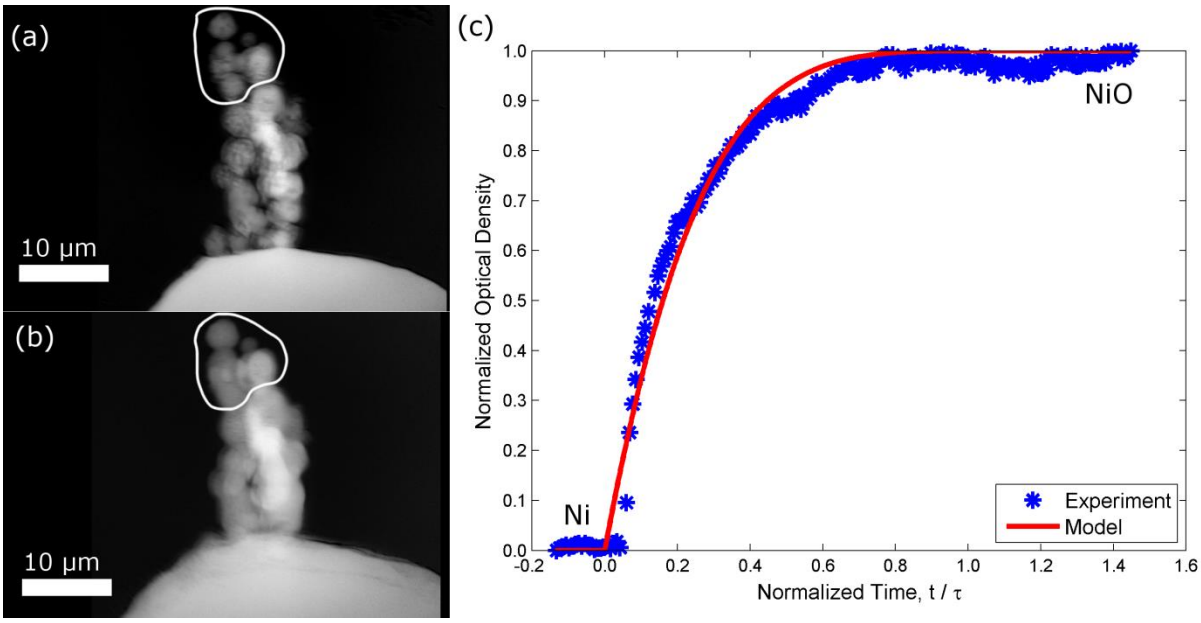

Figure 3.9: The nickel spheres are shown before (a) and after oxidation (b) at 830 °C. The starting spherical geometry makes it easier to select particles to track. (c) The optical density is tracked during the reaction and using the "Averaging" method, significantly more data points can be collected and analyzed.

Overall, the experiments were performed at various temperatures ranging from 400 to 850 °C. The reaction rate was observed to increase with temperature. To extract more information from the data, the reaction rate was fitted to an Arrhenius equation where an activation energy could be calculated from the exponent term of Eq. 3.7.

$$k_c(T) = k_0 \cdot exp\left[\frac{-E_a}{RT}\right] \quad [3.7]$$

A least squares fit was used with the Arrhenius equation to find the reaction constant and the activation energy. Using the infra-red heater, a value of 65 kJ/mol was determined for the activation energy. The data from ceramic resistance heater yielded a higher activation energy of 112 kJ/mol. There is a wide range of values reported for the activation energy of nickel oxidation ranging from 37 to 250 kJ/mol (Atkinson, 1985, Haugsrud, 2003, Modena *et al.*, 2006, Waldbillig *et al.*, 2005). The results of the experiments and modeling can be seen in Figure 3.10 below.

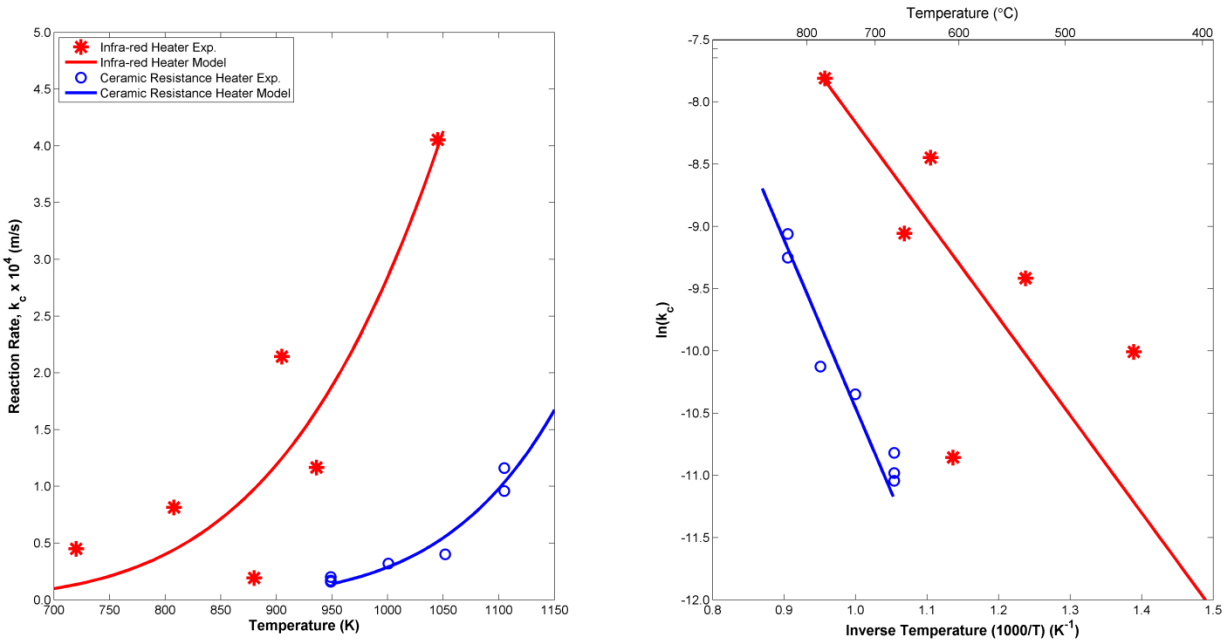

Figure 3.10: A comparison of the reaction rates between the two heaters. In both figures, the infra-red heater is red and the ceramic resistance heater is blue. The symbols are experimental points and the lines are modeling.

Discussion

The kinetic data collected using these setups reveal similar trends but different values. The resulting reaction rate using the ceramic resistance heater is slower than the infra-red heater and the activation energy is higher. There are several factors which contribute to the change in reported values including the heating system and starting sample. Using the infra-red heater, there was no gas environment control. This meant that when the heater was turned on, the reaction started and the imaging began. With the ceramic resistance heater, the gas environment is controlled so that the system is heated to temperature before switching to an oxidizing environment. While this simplified imaging by removing the thermal expansion component, this also could have had effects on the nickel powder. By leaving the sample in an elevated, inert environment, the sample can be annealed which has been shown to affect oxidation (Haugsrud, 2003). The heat treating can change the grain size and since grain boundary diffusion is a major transport path, the oxidation could be affected.

Another major contributor can be the change in starting nickel powder. With this work, nickel spheres were utilized which provided a simple geometry to study, while powder used in the infra-red heater was amorphous in shape. The change in starting powder made the image processing easier and could model the oxidation process more accurately. The surface roughness and shape may affect the oxidation rate (Haugsrud, 2003). The manufacturing techniques used to produce these powders may have left a material with different material properties such as grain size.

The two heaters also heat the sample using different approaches. The infra-red heater focuses the infra-red radiation from a 250 W bulb down to a spot size so that it can heat the sample. Outside that spot, the temperature drops significantly since the radiation will not be

hitting the sample. With the ceramic resistance heater, the sample is still heated using radiation however it is not focused down to a single spot. The heater is capable of maintaining a uniform temperature field around the field of view. This is largely due to the spiral heating element which can uniformly heat a column where the sample will be located. Also, there better management of the heat and the heater is capable of higher temperatures while providing less energy. To reach 830 °C, approximately the maximum temperature for the infra-red heater, the ceramic resistance heater used about 100 W of input power.

By controlling the gas environment, there is the ability to study many different reactions. While this work focused on nickel oxidation, it can also be used for nickel oxide reduction. This was demonstrated using this system, however there was not enough data to report anything significant about nickel oxide reduction. After nickel oxidation had been imaged, the gas environment was switched to an inert environment. Once purged, a 4% hydrogen/balance helium gas (Airgas) was fed around the nickel oxide sample to reduce it back to its original nitrogen state. While the reduction step was successful, it was difficult to keep track of the sample since there were significant morphological changes and the sample was no longer spherical in shape. This complicated the data processing and unfortunately was unable to provide valid data to report in this study.

Before Oxidation | After Oxidation | After Reduction

Figure 3.11: Absorption images of a sample being oxidized and then reduced. During oxidation, the spheres begin to change shape and individual particles bond together. This is tolerable for the oxidation reaction but during reduction, the morphology change is too significant to study assuming spheres.

Conclusions and Scientific Impact

Researchers are investigating degradation effects in SOFC anodes in order to help extend the lifetime of the devices. These anodes are typically made of nickel and YSZ, and can degrade due to oxidation of the nickel particles. The oxidation will increase the volume of the nickel, increasing stresses between the phases which can lead to cracks and failure. In order to minimize degradation from this mechanism, it is important to understand and have an accurate representation of the kinetics. Several research groups have focused on nickel oxidation kinetics and there is a significant spread of reaction rate and activation energy data presented in the literature. Previously used techniques are not capable of observing the reaction at the nanoscale while it is occurring and calculating reaction rates. In order to accomplish this, a new setup using a synchrotron based TXM with temperature and environmental control is developed.

Developing a system which was capable of operating in the limited working distance of the TXM at SOFC temperatures is not a trivial task. Several heater designs were considered and success was achieved with two of them. The infra-red heater design was capable of oxidizing nickel particles in ambient air. The gas environment was not controlled with these experiments but images were able to successfully capture the reaction and calculate reaction rates as a function of temperature. For easier temperature control and the addition of gas control, a heater design using a ceramic resistance heater. Using this setup, the sample could be heated in an inert environment and more images could be captured during the reaction. Reaction rates were computed but were lower than those measured using the infra-red heater. The difference in the reaction rate can be attributed to several factors including using a different nickel powder sample and allowing the sample to reach thermal equilibrium in an inert environment before oxidation began.

Using the approach outlined above, *in situ* observation of nickel powder chemical reactions has been imaged and used to calculate reaction rates and activation energies. The work completed so far has been a validation of the technique and a building block towards more complex experiments. With the setup designed by this research, users will be able to study high temperature chemical reactions and observe the changes to the microstructure *in situ*. This approach is not limited to solid oxide fuel cell applications and can be modified to heaters with lower operating temperatures and will still be effective at controlling the temperature and gas environment. While several research teams have developed elevated temperature systems to study chemical reactions in a TXM, this work has overcome the challenges associated with a limited working distance and accomplished significantly higher operating temperatures.

Chapter 4: Waste form Samples

Introduction

Given the success of the *in situ* nickel oxidation experiments, the experimental approach can be modified for new applications and materials. Through a collaboration with Prof. Kyle S. Brinkman at Clemson, a study was started on waste form materials. Previously, *ex situ* techniques were used to study the materials. Similar to the nickel oxidation setup, the temperature and gas composition around the waste form sample can be controlled while the transmission X-ray microscope (TXM) is imaging changes in the morphology. A different microscope will be used which can operate at lower energy levels to target different absorption edges. New components will need to be considered in order to meet the requirements of the experiment and microscope.

Nuclear waste forms are materials used in nuclear waste treatment and storage. These materials should be able to contain high levels of transition metals such as molybdenum and cesium. Cesium is especially difficult given its ability to transport through materials, volatility at high temperatures, and ability to form water soluble products. As a way to contain cesium, researchers have been investigating a ground of minerals known as hollandite (Amoroso *et al.*, 2014). These materials have locations where the cesium cations can become immobilized in the structure. One possible hollandite form with the composition $Ba_{1.0}Cs_{0.3}Cr_{1.0}Al_{0.3}Fe_{1.0}Ti_{5.7}O_{16}$ was considered for studying in the TXM. With this composition, testing has shown the presence of a TiO_2 minor phase (Amoroso *et al.*, 2014). Using the TXM and scanning across different absorption edges, different elemental phases can be identified and the morphology reconstructed. This will be able to identify if any minor phases are being formed.

One of the previously used durability tests for this material exposes the sample to a high temperature, high humidity environment. This setup tested the waste form samples using the ASTM designation C1663-09 procedure. This approach involves suspending the sample from a platinum wire and exposing the sample to a controlled temperature and humidity environment. The environmental chamber is a high pressure container which can be heated to create high vapor pressures. The desired temperatures are typically 200 to 300 °C and the humidity in this environment is fully saturated. The sample, being exposed to these conditions, can be studied before and after exposure to see how the microstructure has evolved. This is an *ex situ* technique and can only provide information at certain time stamps. It would be useful to be able to observe the microstructure evolving *in situ* to have a better understanding of the changes.

Experimental Approach

In order to adapt the *in situ* oxidation setup for these high humidity tests, some changes needed to be considered. These experiments will be performed at the Stanford Synchrotron Radiation Lightsource (SSRL) beamline 6-2C where there is a significant working distance between the pin hole and the zone plate. The scientists have been able to design and manufacture a metal wire resistance heater with a large heating volume which can be used within the desired temperature range of 200 to 300 °C. Details on this heater were explained in the previous chapter under "SSRL Heaters".

Since titanium minor phases could be forming, the titanium K-absorption edge was targeted at (4966 eV). It is important to consider how the components will behave at this energy. With the nickel oxidation experiments, quartz capillary tubes were used to help isolate the sample from the ambient. When running the X-rays at this energy level, the quartz will attenuate a significant fraction of the signal so another material is needed. The experiments are not operating at the high temperatures that the nickel oxidation requires, and therefore Kapton (DuPont, Wilmington, DE) tubing can be used. The Kapton attenuates less signal at the titanium edge than the quartz capillary would and can withstand the elevated temperatures. Kapton tubes were purchased from Cole Parmer (Vernon Hills, IL), to have an outside diameter of 1.9 mm (0.075 inch) and wall thickness of 0.05 mm (0.002 inch). The wall thickness is thicker than the quartz capillary tubes but at this energy level, the overall attenuation should be less than using the quartz capillary tubes.

While at the titanium K-edge, the X-rays are scattered by the air and extra precautions need to be taken to minimize signal loss. A curtain is draped around the optics and helium is fed into the microscope enclosure. This reduces the attenuation of the X-rays due to scattering. Also,

when operating at the titanium K-edge, the efficiency of the optics starts to decrease. This causes less signal to reach the CCD. The combined losses associated with the scattering and efficiency losses increase the exposure time needed for each image. While at the iron K-absorption edge at 7112 eV, the exposure time for a projection image was 1 second. When the monochromator was set to the titanium K-edge, the exposure time needed to be increased to 30 seconds. Unfortunately, when focusing the X-rays onto the CCD, the zone plate needs to move closer to the sample. This decreases the working distance such that the heater cannot be used while accessing the titanium K-edge. This restriction limits imaging of any titanium phases to *ex situ* testing after the heater has been removed. Instead, the *in situ* imaging will target the iron K-edge at 7112 eV where the working distance will accommodate the heater.

The waste form samples were prepared before arriving at the beamline and were on the tip of an alumina pin. A 20 μm diameter cylinder was milled using a focused ion beam from the stock material and secured to the tip of the pin using a platinum weld, similar to the procedure explained by Lombardo *et al.* (Lombardo *et al.*, 2012). The pins were held in the microscope using the sample pin holders used in the nickel oxidation experiments. Modifications were made to shorten the length of the shaft for location on the microscope stages and for gas delivery with the Kapton tubing.

In order to prevent damage to the microscope stages, the standard adapter used to hold the sample holder was modified. The new adapter was made out of titanium 6AL-AV alloy for its low thermal conductivity. This will prevent heat from conducting through the adapter and heating the sample stages. The new adapter was also made thinner so that the sample could be held in the field of view and there was a greater distance between optics and the stage. With the

stages lowered, there would be more room for the gas delivery tubing to rotate and avoid hitting the pin hole and zone plate.

In order to control the gas environment around the sample, nitrogen gas was used as a carrier gas for the water vapor. A humidification system was borrowed from Prof. Pasaogullari which was capable of controlling the water vapor by using a bubble humidifier. This is similar to what is used and described in the water flux experimental setup. The humidification system (Fuel Cell Technologies Humidification System, Albuquerque, NM) uses two 316 stainless steel humidity bottles which hold the deionized water. When the gas is fed into the humidity bottle, it travels through a Nafion tube so that water can start saturating the gas stream. Float switches maintain a constant water level in the humidifier and temperature controllers maintain the water bath and gas exhaust temperatures. There are also solenoids in place to bypass the humidifiers.

The humidification system can be manually or remotely controlled using software. The temperature controllers can be accessed using an RS-485 connection and the LoveLnkIII software. This allows for setting and monitoring the temperatures in the setup. There is also a USB connection to control a LabJack U-12 board. This board is used to control the solenoids to bypass the humidifiers. There was no software received for this so a free version of DAQFactory was used to control the bypass solenoids. It should also be noted that the solenoids should not be left on for more than one hour because they will start to heat up.

Using the humidification system, it was not possible to heat the humidifiers in excess of 100 °C to get the high water vapor pressures described in the ASTM procedure. It is more realistic to heat the water bath to 80 °C and run heated tubing at 100 °C to prevent any condensation in the lines. The saturation pressure of water at 80 °C is 80 kPa. This value increased to 397 kPa when considering water vapor at 250 °C (Moran & Sharpiro, 2008).

Although this is not achieving the high relative humidity environment that is desired in the original procedure, the system is only operating at ambient pressure and is creating an environment with a high mole fraction of water.

To prevent any condensation in the gas lines from the humidifier to the sample, a heated line needed to be developed. While several ideas were explored, two were actually built for testing. The first system involved external heating. This meant that 0.250 inch outer diameter Teflon tubing was fed through a copper sleeve and then wrapped in heat tape. Fiber glass insulation and aluminum foil were then wrapped around the heat tape to help insulate the heated line. The heat tape was controlled by feedback of a K-type thermocouple which was located between the tubing and the copper sleeve. A Sorenson DC power supply (DLM 80-7.5, AMETEK, San Diego, CA) was used to power the heat tape. While this system worked well during trial runs outside the microscope, it was too large and stiff to be used inside the microscope. Once all of the layers were wrapped around the tubing, it was difficult to bend the tubing and could come into contact with the optics.

Given the complications with external heating, an internal heating method was designed. Instead of heating the outside of the tubing, a Ni-Cr wire was fed through some Teflon tubing to provide the heat. Stainless steel Swagelok fittings were used as electrodes for the Ni-Cr wire. The Ni-Cr was spot welded to the fittings and the fittings could then be connected to a power supply to heat the tubing. A plastic sleeve was used to insulate the outside of the tubing. Even with the smaller form factor, the Swagelok fittings were too large and the sample would not be able to rotate while the gas line was hooked up.

The testing procedure closely followed the nickel oxidation procedure. Before the *in situ* testing could begin, the water bath in the humidifier was set to 80 °C and allowed to reach steady

state which took about 1.5 hours. The sample pin was installed in the pin holder and the Kapton tube was placed over it to isolate the sample from the ambient. The solenoids in the humidification system were set to bypass the humidifier. Nitrogen gas was run through the system to purge the environment. The monochromator was set to the iron K-edge and the sample was moved to be in the field of view. The heater was set to 250 °C and allowed to reach thermal equilibrium. During this time, the sample was tracked to stay in the field of view. Once the system achieved steady state, the solenoid was switched off, allowing the nitrogen gas to flow through the humidifier. Images were collected to observe any changes in the microstructure of the sample.

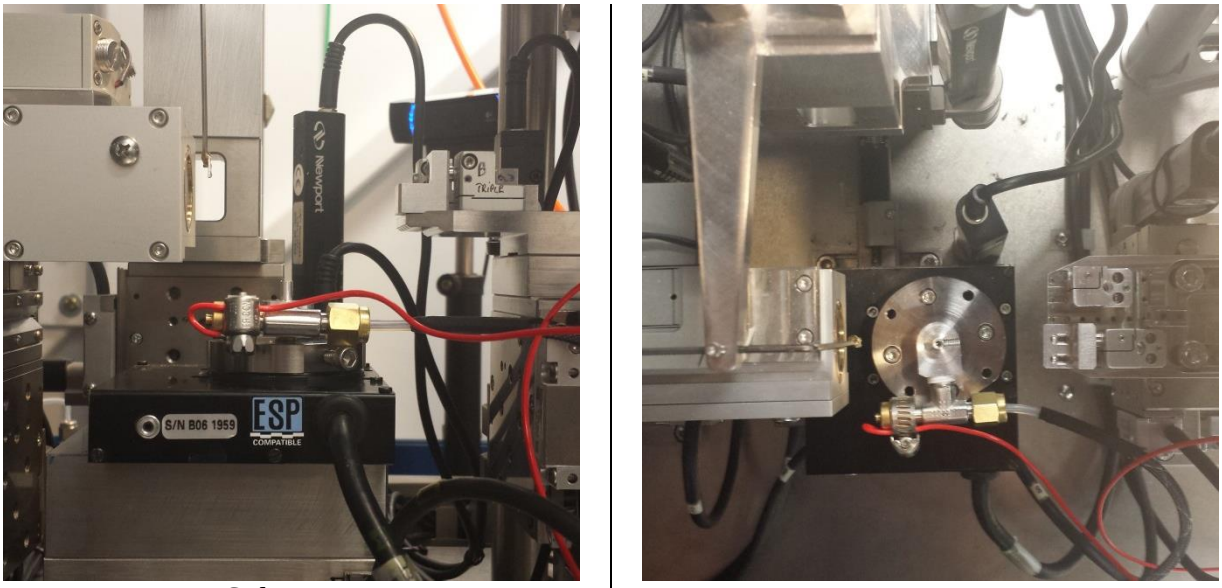

Side View | Top View

Figure 4.1: Side and top views of the gas delivery, electrical connections, and sample holder in the microscope. The environmental control needed to be carefully operated to not interfere with the surrounding X-ray optics.

Complications

During the *in situ* testing, some complications arose which quickly halted the experiment. While imaging the sample, water droplets could be seen forming on the Kapton tubing and around the sample. Having liquid droplets forming around the sample is undesirable and indicates that there are some problems in the experimental setup. All of the feedback indicators seemed to be displaying the desired values so the system was shutdown to investigate why liquid water was present around the sample.

Upon further investigation, it was noticed that the cause of the problem was most likely the aluminum sample pin holder. A significant amount of water was found inside of the sample holder and when enough water collected, was squirting up into the Kapton tube and onto the sample. Aluminum has a high thermal conductivity and the holder temperature must have been dropping below the saturation temperature of the incoming gas at 80 °C. This would cause the water to condense inside of the holder until it was forced into the Kapton tube. The holder was not heated to avoid any heat getting to the sample stages and damaging them.

In fear of damaging the microscope and stages due to water, the *in situ* testing was cancelled. While this was a significant issue, there were other complications which limited the *in situ* testing with this microscope. It was decided that the internal heating method was the best option to prevent condensation in the gas line and provide a flexible, compact, heated gas line. Even though this was the most compact solution, the tubing was still too large and stiff for performing tomographies. It was possible that the tubing would come in contact with the pin hole and it was decided not to rotate the sample with the gas delivery hooked up. In addition, since the minor phase of interest was TiO_2 it was desirable to operate at the titanium absorption edge. This was not possible due to working distance limitations of the TXM and the large size of the heater.

Assuming images could be taken at the titanium absorption edge, it would have been difficult to process the data given the long exposure times required and the helium curtain.

Conclusions

The original goal of this experiment was to investigate morphological and chemical changes in a nuclear waste form material and identify the formation of minor phases. An experimental setup was developed based on a proven approach for studying *in situ* nickel oxidation in a synchrotron based TXM. Nitrogen was passed through a humidifier system to provide a high concentration of water vapor around the sample. A heater maintained the sample at the desired temperature of 250 °C while the sample was imaged at the iron K-absorption edge. Unfortunately, there were complications and water was found condensing in the sample pin holder. This decreased the water partial pressure and caused liquid water droplets to appear around the sample. To prevent damaging the microscope, the testing was cancelled to evaluate this issue.

While this experience did not yield any useful results for the scientific community, this beamline trip did present itself as a useful experience. There was a great deal of collaboration with the beamline scientists before attending this trip including weekly conference calls and emails. With the challenges that were encountered during this trip, a new setup can be designed with these issues in mind. As with the *in situ* nickel oxidation setup, this approach needs to evolve and improve the experimental setup to arrive at working solution. This was a first attempt at *in situ* experiments with these waste samples and hopefully revisions to the experimental setup will be made to produce useful data.

Chapter 5: Conclusions

Fuel cell systems are a viable option for different energy applications. These systems are capable of achieving high efficiencies and can be utilized in both portable and stationary power applications. It is common for low temperature fuel cells such as polymer electrolyte fuel cells to be utilized in portable power applications while higher temperature fuel cells like solid oxide fuel cells are considered for stationary power applications. When considering the different challenges that can impede the progress of these devices, transport losses are one of the issues which should be addressed to improve these devices.

Alkaline anion exchange membrane fuel cells are one technology which is being considered for portable power applications. While these fuel cells can operate without platinum based catalysts and utilize alcohol based fuels, mass transport is a major limitation affecting the performance. The alkaline anion exchange membranes (AEMs) which are used do not have a high ionic conductivity when compared to their acidic counterparts the proton exchange membrane. By understanding the chemistry and transport in the AEM, new membranes can be designed and manufactured which can consider these limitations and hopefully improve the ionic conductivity of the membrane.

In contrast, solid oxide fuel cells (SOFCs) are used for stationary power applications and are able to achieve satisfactory ionic conductivity in the solid electrolyte. Research has been focused on improving the lifetime of these devices and has been considering degradation losses in the Ni/YSZ anode. During operation, the electronic conductor, nickel, can oxidize forming nickel oxide (NiO). This reaction decreases the electronic conductivity and also causes morphological changes in the anode. The oxidation reaction can cause a significant volume increase in the nickel which will increase stresses between solid phases. It is possible that the

increased stresses can initiate cracks, increasing the path length for electrons. If the cracks form at the anode-electrolyte interface then significant transport losses and failure of the cell can be observed. Understanding and minimizing the effect of nickel oxidation in Ni/YSZ anodes is important for extending the life of these devices.

Scientific Impact

As mentioned above, there are considerable losses associated with the alkaline anion exchange membrane. In order to understand ion transport in these membranes, it is important to understand water transport since membrane properties are strongly dependent on the hydration. In order to study water transport a permeation based water flux experiment was built and validated by testing a popular and well-studied proton exchange membrane, Nafion 117 PEM. Once validated, Snowpure Excellion I-200 AEM was studied and water flux measurements were taken.

A numeric model simulating the conditions in the water flux experiment labeled the MP09 was developed to solve for effective water-membrane diffusion coefficients as a function of local hydration and temperature. The diffusion coefficients extracted from this model were then scaled using principles from kinetic theory to predict effective ion-membrane diffusion coefficients as functions of hydration and temperature in the membrane. This technique can be used to predict ion transport for different mobile species including hydroxide, carbonate, and bicarbonate.

Using the predicted ion-membrane diffusion coefficients, the ionic conductivity of the membrane can be calculated. The ionic conductivity equation is derived from the dusty fluid model and Ohm's law and can be used to predict the ionic conductivity of the membrane in different ionic forms as functions of hydration and temperature. Using this conductivity equation in combination with experimental data, the equilibrium constants for different ionic species can be calculated to solve the dissociated ion concentrations. As the fraction of dissociated ions increases, more ions are available for transport and the ionic conductivity of the membrane will increase.

Using this approach as a way to test and characterize different membranes. By considering the water transport in an AEM, the ion transport and membrane performance can be predicted. When developing new AEMs, the data extracted using this approach can be used to consider different polymer backbone and fixed side chain group combinations to improve ionic conductivity.

In SOFC Ni/YSZ anodes, the oxidation of nickel has been shown to decrease performance and by studying how this reaction occurs, the transport losses can be predicted. Since the three-dimensional morphology is complicated within a Ni/YSZ anode, the system is simplified to start with nickel oxidation experiments. Looking to the literature, there is a large range in reaction rates for nickel oxidation which first needs to be understood before moving to more complicated systems.

Using a transmission X-ray microscope (TXM) and environmental chamber, nickel oxidation can be observed *in situ* and the nanoscale features imaged while measuring reaction rates. X-ray absorption near-edge structure (XANES) is used to confirm complete conversion from nickel to nickel oxide. The development of this setup demonstrates a new technique to study chemical reactions at the nanoscale and SOFC operating conditions using a TXM. Using the data collected from this experimental setup, the reaction rate for nickel oxidation was calculated as a function of temperature as well as the activation energy for the reaction.

Recommendations

The water flux experiment was successful in measuring water flux across fuel cell membranes and providing the necessary information to predict diffusion coefficients, ionic conductivity, and ion dissociation. If more time and resources were available for the experimental setup, then some suggestions could be made to benefit the scientific community.

While a significant effort was made, the water flux experiment was unsuccessful in confirming negligible interface resistances in AEMs. Membranes were manufactured to different thicknesses specifically for this purpose however there were issues with membrane stability and sealing the membrane in the flow channels. Given the interest in the proton exchange membrane community with interface effects and the questions received at conferences, there needs to be some sort of manuscript which addresses this issue for AEMs. Since AEMs have diffusion coefficients about an order of magnitude less than PEMs, the interface effects may not be as significant but this should be investigated.

This water flux experiment was able to measure water flux for one AEM however many AEMs are available from different research groups. These membranes are produced by different manufacturing processes including solution casting, electrospinning, and radiation grafting. There are also different combinations of polymer backbone and fixed ion group chemistries which are being investigated. AEMs are still in the developmental stage and this experimental procedure can be used to characterize water and ion transport in these membranes to help arrive at ideal membrane chemistries for maximizing ion dissociation and ionic conductivity.

The nickel oxidation experiments were able to successfully measure reaction rates and an activation energy using a new technique. Controlling the gas and temperature environment around a sample inside the working distance of a TXM is not trivial. The methods outlined in

this thesis demonstrated the ability to image nickel oxidation, and with limited success nickel oxide reduction.

This work was focused on degradation in Ni/YSZ anodes and needs to eventually develop to study these anodes within the TXM. In order to reach this goal, a complete set of reaction rates should be measured using this approach. Nickel oxidation has already been measured but nickel oxide reduction experiments should be performed to demonstrate the capabilities and confirm the values in the literature. Reduction was performed however problems arose with coarsening and the particle morphology changing too much. If spherical nickel oxide (NiO) particles are available, these would provide an ideal starting point for studying nickel oxide reduction and can be easily modeled using the developed tools.

Two-dimensional images were utilized to study the nickel oxidation reactions. This is acceptable when the geometry of the particles is known and can be assumed to be spheres. When considering the complex microstructure of a Ni/YSZ anode, a tomography is necessary to see any changes. Tomographies can be taken before and after oxidation but that is not an *in situ* technique. It may be difficult, but high speed tomographies have been conducted using X-ray computed microtomography (Beckmann *et al.*, 2007). In order to use this approach work, the exposure time for each image needs to be extremely short and the stages need to move quickly. *In situ* tomographies might not be currently available with TXMs for nanotomography however this should continue to be investigated since it will be extremely valuable to the scientific community.

The *in situ* experimental approach should not be limited to only studying nickel oxidation and reduction experiments. SOFCs are not limited to degradation by these reactions and poisoning can occur from other sources such as sulfur and chromium. It may be difficult to

control the gas environment, and exhaust gas, when dealing with these gases but studying these poisoning mechanisms will benefit researchers in this field. Using the TXM, the location of the poisoning and the reaction front could be imaged and reconstructed in three-dimensions.

While considering new reactions to study using the nickel oxidation setup, it is important to remember other useful materials which can benefit from an *in situ* technique such as this. The waste form material is one example of a material which can benefit from the high resolution and elemental sensitivity of a synchrotron based TXM. Other energy materials found in supercapacitors, solar cells, or batteries might also benefit from a temperature and gas controlled environment to study chemical and morphological changes.

To improve on the experimental setup, it would be useful to design a sample holder with slip rings or rotary unions. Using a rotary union, the gas inlet for the sample could remain at one location, where it won't interfere with the X-ray optics while the sample can rotate. This would simply the setup and make it easier to perform tomographies in the TXM. For the waste form sample experiments, problems arose when water condensed in the sample holder. One way to avoid this is to heat the sample holder. This requires careful consideration to contain the heat away from the sample stages. With the amount of water found in the sample holder there needs to be a change in the sample holder design to properly test the nuclear waste samples.

References

Amoroso, J., Marra, J., Conradson, S.D., Tang, M. & Brinkman, K. (2014). Melt processed single phase hollandite waste forms for nuclear waste immobilization: Ba1.0Cs0.3A2.3Ti5.7O16; A = Cr, Fe, Al. *J. Alloys Compounds* **584**, 590-599.

Arges, C.G. & Ramani, V. (2013). Investigation of cation degradation in anion exchange membranes using multi-dimensional NMR spectroscopy. *J. Electrochem. Soc.* **160**, F1006-F1021.

Arges, C.G. & Ramani, V. (2012). Alkaline stability and ion conductivity of polysulfone anion exchange membranes (AEMs) with different cation chemistries. *ECS Trans.* 50 (**2**), pp. 2183-2197.

Arges, C.G., Parrondo, J., Johnson, G., Nadhan, A. & Ramani, V. (2012). Assessing the influence of different cation chemistries on ionic conductivity and alkaline stability of anion exchange membranes. *Journal of Materials Chemistry* **22**, 3733-3744.

Atkinson, A. (1985). Transport processes during the growth of oxide films at elevated temperature. *Rev. Mod. Phys.* **57**, 437-470.

Atkinson, A. & Taylor, R.I. (1978). The self-diffusion of Ni in NiO and its relevance to the oxidation of Ni. *J. Mater. Sci.* **13**, 427-432.

Atkinson, A., Taylor, R.I. & Goode, P.D. (1979). Transport Processes in the Oxidation of Ni Studied Using Tracers in Growing NiO Scales. *Oxid. Met.* **13**, 519-543.

Ayeb, A., Otten, W.M., Mank, A.J.G. & Notten, P.H.L. (2006). The hydrogen evolution and oxidation kinetics during overdischarging of sealed nickel-metal hydride batteries. *J. Electrochem. Soc.* **153**, 2055-65.

Beckmann, F., Grupp, R., Haibel, A., Huppmann, M., Nöthe, M., Pyzalla, A., Reimers, W., Schreyer, A. & Zettler, R. (2007). In-situ synchrotron X-ray microtomography studies of microstructure and damage evolution in engineering materials. *Advanced Engineering Materials* **9**, 939-950.

Bird, R.B., Stewart, W.E. & Lightfoot, E.N. (2007). *Transport Phenomena.* New York, John Wiley & Sons, Inc.

Bockris, J.O. & Reddy, A.K.N. (1970). *Modern Electrochemistry.* New York, Plenum Press.

Brunauer, S., Emmett, P.H. & Teller, E. (1938). *J. Am. Chem. So.* **60**.

Carter, R.E. (1961). Kinetic Model for Solid-State Reactions. *J. Chem. Phys.* **34**, 2010-2015.

Caulk, D.A., Brenner, A.M. & Clapham, S.M. (2012). A steady permeation method for measuring water transport properties of fuel cell membranes. *J. Electrochem. Soc.* **159**, F518-F529.

Choi, P., Jalani, N.H. & Datta, R. (2005). Thermodynamics and proton transport in Nafion II. Proton diffusion mechanisms and conductivity. *J. Electrochem. Soc.* **152**, E123-E130.

Cocco, A.P., Nelson, G.J., Harris, W.M., Nakajo, A., Myles, T.D., Kiss, A.M., Lombardo, J.J. & Chiu, W.K.S. (2013). Three-dimensional microstructural imaging methods for energy materials. *Physical Chemistry Chemical Physics* **15**, 16377-16407.

Danks, T.N., Slade, R.C.T. & Varcoe, J.R. (2003). Alkaline anion-exchange radiation-grafted membranes for possible electrochemical application in fuel cells. *Journal of Materials Chemistry* **13**, 712-721.

Faes, A., Hessler-Wyser, A., Zryd, A. & Van herle, J. (2012). A Review of RedOx Cycling of Solid Oxide Fuel Cells Anode. *Membranes* **2**, 585-664.

Faes, A., Wuillemin, Z., Tanasini, P., Accardo, N., Modena, S., Schindler, H.J., Cantoni, M., Lübbe, H., Diethelm, S., Hessler-Wyser, A. & Van herle, J. (2011). Design of experiment approach applied to reducing and oxidizing tolerance of anode supported solid oxide fuel cell. Part II: Electrical, electrochemical and microstructural characterization of tape-cast cells. *J. Power Sources* **196**, 8909-8917.

Figliola, R.S. & Beasley, D.E. (2006). *Theory and design for mechanical measurements.* Hoboken, N.J, John Wiley.

Fukuta, K., Inoue, H., Watanabe, S. & Yanagi, H. (2009). In-situ observation of CO2 through the self-purging in alkaline membrane fuel cell (AMFC). *ECS Trans.* **19**, 23-27.

Ge, S., Li, X., Yi, B. & Hsing, I.M. (2005). Absorption, desorption, and transport of water in polymer electrolyte membranes for fuel cells. *J. Electrochem. Soc.* **152**, A1149-A1157.

Green, D.W. & Perry, R., H. (2008). *Perry's Chemical Engineers' Handbook.* New York, McGraw-Hill.

Grew, K.N. & Chiu, W.K.S. (2010). A Dusty Fluid Model for Predicting Hydroxyl Anion Conductivity in Alkaline Anion Exchange Membranes. *J. Electrochem. Soc.* **157**, 327-37.

Grew, K.N., Chu, D. & Chiu, W.K.S. (2010). Ionic Equilibrium and Transport in the Alkaline Anion Exchange Membrane. *J. Electrochem. Soc.* **157**, 1024-32.

Grew, K.N., Ren, X. & Chu, D. (2011). Effects of temperature and carbon dioxide on anion exchange membrane conductivity. *Electrochem. Solid-State Lett.* **14**, B127-B131.

Hallinan, D.T., J. & Elabd, Y.A. (2009). Diffusion of water in Nafion using time-resolved Fourier transform infrared-attenuated total reflectance spectroscopy. *J Phys Chem B* **113**, 4257-66.

Haugsrud, R. (2003). On the high-temperature oxidation of nickel. *Corros. Sci.* **45**, 211-35.

Helfferich, F. (1962). *Ion Exchange.* New York, McGraw-Hill Book Company, Inc.

Hinatsu, J.T., Mizuhata, M. & Takenaka, H. (1994). Water uptake of perfluorosulfonic acid membranes from liquid water and water vapor. *J. Electrochem. Soc.* **141**, 1493-1498.

Howell, J.R., Siegel, R. & Mengüc, M.P. (2011). *Thermal radiation heat transfer*. Boca Raton, Fla, CRC Press.

Hsu, W.Y. & Gierke, T.D. (1982). Elastic theory for ionic clustering in perfluorinated ionomers. *Macromolecules* **15**, 101-105.

Inamdar, A.I., Kim, Y., Pawar, S.M., Kim, J.H., Im, H. & Kim, H. (2011). Chemically grown, porous, nickel oxide thin-film for electrochemical supercapacitors. *J. Power Sources* **196**, 2393-2397.

Incropera, F.P., DeWitt, D.P., Bergman, T.L. & Lavine, A.S. (2007). *Fundamentals of heat and mass transfer*. Hoboken, NJ, John Wiley.

Jeangros, Q., Faes, A., Wagner, J.B., Hansen, T.W., Aschauer, U., Van herle, J., Hessler-Wyser, A. & Dunin-Borkowski, R.E. (2010). In situ redox cycle of a nickel–YSZ fuel cell anode in an environmental transmission electron microscope. *Acta Materialia* **58**, 4578-4589.

Kameda, Y., Sasaki, M., Hino, S., Amo, Y. & Usuki, T. (2006). Neutron diffraction study on the hydration structure of carbonate ion by means of 12C/13C isotopic substitution method. *Physica B* **385-386**, 279-281.

Karmhag, R., Niklasson, G.A. & Nygren, M. (1999). Oxidation kinetics of small nickel particles. *J. Appl. Phys.* **85**, 1186-1186.

Kiss, A.M., Harris, W.M., Wang, S., Vila-Comamala, J., Deriy, A. & Chiu, W.K.S. (2013a). In-situ observation of nickel oxidation using synchrotron based full-field transmission X-ray microscopy. *Appl. Phys. Lett.* **102**, 053902.

Kiss, A.M., Myles, T.D., Grew, K.N., Peracchio, A.A., Nelson, G.J. & Chiu, W.K.S. (2013b). Carbonate and bicarbonate ion transport in alkaline anion exchange membranes. *J. Electrochem. Soc.* **160**, F994-F999.

Klemensø, T., Appel, C.C. & Mogensen, M. (2006). In situ observations of microstructural changes in SOFC anodes during redox cycling. *Electrochem. Solid-State Lett.* **9**, A403-A407.

Kofstad, P. (1966). *High-Temperature Oxidation of Metals.* New York, John Wiley & Sons, Inc.

Larminie, J. & Dicks, A. (2003). *Fuel Cell Systems Explained.* West Sussex, John Wiley & Sons.

Laurencin, J., Delette, G., Morel, B., Lefebvre-Joud, F. & Dupeux, M. (2009). Solid Oxide Fuel Cells damage mechanisms due to Ni-YSZ re-oxidation: Case of the Anode Supported Cell. *J. Power Sources* **192**, 344-352.

Leung, K., Nielsen, I.M.B. & Kurtz, I. (2007). Ab initio molecular dynamics study of carbon dioxide and bicarbonate hydration and the nucleophilic attack of hydroxide on CO2. *J. Phys. Chem. B* **111**, 4453-4459.

Levenspiel, O. (1972). *Chemical Reaction Engineering, Second Edition.* New York, Wiley.

Liu, Y., Nelson, J., Holzner, C., Andrews, J.C. & Pianetta, P. (2013). Recent advances in synchrotron-based hard x-ray phase contrast imaging. *J. Phys. D* **46**, 494001.

Liu, Y., Meirer, F., Williams, P.A., Wang, J., Andrews, J.C. & Pianetta, P. (2012). TXM-Wizard: A program for advanced data collection and evaluation in full-field transmission X-ray microscopy. *J. Synchrotron Radiat.* **19**, 281-287.

Lombardo, J.J., Ristau, R.A., Harris, W.M. & Chiu, W.K.S. (2012). Focused ion beam preparation of samples for X-ray nanotomography. *Journal of Synchrotron Radiation* **19**, 789-796.

Majsztrik, P.W., Satterfield, M.B., Bocarsly, A.B. & Benziger, J.B. (2007). Water sorption, desorption and transport in Nafion membranes. *J. Membr. Sci.* **301**, 93-106.

Marx, D. (2006). Proton transfer 200 years after Von Grotthuss: Insights from ab initio simulations. *Chem. Phys. Chem.* **7**, 1849-1870.

Mason, E.A. & Malinauskas, A.P. (1983). *Gas Transport in Porous Media: The Dusty-Gas Model.* New York, Elsevier Science Publishing Company.

Matsui, Y., Saito, M., Tasaka, A. & Inaba, M. (2010). Influence of carbon dioxide on the performance of anion-exchange membrane fuel cells. *ECS Trans.* 25, 105-110.

Mbuna, J., Takayanagi, T., Oshima, M. & Motomizu, S. (2004). An investigation of weak ion association equilibria between inorganic anions and tetraalkylammonium ions in ethanol-aqueous media using capillary zone electrophoresis. *Bull. Chem. Soc. Jpn.* **77**, 1465-1473.

Meher, S.K., Justin, P. & Rao, G.R. (2010). Pine-cone morphology and pseudocapacitive behavior of nanoporous nickel oxide. *Electrochim. Acta* **55**, 8388-8396.

Mench, M. (2008). *Fuel cell engines.* Hoboken, N.J, John Wiley & Sons.

Merle, G., Wessling, M. & Nijmeijer, K. (2011). Anion exchange membranes for alkaline fuel cells: A review. *J. Membr. Sci.* **377**, 1-35.

Modena, S., Ceschini, S., Tomasi, A., Montinaro, D. & Sglavo, V.M. (2006). Reduction and reoxidation processes of NiO/YSZ composite for solid oxide fuel cell anodes. *J. Fuel Cell Sci. Technol.* **3**, 487-491.

Moran, M.J. & Sharpiro, H.N. (2008). *Fundamentals of Engineering Thermodynamics.* Hoboken, N.J, Wiley.

Motupally, S., Becker, A.J. & Weidner, J.W. (2000). Diffusion of water in Nafion 115 membranes. *J. Electrochem. Soc.* **147**, 3171-3177.

Myles, T.D., Kiss, A.M., Grew, K.N., Peracchio, A.A., Nelson, G.J. & Chiu, W.K.S. (2011). Calculation of water diffusion coefficients in an anion exchange membrane using a water permeation technique. *J. Electrochem. Soc.* **158**, B790-B796.

Nelson, G.J., Harris, W.M., Izzo Jr., J.R., Grew, K.N., Chiu, W.K.S., Chu, Y.S., Yi, J., Andrews, J.C., Liu, Y. & Pianetta, P. (2011). Three-dimensional mapping of nickel oxidation states using full field x-ray absorption near edge structure nanotomography. *Appl. Phys. Lett.* **98**, 173109.

Nightingale Jr., E.R. (1959). Phenomenological Theory of Ion Solvation. Effective Radii of Hydrated Ions. *J. Phys. Chem.* **63**, 1381-1387.

Norton, R. (2006). *Machine design : an integrated approach.* Upper Saddle River, N.J, Pearson Prentice Hall.

O'Grady, W.E., Pandya, K.I., Swider, K.E. & Corrigan, D.A. (1996). In situ x-ray absorption near-edge structure evidence for quadrivalent nickel in nickel battery electrodes. *J. Electrochem. Soc.* **143**, 1613-1616.

Sarantaridis, D. & Atkinson, A. (2007). Redox Cycling of Ni-Based Solid Oxide Fuel Cell Anodes: A Review. *Fuel Cells* **7**, 246-258.

Sarantaridis, D., Rudkin, R.A. & Atkinson, A. (2008). Oxidation failure modes of anode-supported solid oxide fuel cells. *J. Power Sources* **180**, 704-710.

Satterfield, M.B. & Benziger, J.B. (2008). Non-Fickian water vapor sorption dynamics by nafion membranes. *J. Phys. Chem. B* **112**, 3693-3704.

Shen, Q., Lee, W., Fezzaa, K., Chu, Y.S., De Carlo, F., Jemian, P., Ilavsky, J., Erdmann, M. & Long, G.G. (2007). Dedicated full-field X-ray imaging beamline at Advanced Photon Source. *Nucl. Instrum. Methods Phys. Res.* **582**, 77-79.

Slade, R.C.T. & Varcoe, J.R. (2005). Investigations of conductivity in FEP-based radiation-grafted alkaline anion-exchange membranes. *Solid State Ionics* **176**, 585-597.

Sone, Y., Ekdunge, P. & Simonsson, D. (1996). Proton conductivity of Nafion 117 as measured by a four-electrode AC impedance method. *J. Electrochem. Soc.* **143**, 1254-9.

Spendelow, J.S. & Wieckowski, A. (2007). Electrocatalysis of oxygen reduction and small alcohol oxidation in alkaline media. *Phys. Chem. Chem. Phys.* **9**, 2654-2675.

Thampan, T., Malhotra, S., Tang, H. & Datta, R. (2000). Modeling of conductive transport in proton-exchange membranes for fuel cells. *J. Electrochem. Soc.* **147**, 3242-3250.

Tikekar, N.M., Armstrong, T.J. & Virkar, A.V. (2006). Reduction and Reoxidation Kinetics of Nickel-Based SOFC Anodes. *J. Electrochem. Soc.* **153**, A654-A663.

Uchimoto, Y., Sawada, H. & Yao, T. (2001). Changes in electronic structure by Li ion deintercalation in LiNiO2 from nickel L-edge and O K-edge XANES. *J. Power Sources* **97–98**, 326-327.

U.S. Energy Information Administration, Monthly Energy Review, January 2014.

Varcoe, J.R. (2007). Investigations of the ex situ ionic conductivities at 30 C of metal-cation-free quaternary ammonium alkaline anion-exchange membranes in static atmospheres of different relative humidities. *Phys. Chem. Chem. Phys.* **9**, 1479-86.

Varcoe, J.R. & Slade, R.C.T. (2005). Prospects for alkaline anion-exchange membranes in low temperature fuel cells. *Fuel Cells* **5**, 187-200.

Varcoe, J.R. & Slade, R.C.T. (2006). An electron-beam-grafted ETFE alkaline anion-exchange membrane in metal-cation-free solid-state alkaline fuel cells. *Electrochem. Comm.* **8**, 839-843.

Varcoe, J.R., Slade, R.C.T., Lam, H.Y., Poynton, S.D., Driscoll, D.J. & Apperley, D.C. (2007). Poly(ethylene-co-tetrafluoroethylene)-derived radiation-grafted anion-exchange membrane with properties specifically tailored for application in metal-cation-free alkaline polymer electrolyte fuel cells. *Chem. Mater.* **19**, 2686-2693.

Vega, J.A., Chartier, C. & Mustain, W.E. (2010). Effect of hydroxide and carbonate alkaline media on anion exchange membranes. *J. Power Sources* **195**, 7176-7180.

Vila-Comamala, J., Pan, Y., Lombardo, J.J., Harris, W.M., Chiu, W.K.S., David, C. & Wang, Y. (2012). Zone-doubled Fresnel zone plates for high-resolution hard X-ray full-field transmission microscopy. *J. Synchrotron Radiat.* **19**, 705-709.

Waldbillig, D., Wood, A. & Ivey, D.G. (2005). Thermal analysis of the cyclic reduction and oxidation behaviour of SOFC anodes. *Solid State Ionics* **176**, 847-859.

Weber, A.Z. & Newman, J. (2003). Transport in polymer-electrolyte membranes. I. Physical model. *J. Electrochem. Soc.* **150**, A1008-A1015.

Yanagi, H. & Fukuta, K. (2008). Anion exchange membrane and ionomer for alkaline membrane fuel cells (AMFCs). *ECS Trans.* **16**, 257-262.

Young, J.L., Vedahara, V., Kung, S., Xia, S. & Birss, V. (2007). Understanding Nickel Oxidation and Reduction Processes in SOFC Systems. In *ECS Trans.* Eguchi, K., Mizusaki, J., Singhal, S. and Yokokawa, H. (Eds.), pp. 1511-1519. Pennington, NJ: The Electrochemical Society Proceedings Series.

Zawodzinski Jr., T.A., Derouin, C., Radzinski, S., Sherman, R.J., Smith, V.T., Springer, T.E. & Gottesfeld, S. (1993a). Water uptake by and transport through Nafion(R) 117 membranes. *J. Electrochem. Soc.* **140**, 1041-1047.

Zawodzinski Jr., T.A., Springer, T.E., Davey, J., Jestel, R., Lopez, C., Valerio, J. & Gottesfeld, S. (1993b). Comparative study of water uptake by and transport through ionomeric fuel cell membranes. *J. Electrochem. Soc.* **140**, 1981-1985.

Zawodzinski, T.A., Neeman, M., Sillerud, L.O. & Gottesfeld, S. (1991). Determination of Water Diffusion Coefficients in Perfluorosulfonate Ionomeric Membranes. *J. Phys. Chem.* **95**, 6040.